Electronic Thesis and Dissertation Repository

6-1-2022 2:00 PM

Electrical And Mechanical Properties Of Polymer Nanocomposites

Nuwansiri N.K. Getangama, *The University of Western Ontario*

Supervisor: Dr. John R. de Bruyn, *The University of Western Ontario*
Co-Supervisor: Dr. Jeffrey L. Hutter, *The University of Western Ontario*
A thesis submitted in partial fulfillment of the requirements for the Doctor of Philosophy degree in Physics
© Nuwansiri N.K. Getangama 2022

Follow this and additional works at: https://ir.lib.uwo.ca/etd

⬤ Part of the Condensed Matter Physics Commons

Recommended Citation

Abstract

This thesis consists of three projects concerning the electrical and mechanical properties of polymer nanocomposites. We study the effect of nanoscale filler particles on the polymer dynamics at different length and time scales. In the first study, poly(ethylene oxide) (PEO)-multiwalled carbon nanotubes (MWCNT) nanocomposites with a MWCNT concentration ranging from 0 to 5 wt% were prepared by both melt-mixing and twin-screw extrusion. Their electrical properties were studied over a wide range of frequency and temperature using a dielectric spectrometer. A percolation transition is observed at which the electrical conductivity of the nanocomposites increases by several orders of magnitude. The percolation threshold concentration p_c is very well-defined in the twin-screw extruded material, but less so in the melt-mixed nanocomposites. We identify two different dielectric relaxation processes in our PEO/MWCNT nanocomposites, which we attribute to polymer dynamics at different length scales. The second project is a study of the mechanical properties of PEO/MWCNT nanocomposites made by melt-mixing. We used a rotational shear rheometer to perform measurements during thermal cycling. Our results show that there are three main mechanical relaxation times in the nanocomposites, all of which are much slower than the relaxation times observed in dielectric data. One of these processes is due to the reptation of polymer chains. Another is due to the relaxation of PEO chains whose motions are restricted by MWCNT. The third one is related to the sample preparation process. In the last project, we used dielectric spectroscopy to investigate the electrical properties of polystyrene (PS)-MWCNT nanocomposites made using twin-screw extrusion. Our data suggest that the percolation threshold for these nanocomposites is between 4 and 5 wt%, but the transition only occurs once the sample has been heated above 330 K. In most cases, the dielectric spectrum did not show any relaxation features. A dielectric relaxation was only observed for a MWCNT concentration of 5 wt%, and the relaxation peak disappeared when the sample was heated above 330 K due to the high electrical conductivity of the sample. Our studies showed several examples of polymer dynamics influenced by the presence of MWCNT on time scales ranging from microseconds to hundreds of seconds.

Summary for lay audience

Polymer nanocomposites are a novel class of composite material made by adding nanometer-sized filler particles to a polymer. The properties of the nanocomposites can be enhanced over those of the pure polymer by choosing the right filler. For example, conducting materials can be made from an insulating polymer by adding a conductive nanofiller such as carbon nanotubes, and the conductivity can be tuned by changing the concentration of the filler particles. The main motivation for this work is to use measurements of polymer nanocomposites to learn about the motion of the polymer molecules at different length scales. In particular, we want to study how the presence of nanotubes affects the polymer dynamics. Here we study nanocomposites made by adding a small amount of carbon nanotubes to poly(ethylene oxide) and polystyrene. We were able to examine the distribution of nanotubes in the polymers using a scanning electron microscope. Our dielectric data showed evidence of microsecond-scale polymer dynamics in the nanocomposites. The mechanical measurements showed the presence of slow polymer dynamics occurring over time scales ranging from one-tenth of a second to few hundred seconds. Pure poly(ethylene oxide) and pure polystyrene are both insulators. Our data showed that nanocomposites based on these polymers become conducting when a few weight percent of carbon nanotubes was added to the polymer. For example, the electrical conductivity of poly(ethylene oxide) with 5% carbon nanotubes added was a factor of 10^8 higher than that of the pure polymer. The conductivity increase for the polystyrene nanocomposite was even higher - a factor of 10^{11}.

Co-Authorship Statement

Chapter 4 has been accepted for publication: Nuwansiri Nirosh Getangama, John R. de Bruyn, Jeffrey L. Hutter, Dielectric spectroscopy of poly(ethylene oxide)-carbon nanotube nanocomposites, to be published in *AIP Advances.*

I did all the experiments and data analysis reported in Chapter 4 and was the primary author of the paper. John R. de Bruyn and Jeffrey L. Hutter supervised the project and provided editorial comments on the paper.

I did all the experiments and data analysis reported in Chapter 5 and was the primary author of the paper. John R. de Bruyn and Jeffrey L. Hutter supervised the project and provided editorial comments on the paper.

I did all the experiments and data analysis reported in Chapter 6 and was the primary author of the paper. John R. de Bruyn and Jeffrey L. Hutter supervised the project and provided editorial comments on the paper.

Acknowledgements

I would like to express my deepest gratitude to my supervisors Dr. John de Bruyn and Dr. Jeffrey Hutter for their supervision and guidance. I'm grateful for their continuous support and encouragement throughout my work which helped me to develop both professionally and personally.

I would also like to thank my advisory committee members Dr. Lyudmila Goncharova and Dr. Mahi Singh for insightful comments and interesting discussions which increased my understanding and interest in my field.

My special thanks go to my colleagues Cameron Hopkins, Yang Liu, and Colin Versnick in Dr. de Bruyn's research group and Himasha Wijesekara in Dr. Hutter's research group for stimulating discussions and being a great team. I also thank fellow graduate students and all faculty and staff in my department for their friendly and kind support.

I am grateful to A. Hrymak, S. Zhou, P. Charpentier, D. V. Hiscott, D. M. Hull, X.A. Sun, Q. Sun and J. Liang for assistance in sample preparation, and to T. Simpson and T. Goldhawk for assistance with the SEM imaging.

I also thank my parents, three sisters and their families for their continuous support and encouragement throughout my life. I thank my son Dineth for his love and giggles which gave me strength to continue. Finally, I am specially thankful to my wife Jayanayana for her persistent support, patience and understanding.

Contents

List of Figures

xvi

List of Tables

Chapter 1

Introduction

1.1 Overview

In this Chapter, we introduce the main concepts needed to understand the work presented in this thesis. We then briefly discuss previous work on the dielectric and mechanical properties of polymer nanocomposites before presenting the motivation for this work at the end of the Chapter.

1.2 Polymer nanocomposites

A polymer molecule consists of many repeating subunits called monomers. These are joined together to form a long molecule with a large molecular weight. A polymer composite is a material made by adding micron scale or smaller filler particles to a polymer to form a well-dispersed homogeneous blend. When the filler particles are of order nanometers in size, the composites are called polymer nanocomposites. The properties of a polymeric material can be changed dramatically by adding even a small amount of filler particles. Some of the parameters that affect the properties of a composite are the size, volume fraction, shape, and electrical and mechanical properties of the filler particles. The high surface to volume ratio of the nanoscale filler particles leads to enhanced polymer-filler interactions. Previous researchers have used

many different types of filler particles including silica [1], calcium carbonate [2], glass beads or fibers [3], metal nanoparticles [4], and carbon nanotubes (CNT) [5]. Polymer nanocomposites have been of great interest in a wide range of applications in industries such as automobiles, aerospace, adhesives, and packing materials [6] due to their enhanced properties such as structural strength, optical properties, electrical and mechanical properties.

In this thesis, we study the electrical and mechanical properties of nanocomposites made by adding multiwalled carbon nanotubes (MWCNT) to poly(ethylene oxide) (PEO) and the electrical properties of polystyrene-MWCNT (PS-MWCNT) nanocomposites. The nanotubes are electrically conductive, and adding a few percent of MWCNT causes the conductivity to increase by many orders of magnitude over that of the pure polymer. Similarly, the elastic modulus of the nanocomposites can be increased by adding MWCNT to the polymer.

1.3   Dielectric spectroscopy

The electromagnetic properties of a material depends on many factors such as the structure, the energy band structure of the material, and the magnetic moment of its atoms and molecules. The dielectric properties of a material can be obtained by studying the response of the material to an external electric field. Dielectric spectroscopy is one of the tools that can be used to study the macroscopic electric properties of a material under the influence of an external electric field.

In dielectric spectroscopy, the dielectric properties of a material are measured as a function of the angular frequency ω or frequency f of the applied electric field. The permittivity $\varepsilon(\omega)$ is the primary dielectric property that characterizes the response of the material to an applied electric field. The permittivity $\varepsilon = \varepsilon' - i\varepsilon''$ is a complex quantity. The real part is the dielectric constant and represents the material's capability to store electrical energy. The imaginary part ε'' quantifies the dissipation of electrical energy due to the electrical resistance of the material.

Ionic relaxation, dipolar relaxation, atomic polarization, and electronic polarization all con-

tribute to the measured permittivity. Each of these phenomena dominates in a different frequency range, as shown in Fig. 1.1. The permittivity spectrum of a material provides insights into the importance and time scale of each of these processes. This information can in turn be interpreted in terms of the microscopic structural properties of the material.
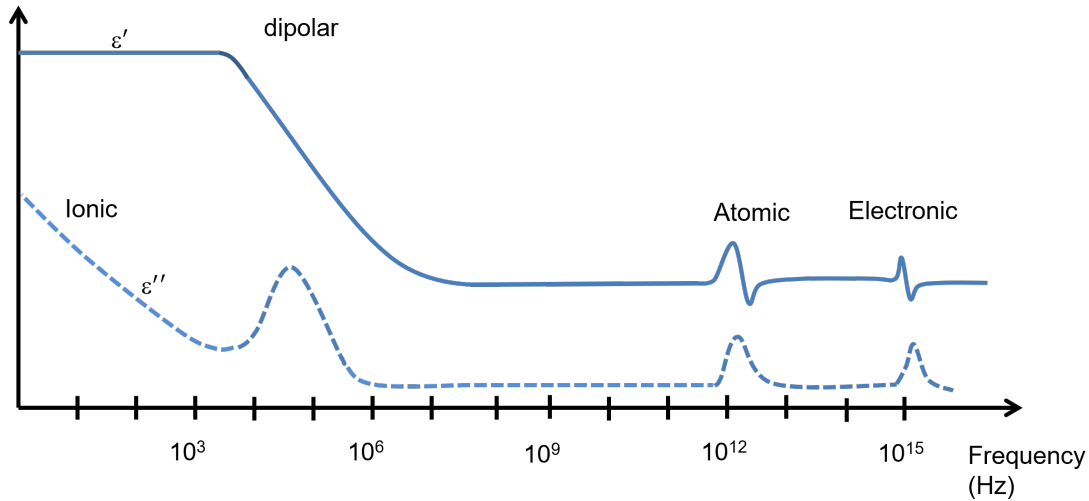
Figure 1.1: Schematic graph of the real ε' and imaginary ε'' parts of the complex permittivity $\varepsilon(f)$ as a function of frequency. The contributions of different phenomena to the permittivity at different frequency ranges are indicated in the figure.

At low frequencies, ionic relaxation is the dominant contribution to the imaginary part of permittivity as $\epsilon'' = \sigma_{dc}/\varepsilon_0 \omega$ where σ_{dc} and ε_0 are the electrical conductivity of the material and the dielectric constant of free space, respectively. Because of this, highly conductive materials show a linear behaviour in ε'' with $1/\omega$ at low frequencies. Dipolar relaxation is important in materials that contain molecules with permanent dipole moments, such as water. This will be discussed in Chapter 2. When atoms or ions in a set of molecules are exposed to an external electric field, they undergo displacements from their equilibrium positions inducing a dipole moment. This is atomic or ionic polarization. Electronic polarization occurs in same manner. Under an electric field, the electron cloud of a neutral atom becomes distorted, inducing a dipole moment in the atom. In the experiments described in this thesis, we studied the frequency range between 100 mHz and 1 MHz and we mainly see effects due to ionic and dipolar relaxation.

3

1.4 Rheological properties

Solids and fluids behave differently under the action of an external stress. A solid deforms under stress and recovers its original form due to its elasticity once the stress is removed. In contrast, a fluid flows under stress and its deformation is permanent once the stress is removed. Many important materials show a mix of solid and fluid behaviour and are referred to as viscoelastic materials. Polymer nanocomposites are viscoelastic.

We study the rheological properties of our nanocomposites by measuring their response to an externally applied stress or strain in both the frequency and the time domains. In the frequency domain, we measure the complex modulus $G = G' + iG''$. The real and imaginary parts represent the elastic and viscous nature of a material, respectively. We studied G' and G'' in the angular frequency range between 0.1 to 100 rad/s. This frequency range is small compared to the frequency range used in dielectric measurements. These low-frequency measurements allow us to explore properties due to the motions of polymer molecules.

In the time domain, we study the creep and recovery of the polymer nanocomposites. In creep, a constant stress is applied to a material and its strain is measured over time. In creep recovery, the material's strain is measured as a function of time once the applied stress is removed. These experiments will be explained in detail in Chapter 2.

1.5 Summary of previous work

Nanocomposites have been of great interest, and extensive work has been performed to study their properties such as degree of crystallinity, optical properties, electrical properties, mechanical properties, and thermal conductivity [1, 5, 7]. The exceptional mechanical and electrical properties of carbon nanotubes (CNT) have led to much effort from researchers and industry to produce CNT-based nanocomposites. For example, the elastic modulus of single-walled CNT can be as high as 1.2 TPa, close to that of diamond, and their electrical conductivity can be similar to that of copper. Conductive fillers such as CNT can be used to increase the electrical

4

conductivity of an insulating polymer. When the filler concentration p exceeds a critical value called the percolation threshold p_c [8], the filler particles form a three-dimensional conductive network that spans the material sample, [9] leading to a dramatic increase in conductivity. Polymer-CNT nanocomposites have been made with percolation thresholds ranging from as small as 0.005 vol% up to several vol% [10].

Pötschke et al. [8] studied the dielectric properties of nanocomposites made by melt mixing polycarbonate and multi-walled carbon nanotubes (MWCNT) with diameters of 10–15 nm and lengths of 1–10 μm. They measured the real and imaginary parts of the permittivity in the frequency range of 10^{-4} Hz to 10^{7} Hz and observed an increase in both ε' and ε'' with increasing MWCNT concentration. The DC conductivity of these composites changed by more than 10 orders of magnitude when the MWCNT concentration was varied from 1.0 to 1.5 wt%, indicating that the percolation threshold was in this concentration range. As they varied the MWCNT concentration from 0 to 5 wt%, the conductivity changed from on the order of 10^{-14} to 1 S/m.

Above (but close to) the percolation transition, the dc conductivity σ_{dc} follows a power law in $p - p_c$ [9, 11, 12]. The critical exponent t of the power law has a theoretical value of approximately 2 for a simple cubic three-dimensional network [13]. Pötschke et al. found t to be 2.1 in the polymer nanocomposites mentioned above.

The mechanical properties of a polymer also can be improved with the addition of nanoscale particles [1]. Complex materials such as polymers and polymer composites exhibit both elastic and viscous behavior and thus are viscoelastic materials. Most polymers and polymer nanocomposites are shear-thinning due to the disentanglement of the polymer coils under shear and the increased orientation of the coils in the direction of shear [14]. Song [15] examined the rheological properties of PEO/MWCNT nanocomposites at different MWCNT concentrations. The nanocomposites exhibited shear-thinning behavior when the MWCNT concentration was higher than 1 wt%. Also, the shear viscosity increased with increasing MWCNT concentration, particularly at low shear rates. Polymer-MWCNT interactions increase with increasing

MWCNT loading, and that leads to the enhancement of the shear viscosity. It was also reported that G' increased with MWCNT concentration due to the increased interparticle interactions.

Pötschke et al. [16] studied the rheological behavior of compression molded mixtures of polycarbonate MWCNT nanocomposites. They found an increase in both G' and G'' with increased MWCNT loading, particularly at low frequencies. At high loadings, nanotube-nanotube interactions begin to dominate. Eventually an interconnected structure of nanotubes forms, which causes a large increase in both G' and G''.

The critical CNT concentrations needed to enhance the electrical and mechanical properties of polymer-based carbon nanotube composites are mainly dependant on the degree of homogeneity of the dispersion of CNT in the polymer, and on the purity of the CNTs. Carbon nanotubes in a dispersion tend to aggregate due to van der Waals forces between tubes, and thorough mixing is required to limit aggregation and reduce the percolation threshold. Aggregation of the CNTs causes the percolation threshold to increase because more nanotubes are needed to make a conductive network throughout the sample.

1.6 Motivation and scope

Many of the materials in living organisms such as proteins and cellulose are polymers. Polymers are of great interest in research and industrial applications. In particular, PEO and its nanocomposites are of interest as PEO can incorporate different types of filler particles over a range of concentrations.

The main motivation is to use the dielectric and rheological measurements to learn about polymer dynamics. In particular, we want to learn about how the presence of the nanotubes affects the polymer dynamics. With this motivation, we study the electrical properties of PEO-MWCNT and PS-MWCNT nanocomposites and the mechanical properties of PEO-MWCNT nanocomposites. These studies would help us to understand different time scale macromolecular dynamics.

In Chapter 2, we present the theoretical background relevant to our electrical and mechanical measurements. Chapter 3 describes the materials, sample preparation, and experimental methods used in this work. We present the results of our dielectric and mechanical measurements on PEO-MWCNT nanocomposites in Chapter 4 and Chapter 5, respectively. Chapter 6 presents the electrical properties of PS-MWCNT composites. Finally, Chapter 7 includes a general discussion and a summary of our conclusions.

Bibliography

[1] J. Jordan, K. I. Jacob, R. Tannenbaum, and M. A. Sharaf. *Mater. Sci. Eng. A* ., 393:1, 2005.

[2] R. D. K. Misra, P. Nerikar, K. Bertrand, and D. Murphy. *Mater. Sci. Eng. A* ., 384:284, 2004.

[3] A. T. DiBenedetto. *Mater. Sci. Eng. A* ., 302:74, 2001.

[4] M. Rubinstein and R.H. Colby. *Polymer Physics*. Oxford University Press, 2003.

[5] P. J. F. Harris. *Int. Mater. Rev.*, 49:31, 2004.

[6] F. Hussain, M. Hojjati, and R. E. Gorga. *J. Compos. Mater.*, 40:1511, 2006.

[7] Z. Hana and A. Finab. *Prog. Polym. Sci.*, 36:914, 2010.

[8] P. Pötschke, S. M. Dudkin, and I. Alig. *Polymer*, 44:5023, 2003.

[9] D.Stauffer and A. Aharony. *Introduction to Percolation Theory, Revised 2nd Edition*. CRC press, 2018.

[10] M. Moniruzzaman and I. Winey. *Macromolecules*, 39:5194, 2006.

[11] S. Kirkpatrick. *Rev. Mod. Phys.*, 45:574, 1973.

[12] W. Bauhofer and J. Z. Kovacs. *Compos. Sci. Tech.*, 69:1486, 2009.

[13] D. B. Gingold and C. J. Lobb. *Phys. Rev. B*, 42:8220, 1990.

[14] C. Clasen and W-M. Kulicke. *Prog. Polym. Sci.*, 9:1839, 2001.

[15] Y. S. Song. *Rheol. Acta*, 46:231, 2009.

[16] P. Pötschke, T. D. Fornes, and D. R. Paul. *Polymer*, 43:3247, 2002.

Chapter 2

Theory

2.1 Overview

In this Chapter, we present the theoretical background of dielectric spectroscopy and rheological measurements. We first introduce the concept of dielectric polarization, then discuss dielectric properties such as complex permittivity and dielectric relaxation time. We then review the rheology of viscoelastic materials and discuss the complex viscoelastic modulus, rheological relaxation time, and other important properties.

2.2 Dielectric materials

Materials can be divided into three categories based on their electrical conductivity: insulators, semiconductors, and conductors. The electrical conductivity of these materials can be explained using band theory. The energy of an electron in an atom can have only certain values referred to as energy levels. An energy band is a group of energy levels that are so close to each other that they overlap to form a continuous band. An energy band is a property of a material made up of many, many atoms. The valence band is the highest energy band that is completely filled with electrons. The lowest partially filled band is called the conduction band. The band gap E_g is the energy difference between the top of the valence band and the bottom of the

conduction band in insulators and semiconductors. In conductors, the conduction band is partially filled and the valence and conduction bands overlap, so the band gap is zero. As a result, conductors can support a substantial electric current when subjected to an externally applied electric field. In semiconductors, the band gap is non-zero but small enough that a significant number of electrons can be promoted to the conduction band thermally, or by an external voltage or photon absorption. On the other hand, insulators have a higher energy gap, such that the thermal energy $k_B T$, where k_B is Boltzmann's constant and T is the absolute temperature, is much less than energy gap. In this case, the probability of an electron being promoted into the conduction band is very small, resulting in a very small electrical conductivity.

Dielectric materials are insulators, with a band gap typically above $3\,\text{eV}$. These materials respond to an external electric field by polarization.

2.2.1   Dielectric polarization

Some molecules, such as the water molecule shown in Fig. 2.1, have a permanent dipole moment even though their net charge is zero. A water molecule has a dipole moment due to the fact that oxygen is more electronegative than hydrogen. The dipole moment of water is 6.2×10^{-30} C·m. A collection of dipolar molecules will be oriented randomly in the absence of an electric field. Under an external electric field, the dipoles experience a torque causing them to orient in the direction of the field. In non-dipolar molecules, the relative positions of the electrons and positive nuclei shift slightly from their equilibrium positions when exposed to an electric field, thus inducing a dipole moment. Both of these processes result in what is called dielectric polarization.
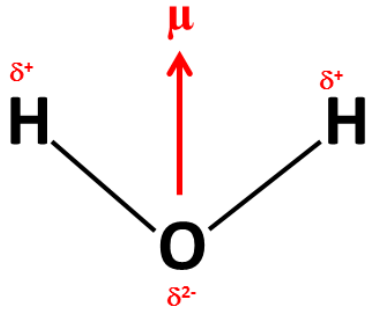
Figure 2.1: Schematic of the permanent dipole moment of water. The electrons in the molecule are attracted more to the oxygen atom than to the hydrogen atoms, with the result that the oxygen and hydrogen tend to be more negative and more positive, represented by δ^{2-} and δ^{+}, respectively. μ is the total dipole moment of the water molecule [1].

Figure 2.2(a) shows a schematic illustration of a dielectric material placed inside a parallel-plate capacitor with no externally applied electric field. Each atom, represented by a circle, consists of a positive point charge at the center and a cloud of electrons surrounding it, with no net dipole moment. When an external electric field is applied across the capacitor, the charge cloud is distorted as shown in Fig.2.2(b), inducing a dielectric dipole moment. This process is called dielectric polarization. The induced dipole moment disappears once the external electric field is removed.
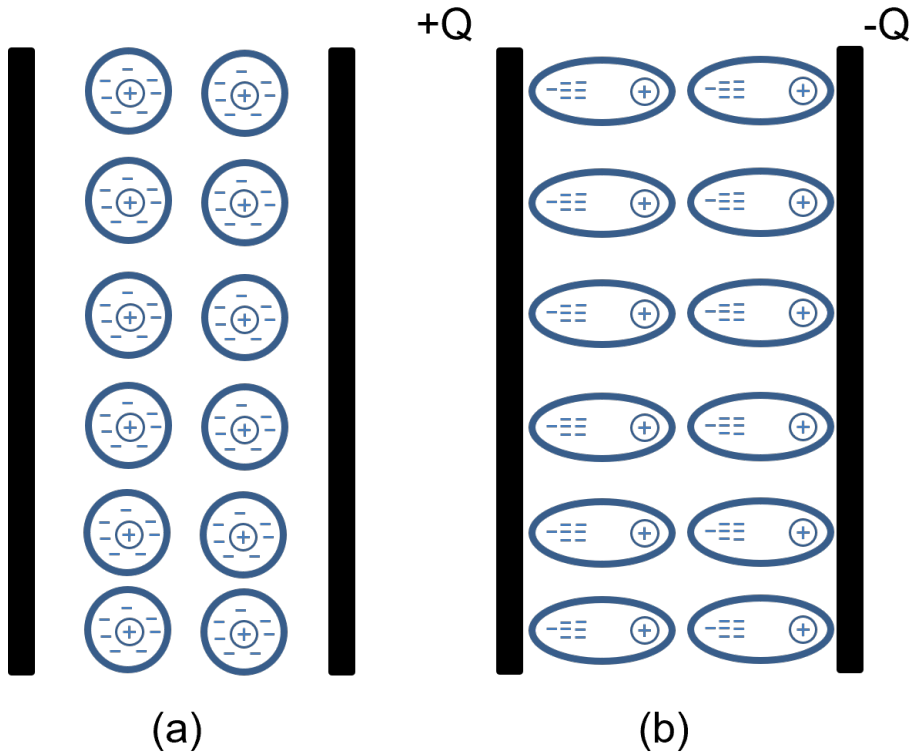
Figure 2.2: A dielectric material in a parallel-plate capacitor (a) with no external electric field and (b) in an applied field. In each atom the positive nucleus has a charge that balances the negative charges. In (a), the electrons and positive ions are in equilibrium, and there is no net polarization. In the presence of an electric field (when the capacitor is charged), the applied field induces a dipole moment in the dielectric material.

2.3   Theory of dielectric spectroscopy

In dielectric spectroscopy, we study the influence of an alternating electric field on materials. Dielectric data can be used to understand the microstructure of the nanocomposites, the microscopic interactions between the nanotubes and the polymer molecules, and the electrical charge transport mechanism in nanocomposites. In dielectric spectroscopy, measurements can be made in both the time and frequency domains. In time-domain experiments, the field is changed suddenly (for example by applying a pulsed field), and the response is studied as a function of time. In the frequency domain, a sinusoidally alternating electric field is applied to the sample and the frequency is swept over a large range.

2.3.1 Electric susceptibility and permittivity

Consider a parallel plate capacitor. The electric susceptibility χ of the material in the gap between the plates is defined by

$$\chi = \frac{C - C_0}{C_0},\tag{2.1}$$

where C_0 and C are capacitance when the gap is under vacuum and when it is filled with a dielectric material, respectively. The electric permittivity ε is defined as

$$\varepsilon = \frac{C}{C_0}.\tag{2.2}$$

Combining Eq. 2.1 and 2.2, the relationship between susceptibility and permittivity can be written as

$$\chi = \varepsilon - 1.\tag{2.3}$$

The polarization $\mathbf{P}$ is the dipole moment in a unit volume of a dielectric material. The polarization is proportional to the material's susceptibility. The polarization vector of a dielectric material in an electric field $\mathbf{E}$ can be written as

$$\mathbf{P} = \chi \varepsilon_0 \mathbf{E},\tag{2.4}$$

where ε_0 is the vacuum permittivity. By substituting χ from Eq. 2.3 to Eq. 2.4,

$$\begin{aligned} \mathbf{P} &= (\varepsilon - 1)\varepsilon_0 \mathbf{E} \\ &= \varepsilon \varepsilon_0 \mathbf{E} - \varepsilon_0 \mathbf{E}. \end{aligned}$$

$\varepsilon_0 \varepsilon \mathbf{E}$ is called the electric displacement $\mathbf{D}$ in the material. Then,

$$\mathbf{P} = \mathbf{D} - \varepsilon_0 \mathbf{E}.\tag{2.5}$$

Imagine we place a molecule with an electric dipole moment in a viscous medium and apply a

time varying electric field $E(t) = E_0 \cos \omega t$. At low enough frequencies, the orientation of the dipole can follow the field, but at high frequencies it cannot, due to the viscosity of the medium and the inertia of the molecule. As a result of this, the polarization vector lags the electric field. This delayed response of the polarization vector leads to a phase difference δ between the external electric field and the polarization and displacement vectors. The magnitude of the electric displacement field can be expressed as

$$D = D_0 \cos(\omega t - \delta). \tag{2.6}$$

Expanding the cosine function,

$$D = D_0 \cos \delta \cos \omega t + D_0 \sin \delta \sin \omega t. \tag{2.7}$$

The permittivity is a complex quantity that can be written as

$$\varepsilon(\omega) = \varepsilon'(\omega) - i\varepsilon''(\omega), \tag{2.8}$$

where the real and imaginary parts of the permittivity are defined by [2]

$$\varepsilon' = \frac{D_0 \cos \delta}{\varepsilon_0 E_0} \tag{2.9}$$

and

$$\varepsilon'' = \frac{D_0 \sin \delta}{\varepsilon_0 E_0}, \tag{2.10}$$

respectively. The real and imaginary parts of the permittivity are not independent, but are related by the Kramers-Kronig relation [3].

The dielectric loss tangent or dissipation factor $\tan \delta$ is defined using Equations (2.9) and (2.10) as

$$\tan \delta = \frac{\varepsilon''}{\varepsilon'}. \tag{2.11}$$

2.3.2 Dielectric measurement techniques

Generally in a dielectric measurement, the complex impedance $Z(\omega)$ is measured and the dielectric permittivity $\varepsilon(\omega)$ is derived from the complex impedance as

$$\varepsilon(\omega) \quad = \quad \frac{1}{i\omega Z(\omega) C_0}. \tag{2.12}$$

In the Solartron Materials Test System (MTS) used in our experiments, a sample is placed between the plates of a capacitor. Then a voltage is applied across the sample and the corresponding current and phase difference are measured to calculate the complex impedance [1]. We study the dielectric properties of our samples in the frequency range from 0.1 Hz to 1 MHz.

2.3.3 Dielectric relaxation

When a dielectric material is exposed to an external electric field, the dipoles in the material experience torques which tend to align them with the applied field. When the applied field is removed, the dipoles randomize again, resulting in zero net polarization in equilibrium. This randomization process is referred to as dielectric relaxation and the characteristic time taken to reach the new equilibrium state is referred to as the dielectric relaxation time, τ. The relaxation process depends on molecular structure, as well as on factors such as inertia of the dipoles, temperature, pressure, and viscosity. Depending on the observed frequency range and its microscopic structure, a material may have more than one dielectric relaxation process and, correspondingly, more than one relaxation time.

The simplest model to explain the complex permittivity is Debye model [2, 4]. This model explains the complex dielectric function and the relaxation process in gases and dilute solutions by assuming no interactions between molecular dipoles and an exponential approach to the equilibrium state. Debye's model for $\varepsilon(\omega)$ is

$$\varepsilon(\omega) = \varepsilon_\infty + \frac{\varepsilon_s - \varepsilon_\infty}{1 + i\omega\tau}, \tag{2.13}$$

15

where ε_∞ and ε_s are the infinite frequency and static permittivities, and ω is the angular frequency of the applied electric field. The real and imaginary parts of this model can be separated as

$$\varepsilon'(\omega) = \varepsilon_\infty + \frac{\varepsilon_s - \varepsilon_\infty}{1 + \omega^2\tau^2} \tag{2.14}$$

and

$$\varepsilon''(\omega) = \frac{\varepsilon_s - \varepsilon_\infty}{1 + \omega^2\tau^2}\omega\tau, \tag{2.15}$$

so that the loss tangent is

$$\begin{aligned}
\tan\delta &= \frac{\varepsilon''(\omega)}{\varepsilon'(\omega)} \\
&= \frac{(\varepsilon_s - \varepsilon_\infty)\omega\tau}{\varepsilon_s + \varepsilon_\infty\omega^2\tau^2}.
\end{aligned} \tag{2.16}$$

$\tan\delta$ is a peaked function which can be used to find the relaxation time τ. Setting the first derivative of Eq. 2.16 with respect to ω to zero and solving for τ, the relaxation time is found to be

$$\tau = \frac{1}{\omega_{max}}\sqrt{\frac{\varepsilon_s}{\varepsilon_\infty}} \tag{2.17}$$

where ω_{max} is angular frequency corresponding to the peak in $\tan\delta$.

To illustrate the behaviour of the Debye model, ε', ε'' and $\tan\delta$ were calculated from Debye's equation supposing $\varepsilon_\infty = 5$ and $\varepsilon_s = 80$. The results are plotted as functions of angular frequency in Figs. 2.3, 2.4, and 2.5.

The real part of the Debye permittivity versus angular frequency is shown in Fig. 2.3. The center of the sudden decrease in ε' occurs at an angular frequency equal to $1/\tau$.

The dielectric loss ε'' in Eq. 2.15 is a peaked function as shown in Fig. 2.4. The reciprocal

16

of the peak frequency gives τ, the relaxation time of the sample. The correspondence between the peak in the imaginary part and the inflection point in the step in the real part is consistent with the Kramers-Kronig relations [3].
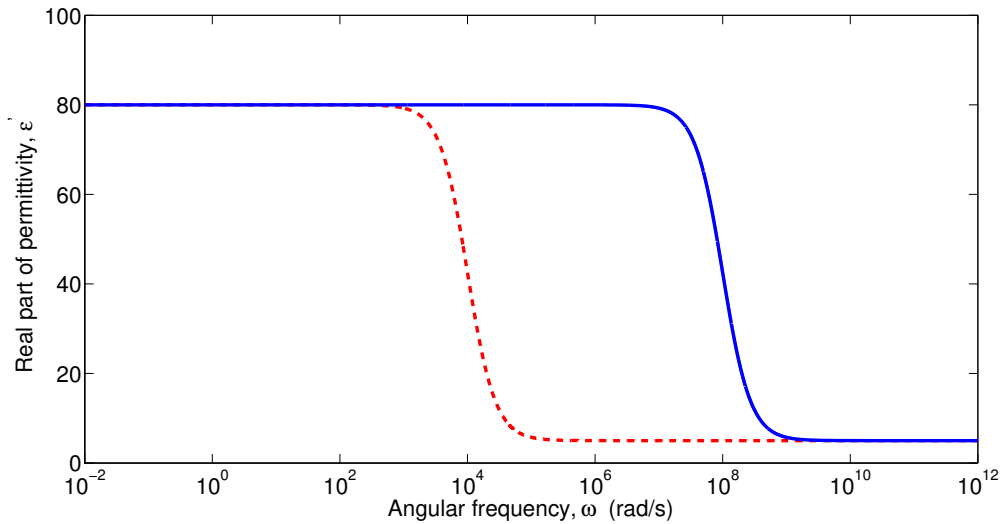
Figure 2.3: Real part of the Debye permittivity versus angular frequency. The red dashed line shows ε' when $\tau = 10^{-4}$ s and the blue line when $\tau = 10^{-8}$ s. Here $\varepsilon_s = 80$ and $\varepsilon_\infty = 5$ [1].

The position of the peak in ε'' changes with the relaxation time as shown in Fig. 2.4.
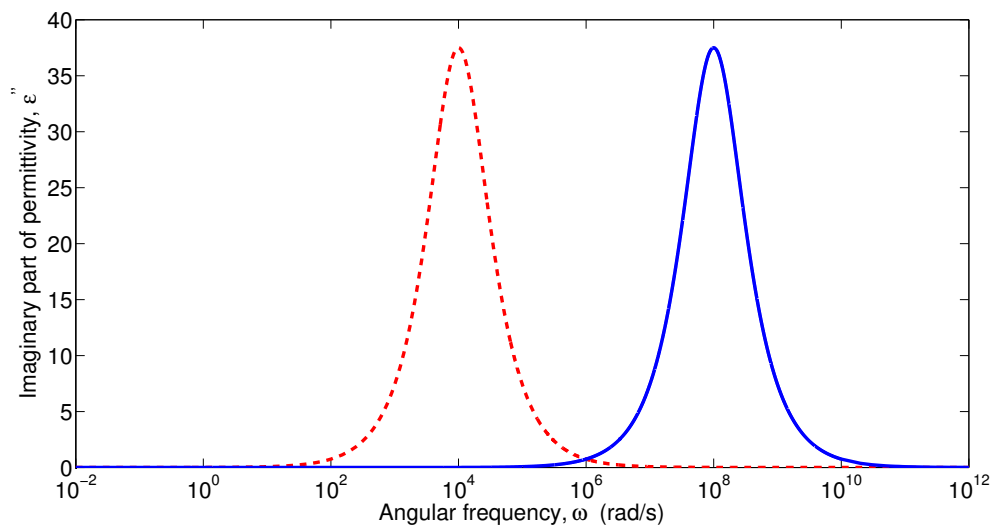
Figure 2.4: Imaginary part of the Debye's permittivity versus angular frequency. The red dashed line shows ε'' when $\tau = 10^{-4}$ s and the blue line when $\tau = 10^{-8}$ s. Here $\varepsilon_s = 80$ and $\varepsilon_\infty = 5$ [1]

17

Figure 2.5 shows the dielectric loss tangent of the Debye model versus angular frequency. Comparing Figs. 2.4 and 2.5, it can be recognized the peak frequency in $\tan \delta$ has shifted by a factor $\sqrt{\frac{\varepsilon_s}{\varepsilon_\infty}} = 4$ compared to the peak in ε''.
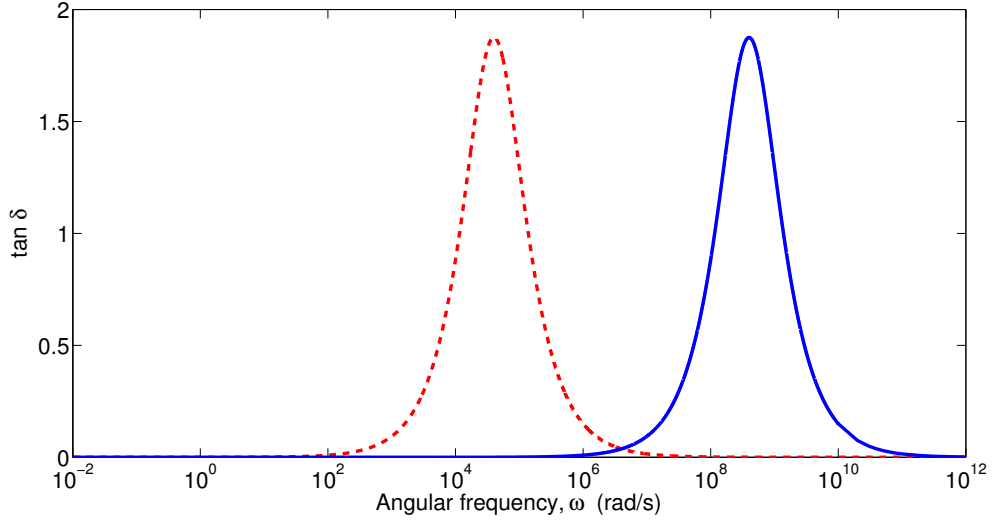
Figure 2.5: Dielectric loss tangent from the Debye permittivity versus angular frequency. The red dashed line shows $\tan \delta$ when $\tau = 10^{-4}$ s and the blue line when $\tau = 10^{-8}$ s. Here $\varepsilon_s = 80$ and $\varepsilon_\infty = 5$ [1].

Because of interactions between dipoles and the presence of more than one relaxation process, the dielectric behaviour of complex materials such as polymer nanocomposites cannot be explained by the simple Debye model with a single relaxation term. Modified Debye equations have been used to model the behaviour of such materials. Some modified models involve adding more relaxation terms to the Debye model [5]. Another modified Debye model is the Cole-Cole model [6], which has been used to fit the dielectric response in polymers.

The empirical Havriliak-Negami (HN) model [7] is another modified Debye model that has been used to describe the complex dielectric permittivity. This model has an extra term to describe the $1/\omega$ behaviour of ε'' observed at low frequencies. It has used to describe the dielectric behaviour of nanocomposites with substantial electrical conductivity. The HN model has been applied to polymeric materials by several groups [7, 8, 9]. In the HN model, the complex permittivity $\epsilon^* = \epsilon' - i\epsilon''$ is given by

$$\epsilon^* = \epsilon_\infty + \frac{\Delta\epsilon_1}{(1 + (i\omega\tau_1)^{\alpha_1})^{\beta_1}} + \frac{\Delta\epsilon_2}{(1 + (i\omega\tau_2)^{\alpha_2})^{\beta_2}} + \frac{\sigma_{dc}}{i\omega\epsilon_0} \qquad (2.18)$$

where $\Delta\epsilon_1$ and $\Delta\epsilon_2$ are dielectric strengths and τ_1 and τ_2 are relaxation times. The four terms on the right-hand side of Eq. (2.18) represent contributions to ϵ^* due to the constant infinite-frequency dielectric constant ϵ_∞, two relaxation processes, and the dc conductivity σ_{dc}.

When the exponents α_1, α_2, β_1 and β_2 in Eq. (2.18) are all equal to 1, the two relaxation terms describe exponential (Debye) relaxation processes with relaxation times τ_1 and τ_2, respectively. When these exponents are not equal to 1, the relaxations are non-exponential. For non-exponential relaxation processes, τ_1 and τ_2 can be regarded as characteristic relaxation times. Each relaxation process is manifested as a peak in ϵ''.
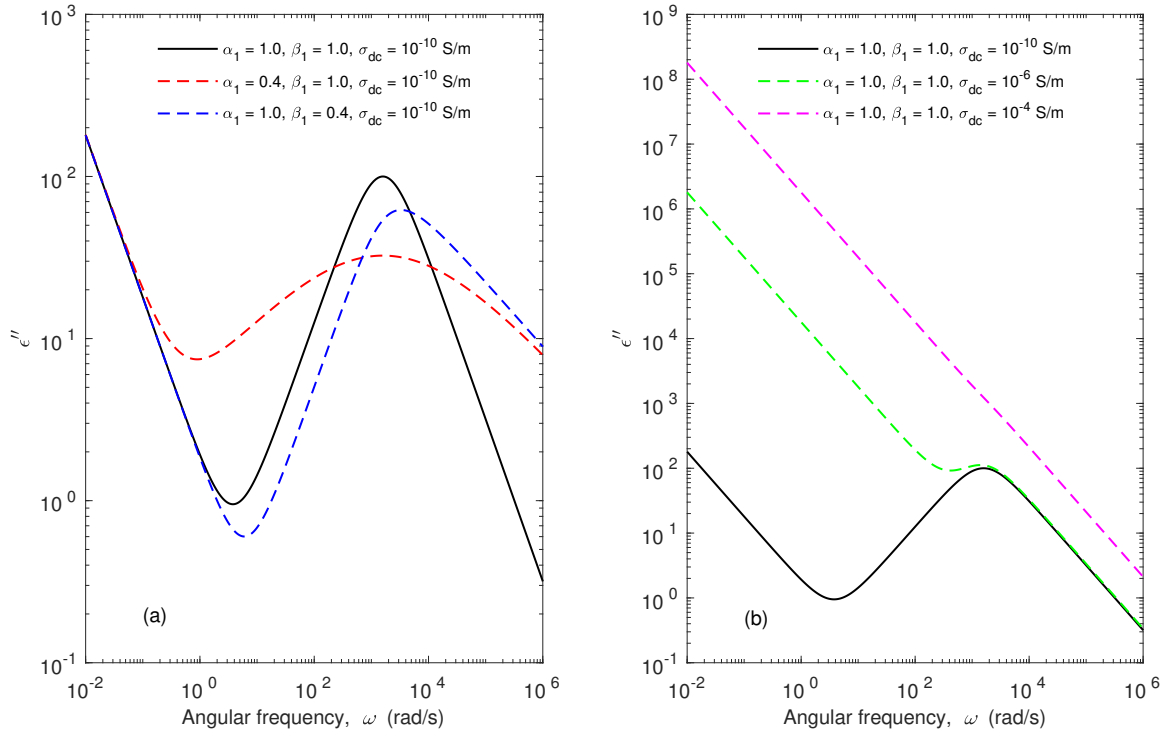
Figure 2.6: Imaginary part of the HN model with one relaxation process versus angular frequency. (a) and (b) show the effect of α_1 and β_1 and σ_{dc} respectively on ε''. The black line in each subplot represents ε'' with parameters $\Delta\epsilon_1 = 200$, $\tau_1 = 10^{-4}$ s, $\alpha_1 = 1$, $\beta_1 = 1$ and $\sigma_{dc} = 10^{-10}$ S/m. In (a), the red and blue dashed lines have different values of α_1 and β_1, as indicated in the legend. The effect of σ_{dc} on ε'' is shown in (b). The curves correspond to three different values of the conductivity, as indicated in the legend, with all other parameters fixed.

Fig. 2.6 shows the imaginary part of the permittivity calculated from the HN model with a single relaxation term versus angular frequency. To easily visualize the effect of the parameters in the HN model on ε'', only one relaxation process is presented. The α parameter controls the slopes of the sides of the relaxation peak and thus their width as shown in Fig. 2.6 (a). β affects the slope of the high-frequency side of the peak, thus varying the skewness as also shown in Fig. 2.6(a). σ_{dc} plays an important role in the behaviour of ε'' as shown in Fig. 2.6 (b). When σ_{dc} increases from 10^{-8} to 10^{-4} S/m, the relaxation peak becomes hidden as the dc conductivity term dominates the RHS of Eq. 2.18. This indicates that the dielectric relaxation peaks may be difficult to discern in measurements on high-conductivity samples.

2.3.4 Dielectric relaxation in polymers

A polymeric material is a collection of polymer chains, and a polymer chain is made of repeated monomers. This means that the net dipole moment per unit volume, or polarization vector, of a polymer is given by the dipole moment of a monomer, summed over all monomers in a polymer chain, then summed over all polymer chains. The polarization of a polymer can be written as [10]

$$\mathbf{P} = \frac{1}{V} \sum_{allchains} \sum_{chain} \mu_{\mathbf{i}}, \tag{2.19}$$

where μ_i is dipole moment of a monomer.

The total polarization of a polymer material thus depends on a range of length scales, from the size of a few atoms up to the full chain length. As a result, one expects more than one dielectric relaxation process in a polymer, with larger regions relaxing more slowly than small regions. Each process is typically characterized by a peak in the dielectric loss spectrum and a step-like decrease in ε' as described by the Debye model in Eq. 2.13 and shown in Figs. 2.3 and 2.4.

In practice, the relaxation spectrum is typically dominated by two processes: one corre-

sponding to the relaxation of short segments of the polymer and the other to long segments or whole chains. These two processes, known as α relaxation and β relaxation, are observed in most amorphous polymers. α relaxation is also known as the principal relaxation and β as the secondary relaxation. The well-accepted explanation for the β relaxation is variation of the local dipole moment vector due to the movement of small regions of the main polymer chain, and/or rotations of side groups [10]. Since the β relaxation involves the motion of small regions, it is relatively fast and so appears in the relaxation spectrum at high frequencies. In contrast, the α relaxation is caused by the reorientation of entire chains or longer chain segments. As these motions happen over a larger length scale, the α relaxation process is much slower than the beta process and appears at lower frequencies in the relaxation spectrum. Both relaxation processes are temperature sensitive. This behaviour has been seen in polymer nanocomposites, for example by Carroll et. al. [9], who analyzed the dielectric spectra of poly(vinyl acetate)-SiO_2 nanocomposites. In reality, these relaxation processes do not result in simple Debye peaks in the relaxation spectrum, because both involve a broad range of segment lengths and relaxation times.

Dielectric relaxation can be also studied by taking measurements at a fixed frequency as a function of temperature. In this case, a relaxation process gives a peak in ε'' versus temperature and a step-like decrease in ε' versus temperature.

2.4   Rheology of viscoelastic materials

Rheology is the study of flow and deformation of materials [11]. Rheology focuses on studying the mechanical response of complex fluids to external forces, and on understanding the relationship between the mechanical properties of materials and their microstructure.

2.4.1 Basics of rheology
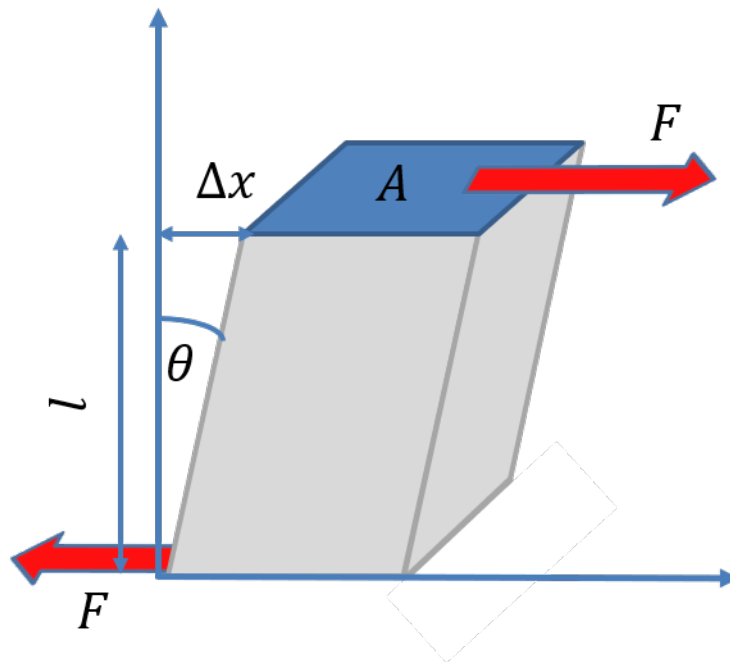
Figure 2.7: Deformation of a material with a shear stress applied.

Figure 2.7 indicates the deformation θ of a material subjected to a shear force F parallel to its top and bottom surfaces. The shear stress τ is defined as

$$\tau = \frac{F}{A},\tag{2.20}$$

where A is the cross-sectional area. The shear strain of the material is

$$\gamma = \frac{\Delta x}{l} \approx \theta.\tag{2.21}$$

In general, when a stress is applied to a solid, it quickly deforms then returns to its original shape upon removal of the stress. This is called elastic behaviour. For small strain, elastic materials show a linear relationship between stress and strain in accordance with Hooke's law,

$$\tau = G\gamma,\tag{2.22}$$

where G is elastic modulus. On the other hand, a liquid continuously flows as long as the stress is present and does not return to its undeformed state when the stress is removed. This response is called viscous behaviour. In the simplest case, fluids show a linear relationship between the shear stress and the shear rate $\dot{\gamma}$, the time derivative of the shear strain. Fluids that display this behaviour are termed Newtonian fluids and follow Newton's law of viscosity,

$$\tau = \eta\dot{\gamma}, \qquad (2.23)$$

where η is the viscosity of the fluid.
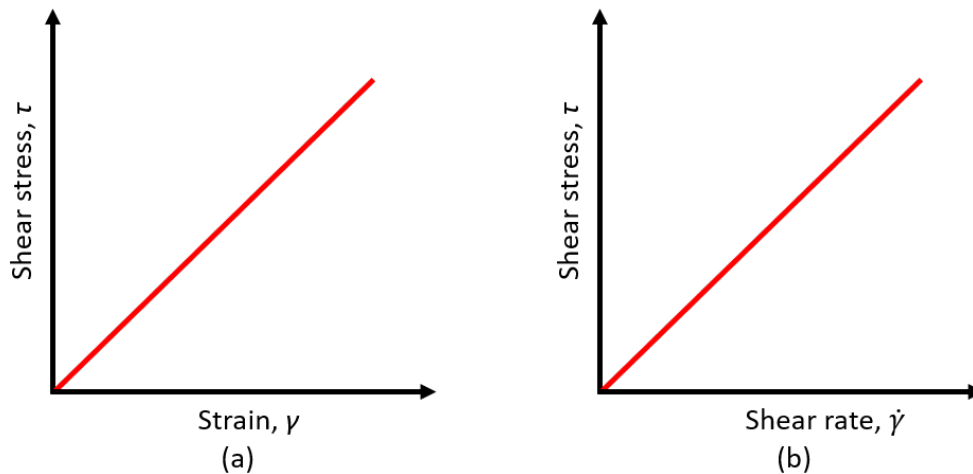
Figure 2.8: Ideal rheological behaviour. (a) pure elastic element, (b) pure viscous element.

Figure 2.9 categorizes some types of fluid according to the way in which stress depends on shear rate. If the slope of the stress vs. shear rate curve increases with increasing shear rate, the viscosity of the fluid also increases with shear rate and the fluid is said to be shear-thickening. Shear-thickening is found mostly in highly concentrated dispersions of particles. A simple example of shear-thickening is a highly concentrated suspension of sand in water. At a low shear rate, viscosity is low as the water acts as a lubricant, reducing the friction between sand particles. However, at higher shear rates, the water does not completely fill the gaps between the particles, causing the particles to come into contact with each other. This leads to

23

comparatively high friction between the particles, increasing the viscosity at high shear rates [12]. Shear-thickening often signals phase separation and lack of reversibility of a material.

Similarly, if the viscosity decreases with the shear rate as shown in Fig. 2.9, the fluid is called shear-thinning. Many polymeric solutions, blood, and ketchup are examples of shear-thinning fluids [11]. Shear-thinning results from changes in the microstructure of the material that take place under shear. For example, when a concentrated polymer solution is at rest or sheared at a low rate, extensive entanglement of the polymer chains leads to a high viscosity. When the polymer solution is strongly sheared, uncoiling and disentanglement of polymer chains takes place, reducing the viscosity.
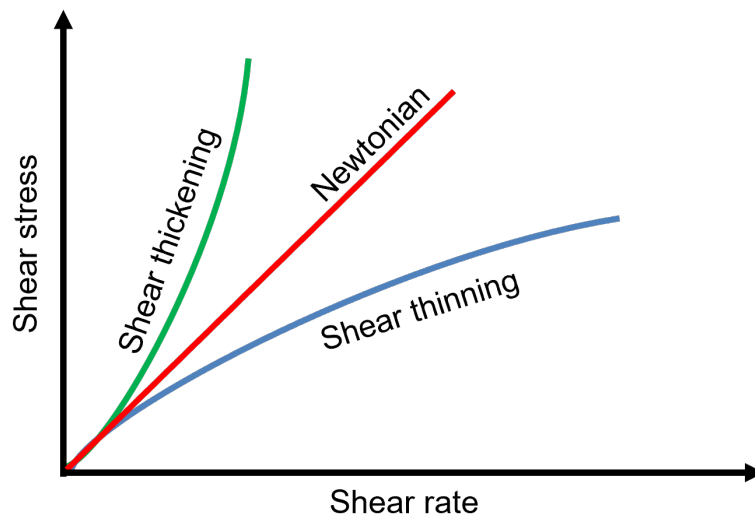
Figure 2.9: Stress as a function of shear rate for various types of fluids.

2.4.2 Oscillatory Measurement

Oscillatory measurements can be used to study the viscoelastic properties of complex fluids. Here, we consider the case in which a periodic stress is applied to a sample and its strain is measured. One can also apply a periodic strain and measure the stress. If the periodic stress is

$$\tau = \tau_0 \cos(\omega t), \tag{2.24}$$

24

then from Eq. 2.22, the strain for an elastic solid is

$$\gamma = \frac{\tau}{G} = \gamma_0 \cos(\omega t), \tag{2.25}$$

where $\gamma_0 = \tau_0/G$. From Eqs. 2.24 and 2.25, it is clear that there is no phase difference between stress and strain in an elastic material.

The shear rate from Eq. 2.24 and Eq. 2.23 for a viscous fluid under the same periodic stress is

$$\dot{\gamma} = \frac{\tau}{\eta} = \frac{\tau_0 \cos \omega t}{\eta}. \tag{2.26}$$

By integrating Eq. 2.26, the strain can be written as

$$\gamma = \gamma_0 \cos\left(\omega t - \frac{\pi}{2}\right), \tag{2.27}$$

where $\gamma_0 = \tau_0/\eta\omega$. Therefore, in a viscous fluid, the strain is 90° out of phase with the applied stress. The phase difference δ in a viscoelastic material will lie between these two ideal cases, i.e., between 0 and 90° [12]. For a viscoelastic material, the strain can be written as

$$\gamma = \gamma_0 \exp\left(i(\omega t - \delta)\right). \tag{2.28}$$

The complex modulus G^* is defined as

$$G^* = \frac{\tau}{\gamma} = \frac{\tau_0 \exp\left(i\omega t\right)}{\gamma_0 \exp\left(i(\omega t - \delta)\right)} \tag{2.29}$$

so that,

$$G^* = G' + iG'' = \frac{\tau_0 \exp\left(i\delta\right)}{\gamma_0}. \tag{2.30}$$

where G' and G'' are the storage modulus and loss modulus, respectively, and characterize the elastic and viscous components of the material's mechanical response. In fact, the real part of

Eq. 2.30 is

$$G' = \frac{\tau_0 \cos \delta}{\gamma_0}. \tag{2.31}$$

The imaginary part of Eq. 2.30 is

$$G'' = \frac{\tau_0 \sin \delta}{\gamma_0}. \tag{2.32}$$

One can develop simple mechanical models in an effort to explain the viscoelastic behaviour of materials [11, 12]. These models use ideal springs to represent Hookean deformation and dashpots to represent Newtonain flow. Here we discuss a few models starting with the simple Maxwell model.

The Maxwell model
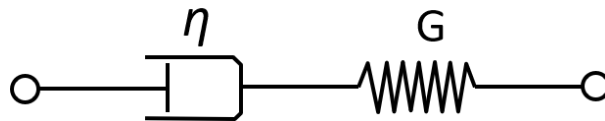
Figure 2.10: The Maxwell model.

The Maxwell model describes a material as a series combination of a spring element and a dashpot element as shown in Fig. 2.10. The stress on each individual element is the same as the overall applied stress and the total strain is the sum of the strains of the two elements. From this, the stress-strain relationship for the Maxwell model can be derived as

$$\tau + \lambda \dot{\tau} = \eta \dot{\gamma}, \tag{2.33}$$

where $\lambda_M = \eta/G$ is called the relaxation time. Solving this equation for the stress as a function of time shows that the stress depends on both the strain and the shear rate. Therefore, this model incorporates both viscous and elastic behavior.

If we consider a sinusoidally varying stress as in Eq. 2.24, one can show that G' and G'' can

be written as

$$G' = \frac{\eta \lambda_M \omega^2}{1 + (\omega \lambda_M)^2} \tag{2.34}$$

and

$$G'' = \frac{\eta \omega}{1 + (\omega \lambda_M)^2}. \tag{2.35}$$
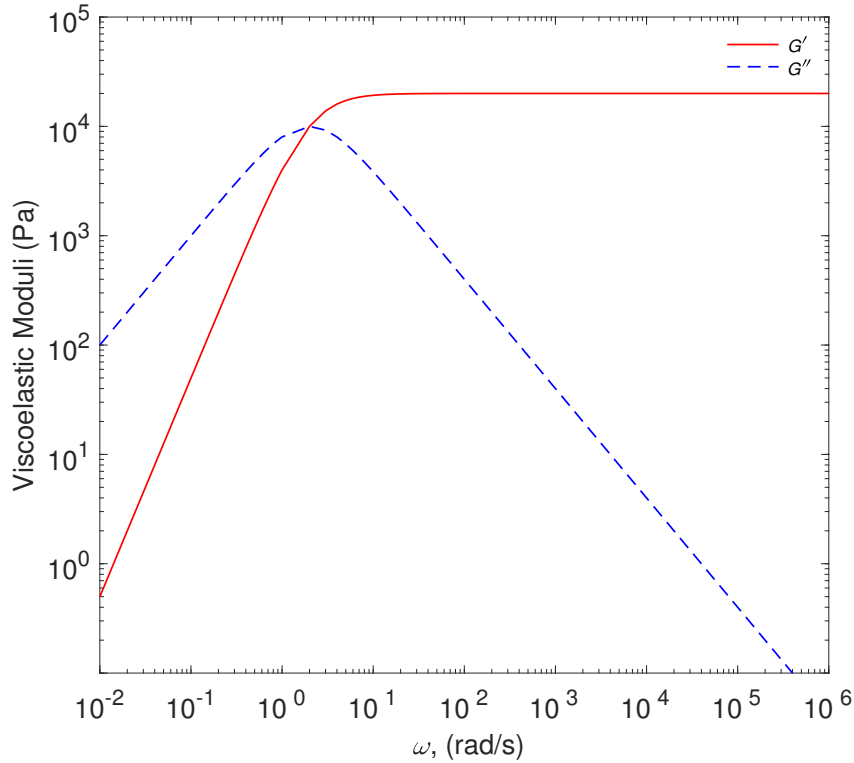
Figure 2.11: The behaviour of G' and G'' in the Maxwell model with $\eta = 10^4$ Pa.s and $\lambda_M = 0.5$ s.

Figure 2.11 is a plot of the viscous and elastic moduli for a Maxwell model assuming $\eta = 10^4$ Pa·s and $\lambda_M = 0.5$ s. The crossover of G' and G'' occurs at an angular frequency equal to the inverse of the relaxation time.

The Kelvin-Voigt model

The Kelvin-Voigt model also uses the ideal spring and dashpot elements shown in Fig. 2.8. In this case they are connected in parallel as shown in Fig. 2.12. In this model, the strain on each
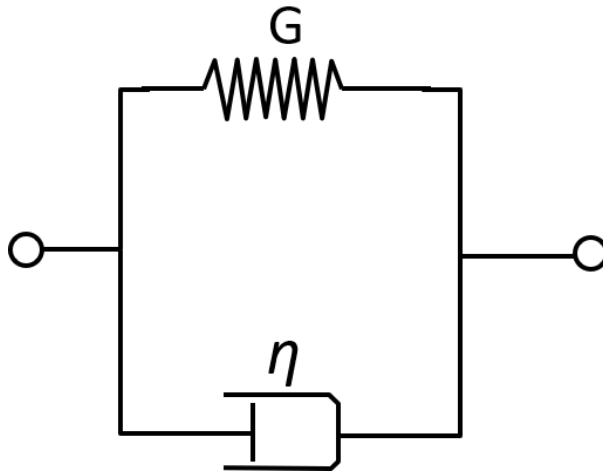
Figure 2.12: The Kelvin-Voigt model

element is the same, while the total stress is equal to the sum of the stress on each of the two elements. The stress-strain relationship for this model is

$$\tau = G\gamma + \eta\dot{\gamma}. \tag{2.36}$$

The stress in the Kelvin equation depends on both the strain and strain rate, illustrating viscoelastic behaviour of a material.

Relaxation experiment using a Maxwell model

As an example of the applicability of these models, imagine that a constant non-zero strain is applied to a material described by the Maxwell model and its stress is measured as a function of time. Since the shear rate is zero, Eq. 2.33 simplifies to

$$\tau + \lambda\dot{\tau} = 0. \tag{2.37}$$

Rearranging and integrating Eq. 2.37, the stress can be written as

$$\tau(t) = \tau_0 \exp\left(-t/\lambda\right). \tag{2.38}$$

The Maxwell model thus predicts that the stress decays exponentially with time when subjected to a constant strain. This is approximately true for most polymers as long as the applied strain is small enough. On the other hand, the predictions of the Maxwell model are incorrect if one considers applying a constant stress to the material — the model then predicts a constant strain rate, while in reality the strain rate decreases with time.

Creep relaxation/recovery experiment using Kelvin-Voigt model

In a creep experiment, a material is placed under constant stress for a long time and then the stress is suddenly removed at time $t = 0$. The strain is then measured as a function of time. For the Kelvin-Voight model with $\tau = 0$, Eq. 2.36 becomes

$$G\gamma + \eta\dot{\gamma} = 0. \tag{2.39}$$

Rearranging and integrating Eq. 2.39, we find

$$\gamma = \gamma_0 \exp\left(-t/\lambda'\right), \tag{2.40}$$

where $\lambda' = \eta/G$ is called the retardation time. This model can successfully describe creep in simple materials.

2.4.3 Complex viscoelastic materials

The Maxwell and Kelvin-Voigt model models both incorporate a single relaxation time. However, complex materials such as nanocomposites have more than one relaxation process and these simple models are unable to realistically model their behavior. More complex models can be developed by adding additional springs and dashpots to these simple models.

Burgers model
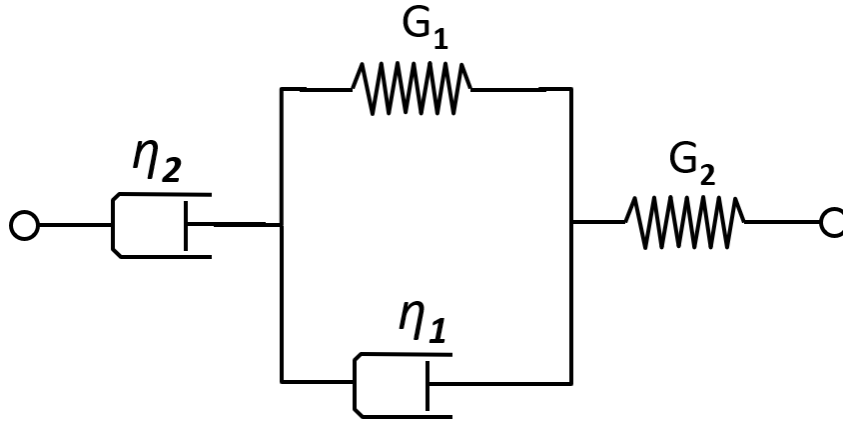
Figure 2.13: Schematic of the Burgers model

Figure 2.13 shows a schematic diagram of the Burgers model, which is a combination of the Maxwell model and the Kelvin-Voigt model. In this model, creep strain is given as a function of time t by

$$\gamma(t) = \frac{\sigma_0}{E_M} + \sum_{i=1}^{2} \frac{\sigma_0}{E_{ki}} \left[1 - exp\left(\frac{-t}{\tau_i}\right) \right] + \frac{\sigma_0 t}{\eta_M}, \tag{2.41}$$

where σ_0 is the applied constant stress. The first term of the equation represents the elastic (instantaneous) deformation corresponding to the spring of the Maxwell model with elastic modulus E_M, the second term indicates two delayed viscoelastic deformations corresponding to the Kelvin-Voigt model with relaxation times τ_i and elastic modulus E_{ki}, and the third term represents Newtonian flow behaviour corresponding to the sliding of the Maxwell dashpot with steady state viscosity η_M. This model has been of interest among researchers to describe the creep behaviour of composites [13, 14]. In Chapter 5, we determine these rheological properties by fitting our experimental creep strain data to Eq. 2.41.

Weibull distribution equation

We use the Weibull distribution equation [13, 14] to interpret the creep recovery data obtained in Chapter 5. In this distribution, the recovery strain is given by

$$\gamma_r(t) = \sum_{i=1}^{3} \gamma_{vi} \left[exp\left(-\left(\frac{t - t_0}{\tau_{ri}} \right) \right) \right] + \gamma_\infty,$$ (2.42)

where γ_{vi} and τ_{ri} are viscoelastic strain recovery and characteristic life time respectively. t_0 is the time when the applied stress in creep was removed, and γ_∞ is the permanent strain at $t \to \infty$ due to the viscous flow effect.

2.5   Shear Rheometry

Our rheological experiments were performed using a rotational shear rheometer. This instrument can be operated in a strain-controlled mode — in which a known shear strain is applied to the sample, and the resulting stress measured — or in a stress-controlled mode — in which a known stress is applied and the strain measured. We performed both strain-controlled and stress-controlled experiments for this work, as explained in Chapter 3. Some common measurement geometries used in the shear rheometer are shown in Figure 2.14. The optimum geometry for a given measurement depends on the nature of the material being tested. For example, a concentric cylinder tool would be ideal for measurements on a low-viscosity fluid. We used a parallel-plate geometry for our study because our samples are circular disks.

A shear rheometer does not measure most of the rheological parameters directly. Instead, it measures the torque M on the tool used and the angular displacement θ of the tool. Then, knowing the geometry of the measurement tool, the shear stress and shear strain can be calculated from these quantities. For a cone-and-plate geometry the stress can be calculated as

$$\tau = \frac{3M}{2\pi R^3},$$ (2.43)

31

where R is the radius of the tool. The shear strain is given by

$$\gamma = \frac{\theta}{\beta}, \tag{2.44}$$

where β is the cone angle. Shear rate $\dot{\gamma}$, which is the time derivative of γ, is given by

$$\dot{\gamma} = \frac{\omega}{\beta}, \tag{2.45}$$

where ω is the angular frequency of the tool. The shear rate is constant throughout the sample in the cone-and-plate geometry.

In the parallel-plate geometry, the top plate rotates with angular frequency ω and the bottom plate is held fixed. If the height of the sample is h, the shear rate $\dot{\gamma}$ can be expressed as

$$\dot{\gamma} = \frac{\omega r}{h}, \tag{2.46}$$

where r is the radial distance from the center of the top plate [11]. It is interesting to note that the shear rate linearly increases with r and the highest $\dot{\gamma}$ exists at the edge of the plate. Calculation of the shear stress in the parallel-plate geometry is not simple as in cone-and-plate geometry. [11].
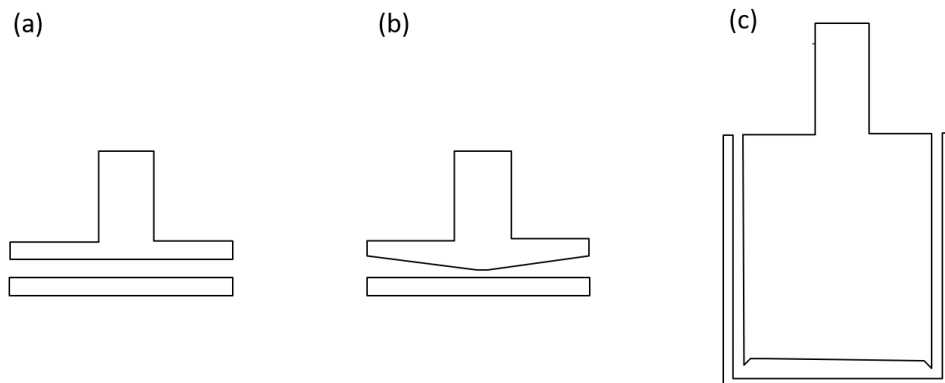
Figure 2.14: Common geometries used in shear rheometry. (a) Parallel Plate, (b) Cone-and-Plate, and (c) Couette, or concentric cylinder, geometry [11]

2.6 The analogy between dielectric and rheological measurements

There are many similarities between dielectric and rheological measurements. In frequency-domain measurements, both techniques use spectroscopy to examine small scale dynamics of a material. In dielectric measurements, the electrical response of a material to an external electric field is studied. Rheology focuses on studying the mechanical response of a material to external forces. Both techniques are used to understand the material's microstructure. Dielectric spectroscopy can be used to study dynamics of a material at very different time scales compared to rheometry as dielectric spectroscopy is capable of measurements from the microhertz to megahertz frequency range and rheometer from millihertz to hundreds of hertz. Therefore dielectric measurements can be used to study monomer-scale dynamics, molecular dynamics and long polymer chain dynamics. On the other hand, a rheometer is capable of studying large time scale dynamics such as polymer chain dynamics.

Another similarity is that the mathematical treatment is exactly the same for both techniques. In both cases we are applying a linear perturbation to the system and measuring its response. In both cases, there is a real (energy storage) and an imaginary (energy dissipation) part of the response. The difference is that in the rheological case, storage is in the elastic deformation of the material, and in dielectric case storage is in the electric dipole configuration. In both cases the dissipation is due to polymer motions on different length and time scales.

From a mathematical point of view, the Maxwell model in rheology is exactly analogous to the Debye model for dielectric relaxation.

Bibliography

[1] N. N. Getangama. *Dielectric Spectroscopy of Polyvinyl alcohol Hydrogels and Nanocomposites*. MSc thesis, The University of Western Ontario, London, Ontario, Canada, 2015.

[2] T. Blythe and D. Bloor. *Electrical Properties of Polymers*. Cambridge University Press, 2005.

[3] J. Jackson. *Classical electrodynamics*. Wiley, 1975.

[4] A. Chelkowski. *Dielectric Physics*. Polish Scientific, 1980.

[5] R. Buchner, J. Barthel, and J. Stauber. *Chem. Phys. Lett.*, 306:57, 1999.

[6] K.S. Cole and R. H. Cole. *J. Chem. Phys.*, 9:341, 1941.

[7] M. Eesaee, E. David, and N. R. Demarquette. *Polym. Eng. Sci.*, 60:968, 2020.

[8] M. Füllbran, P. J. Purv, and A. Schönhal. *Macromol.*, 46:4626, 2020.

[9] B. Carroll, S. Cheng, and A. P. Sokolov. *Macromol.*, 50:6149, 2017.

[10] J. P. Runt and J. J. Fitzgerald. *Dielectric Spectroscopy of Polymeric Materials*. American Chemical Society, 1997.

[11] C. W. Macosko. *Rheology Principles, Measurements, and Applications*. Willey-VCH, Inc, 1994.

[12] J. Ferguson and Z. Kemblowski. *Applied Fluid Rheology*. Elsevier science publishers LTD, 1991.

[13] K. S. Fancey. *J. Mater. Sci.*, 40:4827, 2005.

[14] X. Wang, L. Gong, L. Tang, K. Peng, Y. Pei, L. Zhao, L. Wu, and J. Jiang. *Compos. - A: Appl. Sci. Manuf.*, 69:288, 2015.

Chapter 3

Experiment

3.1 Overview

Here we describe the materials, apparatus, and experimental procedures used in our work.

3.2 Materials

3.2.1 Polyethylene oxide

Polyethylene oxide (PEO), also known as polyethylene glycol (PEG), is a crystalline, thermoplastic, water soluble polymer. It is commercially available in a wide range of molecular weights, ranging up to millions. Higher molecular weight PEO can be formed into tough, molded shapes. The structure of PEO is shown in Figure 3.1. It consists of n CH_2-CH_2-O monomers, and each repeating unit has a dipole moment due to the polarization of C-O bond. The total dipole moment of a macroscopic sample of PEO and its polarization vector can be calculated as explained in Section 2.3.4.

For our work, white and odorless PEO powder with molar mass 100,000 g/mol was purchased from Sigma-Aldrich Co (product number: 181986) and used as received. The melting point and glass transition temperature of PEO used in our work are 65 and $-67\,°C$ respectively.[1]
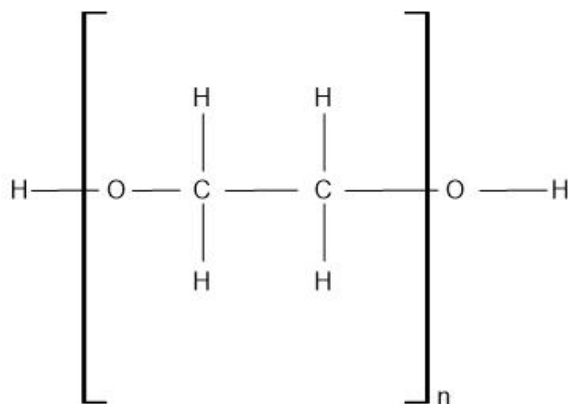
Figure 3.1: Chemical structure of PEO.

3.2.2 Polystyrene

Polystyrene (PS) is one of the most commonly used and inexpensive polymers in the world. Several million tonnes are produced annually worldwide. At room temperature, it is a transparent polymer made by polymerization of the styrene monomer shown in Figure 3.2. When PS is above its glass transition temperature (between 123 and 128 °C), it is soft enough for injection molding or extrusion. The styrene monomer has a weak dipole moment due to the presence of the phenyl side group. This weak polarization leads to a small dielectric constant in PS.

For our research, clear and odorless PS beads with molar mass 35,000 g/mol were purchased and used as received from Sigma-Aldrich Co (product number: 331651).
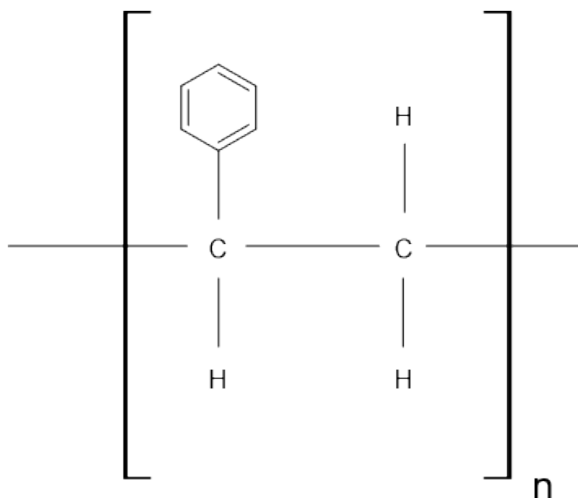
Figure 3.2: Chemical structure of PS.

3.2.3 Carbon nanotubes

Carbon nanotubes can be thought of as graphene sheets rolled up into cylinders. Single-walled carbon nanotubes consist of a single such cylinder, while multi-walled carbon nanotubes (MWCNT) consist of several concentric cylinders. We made the polymer nanocomposites studied in this thesis by adding MWCNT to the molten polymer. We used MWCNT concentrations ranging from 0 to 5% by weight. The MWCNT used in this work had diameter 8–15 nm, length 30–50 μm, and purity > 95%. They were purchased from TimeNano Chengdu Organic Chemicals and used as received.

3.3 Sample preparation

Two mixing methods were used to prepare our PEO-MWCNT nanocomposites. PS-MWCNT were made using twin-screw extrusion, while PEO-MWCNT nanocomposites were prepared by both twin-screw extrusion and melt-mixing. Both PEO-MWCNT and PS-MWCNT composite mixtures were compression molded to produce the final sample disks as described below. PEO-MWCNT and PS-MWCNT nanocomposites samples were made with MWCNT concentrations ranging from 0 to 5 wt%.

3.3.1 PEO-MWCNT: Melt-mixing

The PEO powder and MWCNT were used as received. 50 g of PEO and the required amount of MWCNT were added to a Brabender three-piece mixer equipped with two counter-rotating blades and preheated to 75 °C. The material was mixed for 10 minutes by the blades in the mixer before being cooled down to room temperature. The resulting composite mixture was pelletized to a size suitable for the compression molding process described below.

3.3.2 PEO-MWCNT: Twin-screw extrusion

In the second method, PEO-MWCNT nanocomposites were prepared using a Thermo Scientific HAAKE MiniLab II twin-screw micro-compounder. 4.5 g of PEO and the required amount of MWCNT were added to the twin-screw mixer, which was preheated to 75 °C. The material was mixed for 10 minutes at a screw speed of 50 rpm before the mixture was extracted and cooled down to room temperature. The extracted material was in the form of a long ribbon, about 5 mm in width and 1 mm thick, which was pulverized prior to compression molding.

3.3.3 PS-MWCNT: Twin-screw extrusion

4.5 g of PS and the required amount of MWCNT were added to the twin-screw mixer, which was preheated to 125 °C. The material was mixed for 10 minutes at a screw speed of 50 rpm before the mixture was extracted and cooled down to room temperature. The extracted material from twin-screw extrusion was in the form of a long ribbon, about 5 mm in width and 1 mm thick, which was pulverized prior to compression molding.

3.3.4 Compression molding of nanocomposite disks

Circular disks 1 mm thick and 25 mm or 50 mm in diameter were made by transferring the small pieces of nanocomposite prepared as above to a room temperature mold made from 3.2 mm thick aluminum plates, separated by a 1 mm thick aluminum gasket with 25 and 50 mm diameter holes in it. Then the filled mold was placed in a preheated compressor from Carver Inc. [2]. It was allowed to sit for 5 minutes, then compressed under 13.3 kN of force for 5 minutes. The disks were removed from the mold after the mold had cooled down to room temperature. For the PEO-MWCNT nanocomposites, the compressor was preheated to 75 °C. For the PS-MWCNT nanocomposites, the preheating temperature was 125 °C.

As we made PEO/MWCNT nanocomposites using two mixing methods, we use the following notation to identify our samples: PEO/MWCNT nanocomposites prepared by melt-mixing

are labeled by an M followed by the amount of MWCNT added, given as a percentage of the total sample weight, while those prepared by twin-screw extrusion are labeled by T followed by the wt% MWCNT. Thus, for example, M1.0 refers to a melt-mixed sample containing 1.0 wt% MWCNT. Samples of pure PEO, made in the melt mixer only, are referred to as M0.0. Also, PS/MWCNT samples are labeled by a PS followed by the amount of MWCNT added, given as a percentage of the total sample weight. For example, PS1.0 wt% refers to a twin-screw extrusion sample containing 1.0 wt% MWCNT.

Figure 3.3 shows a 25 mm diameter M3.0 disk prepared by melt mixing and compression molding as discussed above. All the nanocomposite samples are black even for the lowest MWCNT concentration. They are stiff and the surfaces are smooth.
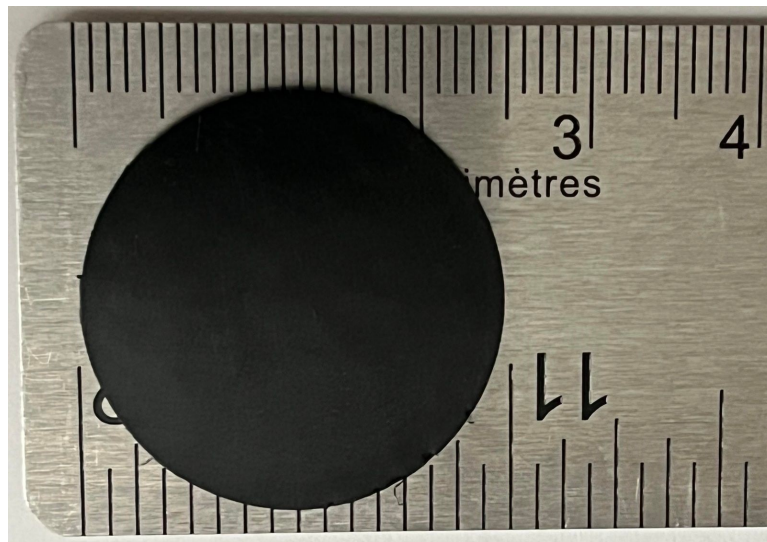
Figure 3.3: 25 mm diameter M3.0 disk prepared by melt mixing and compression molding as described in the text.

3.4   Dielectric spectrometer

The dielectric spectrometer consists of the material test system (MTS), the cryostat and cooling system, and the temperature controller as shown in Figure 3.4.
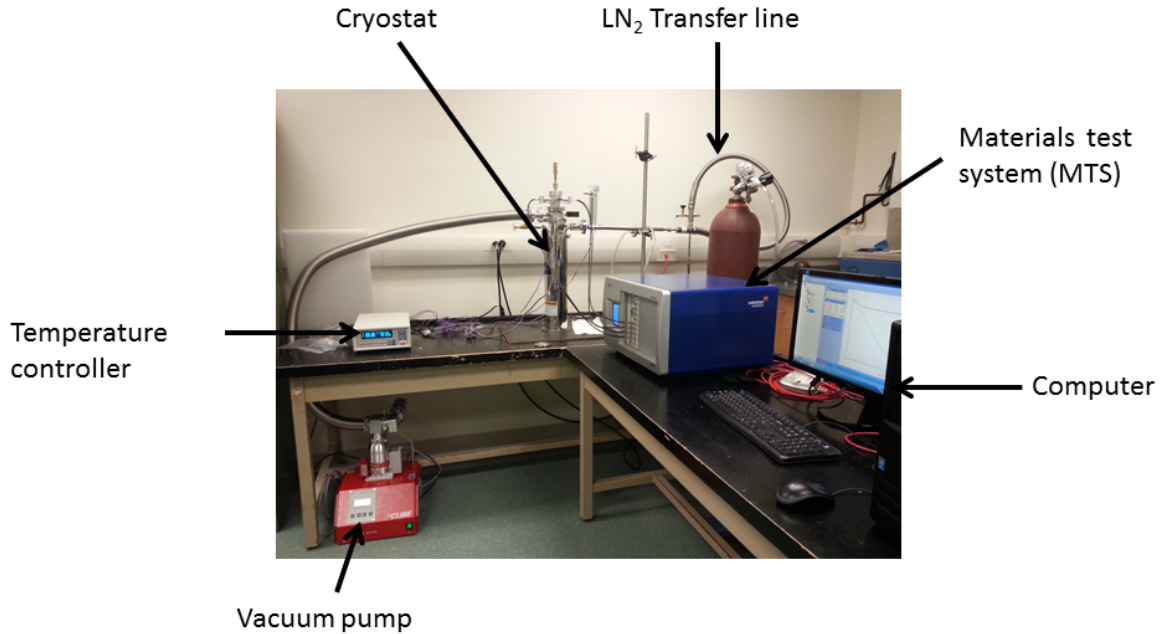
Figure 3.4: Main components of the dielectric spectrometer: the MTS, the cryostat and cooling system, and the temperature controller. The computer communicates with the MTS and the temperature controller while collecting data [3].

The Solartron Modulab Materials Testing System is the blue box shown in Figure 3.4. This is the actual dielectric spectrometer instrument. A computer communicates with the MTS and the temperature controller via an ethernet connection. The MTS can be used to perform both direct current (DC) and alternating current (AC) measurements.

In DC measurements, a constant voltage is applied across the sample and the MTS measures the corresponding current density J.

For AC measurements, the MTS generates a sinusoidal voltage across the sample and the resulting current and phase angle are measured by the MTS. The MTS software then calculates the desired dielectric quantities.

The sample cell is contained inside the cryostat, which is used to allow variation of the sample temperature. A cross section of the cryostat is shown in Figure 3.5. The cryostat consists of three concentric stainless steel cylinders. The space between the outer two cylinders is a vacuum jacket which was evacuated to a pressure of 5×10^{-4} Torr or less using a turbo-

pump prior to every experiment. The inner cylinder, in which the sample cell resides, is filled with helium exchange gas at a pressure of 1 PSI to maintain good heat transfer to the sample.
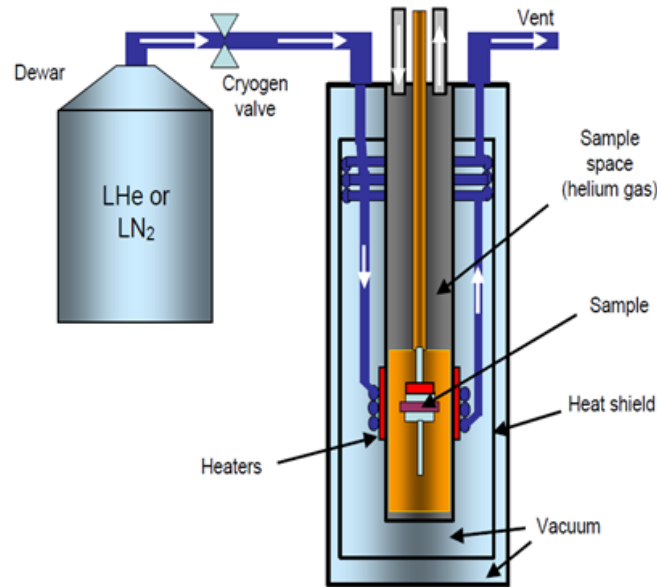
Figure 3.5: A cross section of the cryostat showing the main components inside the cryostat and their organization [3, 4].

The sample holder in the cryostat is a parallel-plate capacitor, which is made of two brass disks 10 and 25 mm in diameter. The capacitor is designed to have a uniform electric field across the sample when a voltage is applied across the capacitor. Therefore, the effective diameter of the capacitor is 10 mm. The sample can be heated when needed by two electric heaters, one mounted near the sample and the other mounted on the outer surface of the inner cylinder. Two thermocouples measure the sample temperature and the temperature of the surrounding area. The sample can be cooled by flowing cold nitrogen gas into the space between the middle and inner cylinders. The sample temperature is controlled by a Lake Shore Model 335 Cryogenic Temperature Controller [5] to an accuracy of 0.01 K by balancing the heating and the cooling due to the cold gas.

In our dielectric measurements on polymer nanocomposites, we measured the real and imaginary parts of the permittivity, as well as the DC conductivity as a function of temperature and nanotube concentration. The MTS control software is used to operate the dielectric spec-

trometer and collect data. The experimental data were exported as text files from the software and analyzed using Matlab.

3.4.1 Dielectric procedure

A 25 mm disk of the nanocomposite under study was placed in between the plates of the measuring capacitor of the dielectric spectrometer described in Section 3.4. The cryostat was sealed and evacuated, and nitrogen gas for cooling was allowed to flow from a storage dewar of liquid nitrogen. Once the desired sample temperature was reached, the system was allowed to equilibrate for 20 minutes before data collection was started.

In DC measurements, the voltage across the sample V_{dc} was swept from 0 to 4 V at a rate of 100 mV/s and the corresponding current density $J_{dc} = I_{dc}/A$, where A is the cross-sectional area of the sample, was measured. At low applied voltages, the samples are Ohmic, with $J_{dc} \propto V_{dc}$. Knowing the sample thickness ℓ, σ_{dc} is then simply given by

$$\sigma_{dc} = \frac{\ell}{A}\frac{dI_{dc}}{dV_{dc}}. \tag{3.1}$$

For our AC measurements, the MTS generates a sinusoidal voltage with 4 V amplitude across the sample. The frequency is swept from 0.1 Hz to 1 MHz. Then the resulting current is measured by the MTS, which calculates the desired dielectric quantities. Measurements were performed from 300 to 180 K for the PEO/MWCNT nanocomposites and 360 to 300 K for the PS/MWCNT nanocomposites. We determine the dielectric properties of our nanocomposites by fitting the empirical Havriliak-Negami (HN) model introduced in Eq. 2.18 to the imaginary part of the frequency-dependent data obtained from the AC experiments.

3.5 Shear Rheometer

We used the Anton-Paar MCR-302 rotational shear rheometer shown in Figure 3.6 to take rheological measurements. This is a stress-controlled rheometer, but its control software allows it to operate in strain-controlled modes as well. A stress-controlled rheometer applies a known torque to the rheometer tool, calculates the corresponding applied shear stress, and measures the resulting rotational deformation (or strain) of the material in the tool. When it operates in a strain-controlled mode, the control software continuously adjusts the applied torque to achieve a user-defined strain of the sample, and the corresponding shear stress on the tool is extracted [6]. The rheometer does not directly measure the rheological parameters. For example, it measures the angular displacement of the parallel-plate tool for a known applied torque. Other properties such as elastic and viscous moduli are extracted from the calculated stress and strain.

We used a 50 mm diameter parallel-plate geometry tool for our rheological measurements as our PEO nanocomposites samples are in the form of disks. The temperature of the sample is controlled to an accuracy of $0.01\,°C$ by a Peltier-plate heater on the bottom plate of the rheometer tool. A temperature-controlled environmental housing covers the rheometer tool to minimize thermal gradients across the sample. RHEOPLUS software is used to control the rheometer, collect data, and calculate the required rheological parameters. The experimental data were saved as text files from the software and analyzed using Matlab.

3.5.1 Rheology procedure

The rheological properties of our PEO/MWCNT samples were measured using the shear rheometer described above with a 50 mm diameter parallel plate tool. A roughened bottom plate was used and a 50 mm diameter disk of 280 grit sandpaper was attached to the top plate to minimize slip between the sample and the tool. As the temperature of the sample is increased, it goes through its melting transition. As a result, its volume changes. To accommodate this, we set the rheometer to maintain a constant normal force on the top plate, rather than the
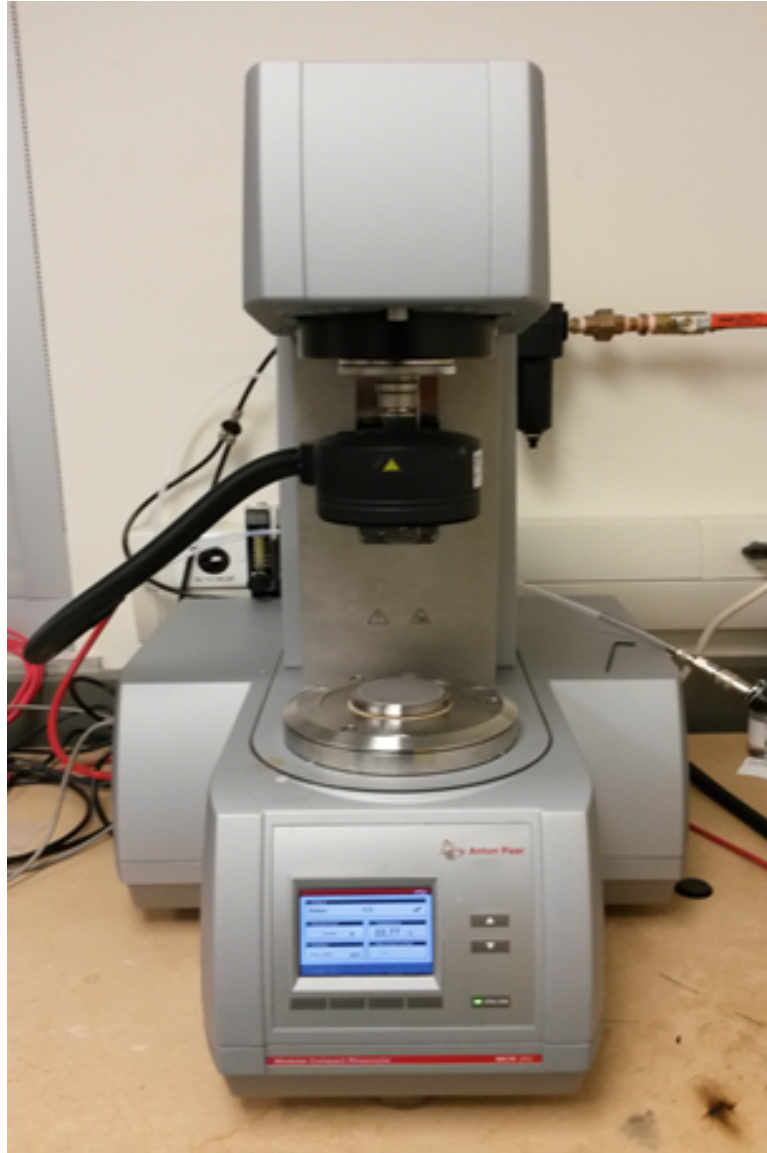
Figure 3.6: Shear rheometer used in the experiments.

more usual constant gap. As a result of this, the gap changes slightly over the course of the experiments. This change is taken into account by the software.

A PEO/MWCNT nanocomposite disk 50 mm in diameter and 1 mm thick was carefully centered in the rheometer tool and the upper plate was lowered until the normal force reached the desired value. Then the environmental housing was lowered over the tool. The rheometer was set to the desired temperature and held at that temperature for 15 minutes to ensure equilibrium before performing the experiments. PEO and the PEO/MWCNT nanocomposites were

solid at 60 °C but softened and melted as the temperature was increased. As a result, some of the material properties depend strongly on temperature. We raised the sample temperature from 60 to 85 °C in 5 °C increments, then lowered it back to 60 °C, again in 5 °C steps. We waited 15 minutes at each step for the sample temperature to equilibrate. The temperature was cycled in this way up to four times for a given experiment, with data collected at each temperature step.

Frequency sweep

Frequency sweep experiments were used to measure the viscous and elastic moduli of our PEO/MWCNT nanocomposites. First, the extent of the linear viscoelastic regime, in which G' and G'' are independent of the amplitude of the applied shear strain, was determined by applying a strain amplitude sweep at a frequency of 6.28 rad/s. We found that the PEO/MWCNT nanocomposites were in the linear viscoelastic regime when the amplitude of the applied strain was less than 5%. The frequency sweep experiments were performed using a strain amplitude of 0.5%, which is well within the linear regime.

Once the sample reached desired stable temperature as explained above, a sinusoidal strain with 0.5% amplitude was applied to the sample. The frequency was increased in logarithmically-spaced steps from 0.1 to 100 rad/s. The elastic and viscous modulus, G' and G'' respectively, were measured at each frequency. The wait time at each step was decreased from 100 s at the lowest frequency to 10 s at the highest. For a given MWCNT concentration, the same sample was used for all temperatures and temperature cycles.

Creep recovery experiments

Our nanocomposite's response to an external stress was studied using creep and creep recovery experiments. A new set of samples was used for these experiments. We wished to keep the deformation of the samples small, i.e., within the linear viscoealstic regime throughout these experiments. To ensure this, each sample was first heated to 70 °C, a series of stresses was applied, and the resulting strain was measured. Based on these results, the stress σ_0 to be

45

Table 3.1: The stress σ_0 used for each sample in the creep experiments.

Sample	σ_0 (Pa.s)
M0.0	0.08
M1.0	0.3
M2.0	4.0
M3.0	2.0
M5.0	55

used in the creep experiments was chosen so that the maximum strain was few percent. The values of σ_0 used for each MWCNT concentration are shown in Table 3.1. After σ_0 had been determined, the sample was cooled down back to $60\,°\text{C}$ and the first cycle of the creep experiment was started. When the desired temperature was reached as explained above, the stress σ_0 was applied to the sample for 15 minutes and the corresponding strain γ was measured as a function of time. After 15 minutes of creep, the stress was set to zero to start the recovery portion of the experiment, and the unrecovered strain was measured for another 15 minutes as the sample relaxed.

The data from the creep phase of the experiment were fitted to the Burger's model introduced in Eq. 2.41 to extract the relaxation times τ and the steady state viscosity η_M. The recovery data was fitted by the Weibull distribution introduced in Eq. 2.42 to obtain the characteristic recovery time τ_r and the permanent strain γ_∞.

Bibliography

[1] https://www.sigmaaldrich.com/ca/en/product/aldrich/181986?context=product, (last accessed on August 08, 2021).

[2] https://carverpress.com/news/68-carver-auto-series-presses, (last accessed on April 18, 2022).

[3] N. N. Getangama. *Dielectric Spectroscopy of Polyvinyl alcohol Hydrogels and Nanocomposites*. MSc thesis, The University of Western Ontario, London, Ontario, Canada, 2015.

[4] *Materials Test System User Guide*. Solartron Analytical Ltd., 2011.

[5] http://www.lakeshore.com/products/cryogenic-temperature-controllers/model-335/pages/overview.aspx, (last accessed on August 03, 2015).

[6] C. W. Macosko. *Rheology Principles, Measurements, and Applications*. Willey-VCH, Inc, 1994.

Chapter 4

Dielectric properties of PEO/MWCNT nanocomposites

4.1   Introduction

Polymer nanocomposites are a novel class of composite material made by adding nanometer-sized filler particles to a polymer matrix. Carbon-nanotube-based nanocomposites have been of great interest both fundamentally and to the materials industry due to their exceptional electrical and mechanical properties [1, 2, 3]. As examples, the electrical conductivity of an insulating polymer can be increased by many orders of magnitude by adding only a small amount of carbon nanotubes (CNT) [3, 4], while their very high Young's modulus and mechanical strength make carbon nanotubes an attractive filler for improving the mechanical properties of polymer-based materials [5]. Because of these attractive electrical and mechanical properties, polymer nanocomposite materials have potential applications in many areas, including electrostatic coatings [6], conducting plastics, energy storage, conductive adhesives, light-emitting and photonic devices, and air and water filtration [7].

In the present work, we use dielectric spectroscopy to study the microscopic interactions between CNTs and molecules of poly(ethylene oxide) (PEO, $[CH_2CH_2O]_n$) and their effect on

the bulk electrical properties of PEO-CNT nanocomposites. Because PEO is a biocompatible polymer, nanocomposites based on PEO are of substantial interest for biomedical applications such as controlled drug release [8, 9].

The electrical properties of polymer nanocomposites have been studied extensively [3, 10]. As conductive nanoscale fillers are added to an insulating polymer matrix, the material's electrical conductivity increases dramatically when the filler concentration p exceeds a percolation threshold p_c [4]. This percolation transition occurs when the filler particles form a three-dimensional conductive network that spans the material sample [11]. For CNTs, which have a very high length-to-diameter aspect ratio, electrical percolation occurs at a nanotube concentration that can be much less than 1% [6]. p_c is quite sensitive to the degree of dispersion and alignment of the CNTs, however, with stronger alignment or uneven dispersion leading to fewer electrical contacts between tubes and a higher percolation threshold than for randomly oriented tubes [12].

Above (but close to) the percolation transition, the dc conductivity σ_{dc} is predicted to behave as a power law in $p - p_c$, *i.e.,* [10, 11, 13]

$$\sigma_{dc} = A \left(p - p_c \right)^t, \tag{4.1}$$

where A is an amplitude factor and the critical exponent t has a theoretical value of approximately 2 for a simple cubic three-dimensional network [14]. This behaviour has been observed in many polymer nanocomposite systems [3, 10]. Potschke *et al.* [4] studied polycarbonate-MWCNT nanocomposites prepared by melt mixing. They found the percolation threshold p_c to be between 1.0 and 1.5 wt% and the critical exponent t to be 2.1. McCullen *et al.* [15] studied the electrical conductivity of mats of PEO/MWCNT nanofibers made by electrospinning. They observed an increase in conductivity by a factor of 10^{12} at the percolation transition, and found $t = 1.3 \pm 0.6$. Critical exponents significantly higher than 2 have also been observed [16, 17, 18], and have been attributed in part to clustering of the filler particles [16, 17].

Dielectric spectroscopy involves the study of a material's complex permittivity $\epsilon^* = \epsilon' - i\epsilon''$ over a broad range of frequencies. Here ϵ' is the dielectric coefficient divided by ϵ_0, the permittivity of free space, and6 $\epsilon'' = \sigma/\epsilon_0\omega$, where σ is the frequency-dependent electrical conductivity and ω is the angular frequency. This technique has been widely used to probe polymer dynamics, molecular configurations and charge transport in polymeric materials [4, 19, 20, 21, 22]. The dielectric properties of a material are sensitive to the configuration of microscopic electric dipoles. The material's dielectric response to a time-varying electric field thus provides information about molecular dynamics and configurational relaxation processes within the material.

Ideally, the spectrum of ϵ'', the imaginary part of the dielectric response, will display one or more peaks corresponding to distinct dielectric relaxation processes. A peak at angular frequency ω_m corresponds to a relaxation process with a characteristic relaxation time τ given by

$$\tau = \frac{1}{\omega_m}. \tag{4.2}$$

In reality, the dielectric spectra of polymeric materials are complicated and display very broad relaxation features. A variety of dielectric relaxation models have been used in their interpretation [23, 24, 25, 26]. In this work, we determine the dielectric properties of our nanocomposites by fitting the well-known empirical Havriliak-Negami (HN) model [21] to the imaginary part of our experimentally measured spectra. In this model, which has been applied to polymeric materials by several groups [21, 27, 28], the complex permittivity $\epsilon^* = \epsilon' - i\epsilon''$ is given by

$$\epsilon^* = \epsilon_\infty + \frac{\Delta\epsilon_1}{(1 + (i\omega\tau_1)^{\alpha_1})^{\beta_1}} + \frac{\Delta\epsilon_2}{(1 + (i\omega\tau_2)^{\alpha_2})^{\beta_2}} + \frac{\sigma_{dc}}{i\omega\epsilon_0} \tag{4.3}$$

where $\Delta\epsilon_1$ and $\Delta\epsilon_2$ are dielectric strengths and τ_1 and τ_2 are relaxation times. The four terms on the right-hand side of Eq. (4.3) represent contributions to ϵ^* due to the constant infinite-frequency dielectric constant ϵ_∞, two relaxation processes, and the dc conductivity σ_{dc}.

When the exponents α_1, α_2, β_1 and β_2 in Eq. (4.3) are all equal to 1, the two relaxation

terms describe exponential relaxation processes with relaxation times τ_1 and τ_2, respectively. For non-exponential relaxation processes, τ_1 and τ_2 can be regarded as characteristic relaxation times. Each relaxation process is manifested as a peak in ϵ''. The α parameters control the slopes of the sides of the peaks and thus their width. The β parameters affect the slopes of the high-frequency side of the peaks, thus varying the skewness.

In this paper, we study the dielectric spectra and dc conductivity of PEO-CNT nanocomposites made by both melt mixing and twin-screw extrusion, as functions of CNT loading and temperature. The HN model is used to extract the dielectric parameters from the experimentally measured spectra. Our results are discussed in terms of the microstructure of the nanocomposites and the microscopic interactions between the nanotubes and the polymer molecules.

4.2   Experiment

We prepared nanocomposites of PEO and multi-walled carbon nanotubes (MWCNT) using two different methods — melt mixing and twin-screw compounding — to disperse the nanotubes in the polymer matrix. In both cases, the starting materials were the same. PEO powder with molar mass of 100,000 g/mol was purchased from Sigma-Aldrich and used without further purification. MWCNT with diameter 8–15 nm and length 30–50 μm was purchased from TimeNano Chengdu Organic Chemicals and used as received. We used MWCNT concentrations ranging from 0 to 5% by weight.

To prepare melt-mixed samples, 50 g of PEO powder and the required amount of MWCNT were added to a Brabender three-piece mixer equipped with two counter-rotating blades and preheated to 75 °C. The material was mixed for 10 minutes, then removed from the mixer and cooled to room temperature. The resulting material was pelletized to obtain particles of a suitable size for the compression molding process described below.

In the second method, 4.5 g of PEO and the required amount of MWCNT were mixed in a Thermo Scientific HAAKE MiniLab II twin-screw micro-compounder preheated to 75 °C.

The components were mixed for 10 minutes with a screw speed of 50 rpm before extracting the compound from the mixer and cooling to room temperature. The extracted material was in the form of a long sheet, about 5 mm in width and 1 mm thick, which was pulverized prior to compression molding.

Disks of the nanocomposites 25 mm in diameter and 1 mm thick were made by transferring the small pieces of PEO/MWCNT prepared as above to a room temperature mold made from 3.2 mm thick aluminum plates, separated by a 1 mm thick aluminum gasket with three 25 mm diameter holes in it. The filled mold was heated to 75 °C for 5 min, then compressed under 13.3 kN of force for 5 min. Finally, the mold was cooled to room temperature and the disks removed.

We use the following notation to identify our samples: the nanocomposites prepared by melt-mixing are labeled by an M followed by the amount of MWCNT added, given as a percentage of the total sample weight, while those prepared by twin-screw extrusion are labeled by T followed by the wt% MWCNT. Thus, for example, M1.5 refers to a melt-mixed sample containing 1.5 wt% MWCNT. Samples of pure PEO, made in the melt mixer only, are referred to as M0.0.

Scanning electron microscope (SEM) images of the nanocomposite samples were obtained using a high-resolution Zeiss 1540XB SEM with an acceleration voltage of 1.0 keV. The composites were quenched in liquid nitrogen and fractured. The newly-exposed cross-section was then coated with a conducting layer of osmium for imaging with the SEM.

The complex permittivity $\epsilon^* = \epsilon' - i\epsilon''$ of the nanocomposites was measured as a function of frequency and temperature T using a Solartron ModuLab Material Test System (MTS) dielectric spectrometer with a Janis Research STVP-200-XG cryostat for temperature variation. The 25 mm diameter PEO nanocomposite disks were placed between the 25 mm diameter electrodes of the dielectric spectrometer's solid-sample holder. A sinusoidal voltage at frequency $f = \omega/2\pi$ was applied across the sample holder, and the amplitude and phase of the resulting current were measured. Our measurements were conducted using a 2-wire measurement tech-

nique over the frequency range 0.1 Hz $\leq f \leq$ 1 MHz, using a sinusoidal excitation voltage of 4 V rms. A Lake Shore Model 335 Cryogenic Temperature Controller was used to control the temperature T of the sample with an accuracy of 0.01 K. Measurements were taken at temperatures from 180 K to 300 K, and samples were allowed to equilibrate at each temperature for 20 minutes before the dielectric spectrum was measured.

The DC conductivity σ_{dc} of the samples was also measured using the MTS. A DC voltage V_{dc} was applied across the sample and the DC current density $J_{dc} = I_{dc}/A$, where A is the cross-sectional area of the sample, was measured. At low applied voltages, the samples are Ohmic, with $J_{dc} \propto V_{dc}$. Knowing the sample thickness ℓ, σ_{dc} is then simply given by

$$\sigma_{dc} = \frac{\ell}{A} \frac{dI_{dc}}{dV_{dc}}. \tag{4.4}$$

4.3   Results

4.3.1   Distribution of CNTs

Fig. 4.1 shows SEM images of nanocomposite samples prepared by melt-mixing and twin-screw extrusion. All images show a portion of a cross-sectional surface of the nanocomposite obtained by freeze-fracture as described above. Samples M0.5 and M3.5 are shown in Fig. 4.1(a) and (b), respectively. In Fig. 4.1(a) the nanotube concentration is quite low, and is, as will be shown below, less than the critical concentration at which a percolation transition occurs. Individual nanotubes and small clusters can be seen throughout the image, and clusters with an extent (in the image plane) on the order of a few μm are visible near the center of the image. While the distribution of nanotubes is far from homogeneous on the 1 μm scale, it appears to be more uniform when averaged over regions the size of this image or larger. The clusters seen in the M3.5 sample shown in Fig. 4.1(b) are much larger and, indeed, extend right across the image. As will be discussed, the nanotube concentration in this sample is well above that at the percolation transition.
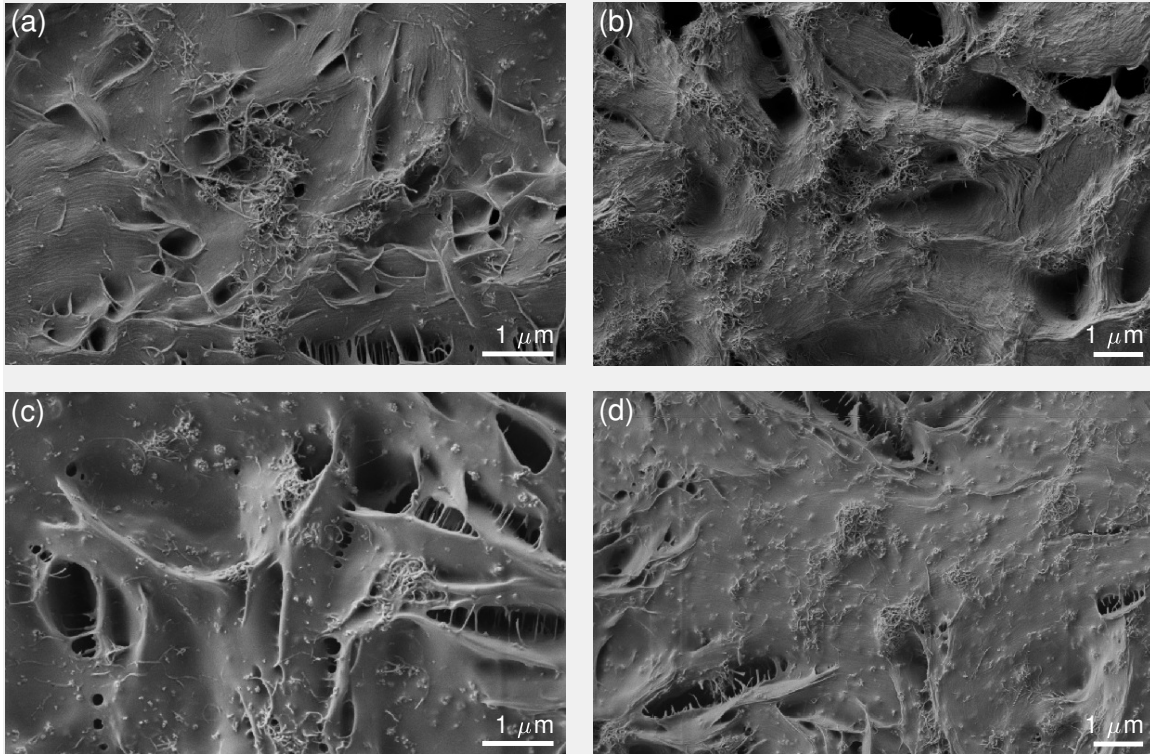
Figure 4.1: SEM images of PEO-MWCNT nanocomposites (a) M0.5, (b) M3.5, (c) T0.5, and (d) T2.0. In (a) and (c), the MWCNT concentration is below the percolation transition described in the text, while in (b) and (d) it is above the transition. These images are discussed in more detail in the text.

Fig. 4.1(c) and (d) show SEM images of samples T0.5 and T2.0. Again the nanotube concentration in Fig. 4.1(c) is quite low, and is less than the critical percolation concentration for this material. Small clusters of nanotubes on the order of 1 μm in scale can be seen, and appear to be distributed more uniformly than in the corresponding melt-mixed sample M0.5 shown in Fig. 4.1(a). Similar clusters are seen in sample T2.0, shown in Fig. 4.1(d), although the clusters are slightly larger than in Fig. 4.1(a) and are more broadly and uniformly distributed across the image.

4.3.2 Overall dielectric response

The effect of CNT loading on the dielectric response of PEO-MWCNT nanocomposites is illustrated in Fig. 4.2. This figure shows the real and imaginary parts of the complex permittivity at
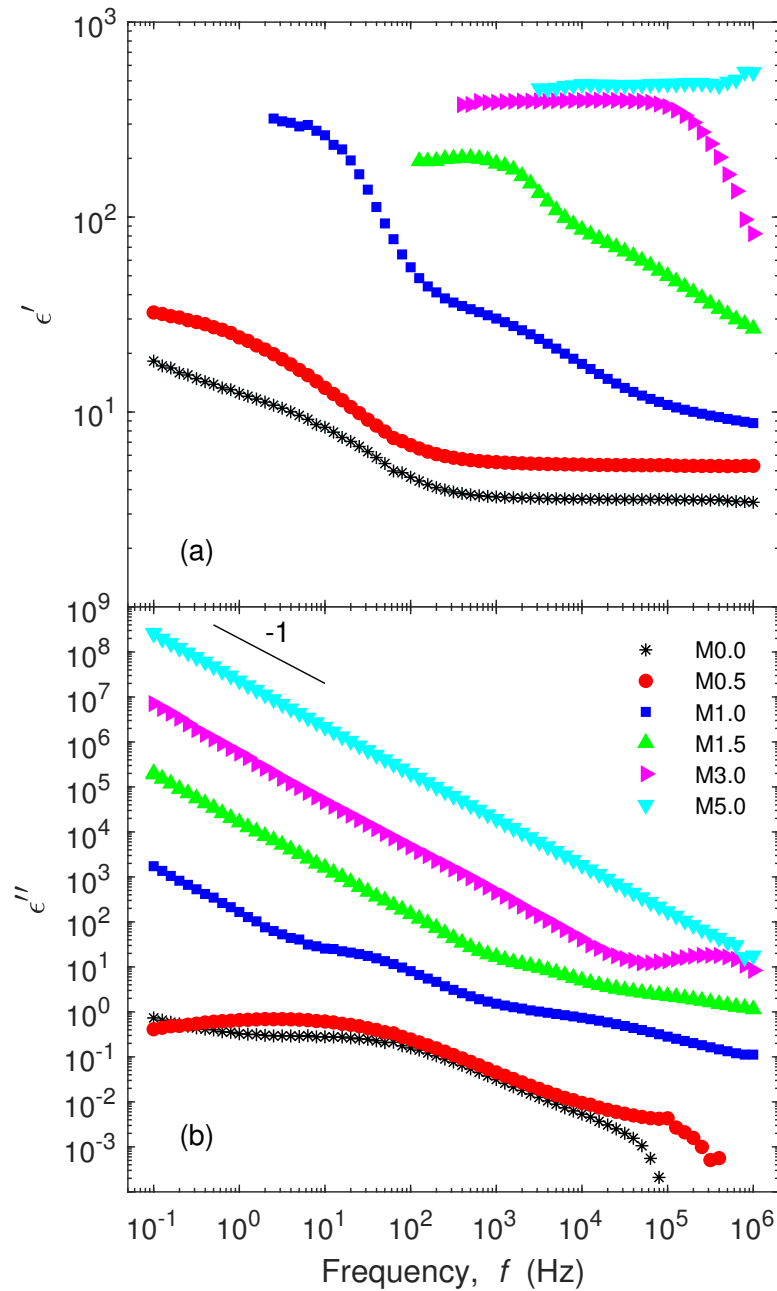
Figure 4.2: (a) Real (ϵ') and (b) imaginary (ϵ'') parts of the permittivity of melt-mixed PEO/MWCNT nanocomposites at a temperature of 280 K. The different symbols represent different MWCNT concentrations. The solid line in (b) has a logarithmic slope of -1 and is shown for comparison.

$T = 280$ K for a series of melt-mixed PEO/MWCNT nanocomposites with MWCNT concentrations ranging from 0 (i.e., pure PEO) to 5 wt%. The pure polymer has a dielectric constant that is independent of frequency above 1 kHz, but ϵ' increases with decreasing frequency be-

low 1 kHz. The imaginary part ϵ'' has a weak frequency dependence and shows a broad peak at around 100 Hz. Both the low-frequency increase in ϵ' and the broad peak in ϵ'' indicate the presence of a dielectric relaxation process with a characteristic relaxation time on the order of 10 ms. Adding 0.5 wt% MWCNT to the polymer decreases the frequency of the relaxation feature, but does not qualitatively change the dielectric response. When the MWCNT concentration is increased to 1.0 wt% or higher, however, both ϵ' and ϵ'' increase significantly and higher-frequency relaxation features become visible in the dielectric spectra. At the highest concentrations studied, ϵ' could not be accurately measured at low frequencies due to the very high conductivity of the materials (see below) [4]. At $p = 5.0$ wt% (sample M5.0), ϵ' at 280 K is approximately 150 times higher than that for pure PEO over the kHz-to-MHz frequency range.

The changes in the imaginary part of the dielectric response are more dramatic, as seen in Fig. 4.2(b). ϵ'' behaves as $1/f$ at low frequencies, indicating that the electrical conductivity $\sigma = \omega\epsilon_0\epsilon''$ is constant in that frequency range. The low-frequency value of ϵ'' increases by a factor of 1000 as p is increased from 0.5 to 1.0 wt%, and by 8 orders of magnitude between $p = 0.5$ wt% and 5.0 wt%. This large increase is due to the high conductivity of the nanotubes, which form a percolation network above some critical concentration. As a result, the electrical conductivity σ of the nanocomposite is much higher than that of the pure polymer matrix and independent of f at low frequencies. The dielectric relaxation feature seen around 100 Hz at low p is no longer visible for $p > 1.5$ wt%, possibly masked by the conductive response of the nanotubes.

Fig. 4.3 shows the complex permittivity at $T = 280$ K for a series of PEO nanocomposites prepared by twin-screw extrusion. The behaviour of these data are qualitatively similar to that of the melt-mixed samples displayed in Fig. 4.2. The data for the low-p samples again show a broad relaxation feature around 100 Hz, a dramatic increase in both ϵ' and ϵ'' as the CNT concentration is increased, and a $1/f$ dependence of ϵ'' at low frequencies. On the other hand, there is a larger difference in ϵ' between the pure PEO and T0.5 than between M0.0 and M0.5,
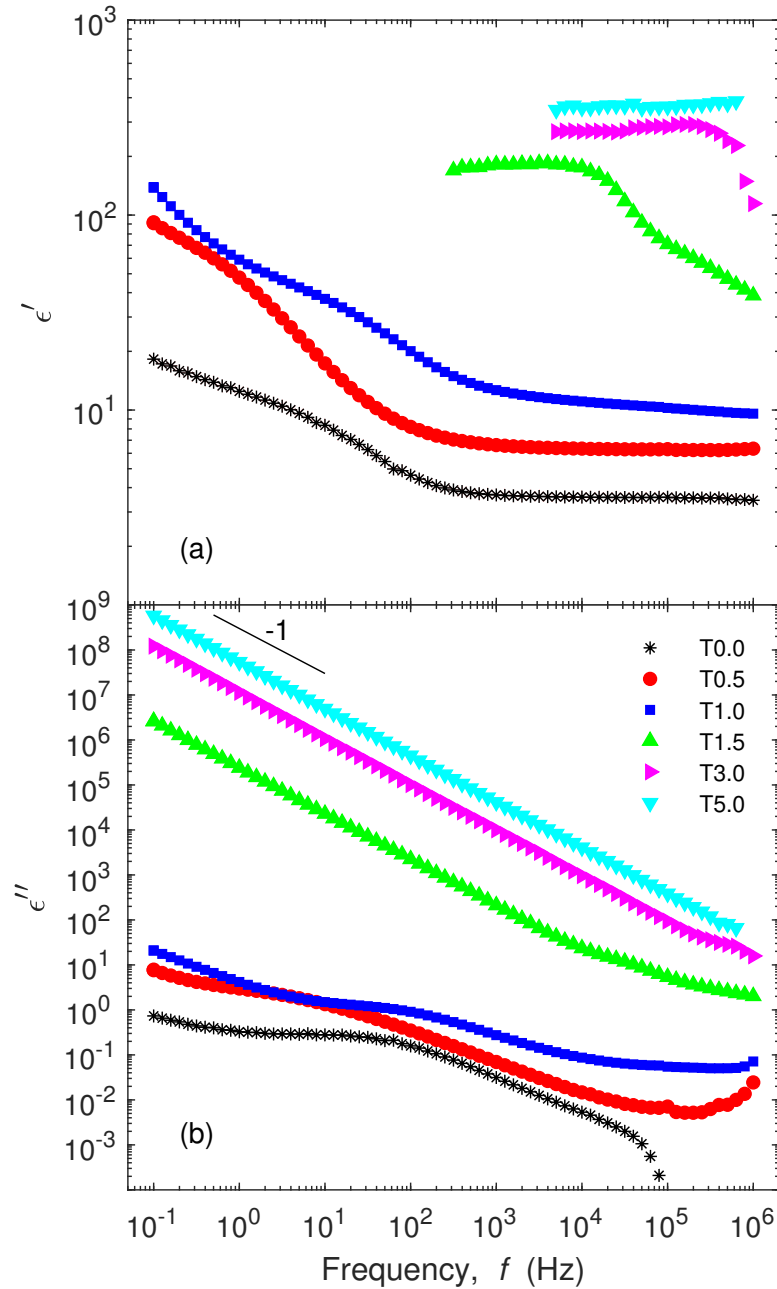
Figure 4.3: (a) Real (ϵ') and (b) imaginary (ϵ'') parts of the permittivity of twin-screw-extruded PEO/MWCNT nanocomposites at temperature $T = 280$ K. The different symbols represent different MWCNT concentrations. The solid line in (b) has a logarithmic slope of -1 and is shown for comparison.

especially at low frequencies, and the dramatic increase in ϵ' and ϵ'' occurs at a slightly higher nanotube concentration for the T samples (between $p = 1.0$ and 1.5 wt%) than for the M samples (between $p = 0.5$ and 1.0 wt%). The frequency dependence of the dielectric spectra

and the percolation transition will be analysed more quantitatively below.
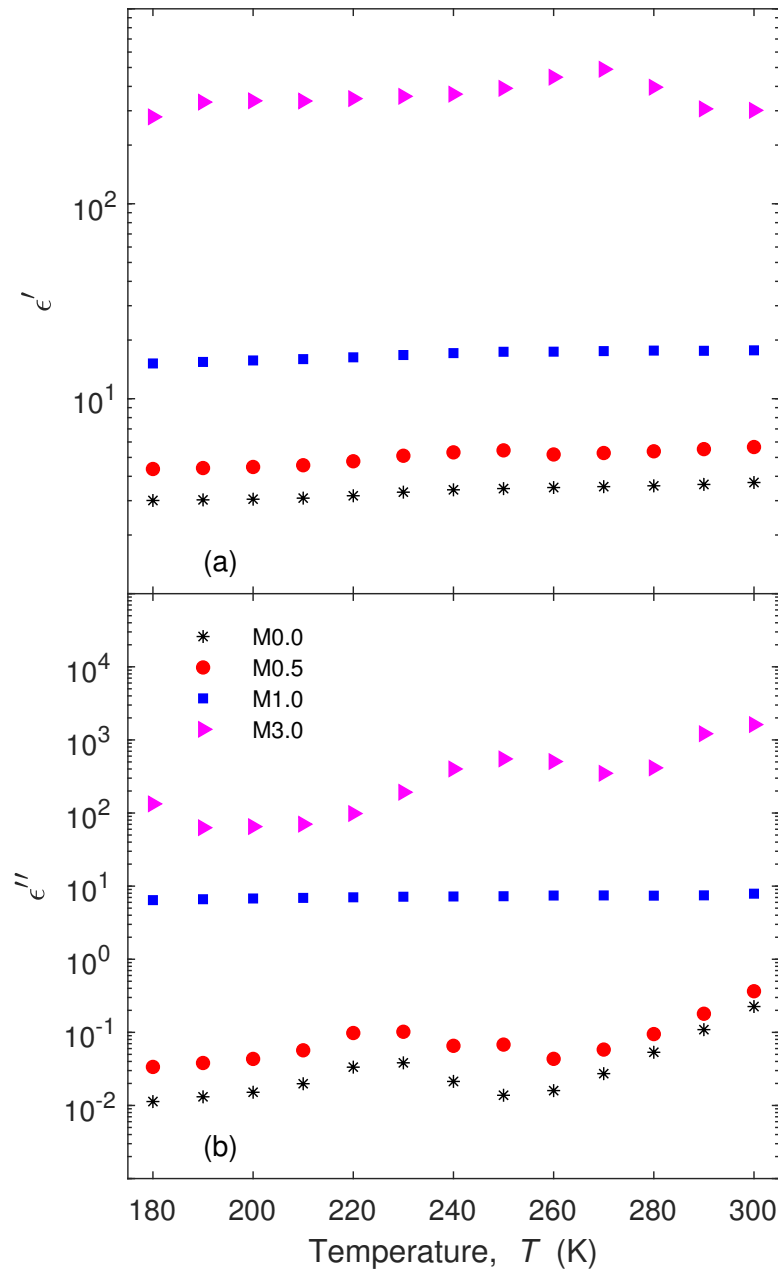
Figure 4.4: (a) Real (ϵ') and (b) imaginary (ϵ'') parts of the permittivity of melt-mixed PEO nanocomposites at f = 1 kHz as a function of T. The different symbols represent different MWCNT concentrations. The corresponding data for twin-screw extruded samples are shown in Appendix A.

ϵ' and ϵ'' at a frequency of 1 kHz are plotted as a function of temperature for melt-mixed samples at four representative MWCNT concentrations in Fig. 4.4. Data for the T samples are shown in Appendix A. ϵ' is essentially independent of temperature over the range of our

experiments, while ϵ'' increases with increasing T. Consistent with what was seen above, the dielectric response of M0.5 is very close to that of the pure PEO, while both ϵ' and ϵ'' increase substantially for $p \gtrsim 1.0$ wt%.
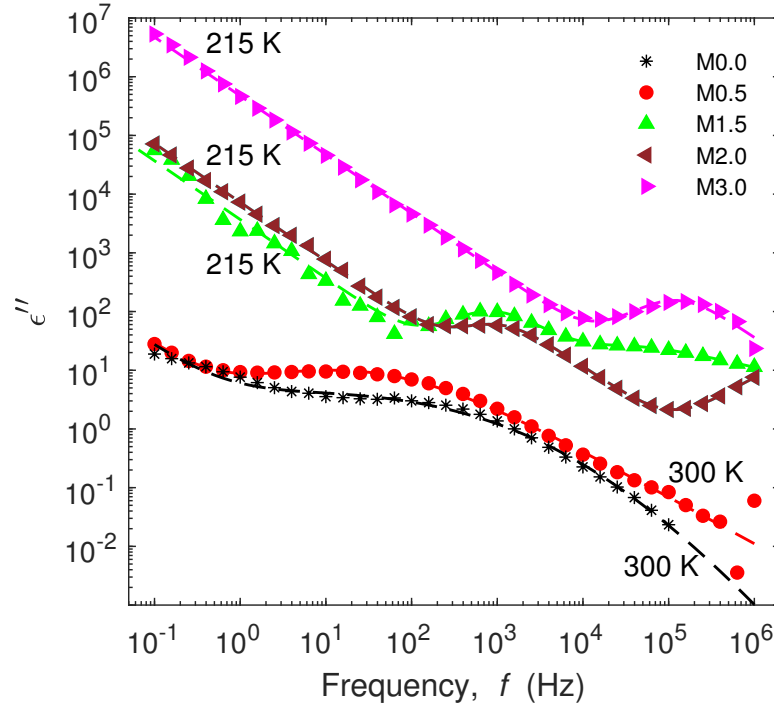
Figure 4.5: Fits of the HN model, Eq. (4.3), to ϵ'' for melt-mixed PEO nanocomposites at a few different temperatures and MWCNT concentrations, illustrating the range of behavior observed. The symbols represent the experimental data and the dashed lines are the fits. One relaxation term was used for samples M0.0, M0.5 and M3.0, and two were used for M1.5 and M2.0. Representative fits for twin-screw extruded samples are shown in Appendix A.

A more quantitative analysis of the dielectric spectra of the nanocomposites was performed by fitting the imaginary part of the permittivity to the HN model, Eq. (4.3). Fig. 4.5 shows fits to $\epsilon''(f)$ for several melt-mixed samples, representing the range of behaviour observed. Since the shape of the spectrum depends strongly on both p and T, we choose either one or two relaxation terms in the HN model based on the number of peaks evident in the ϵ'' data. In general, good fits were obtained using a single relaxation term at low and high MWCNT loadings, while two relaxation terms gave better fits at some intermediate nanotube concentrations (specifically, samples M1.5, M2.0, T0.5 and T1.5). The parameters obtained from fits to the data for samples M2.0 and T2.0 at several different temperatures are presented in Appendix A. In this case of

sample M2.0, while two relaxation terms were used in the fit, the fitted location of the higher-frequency relaxation peak was outside of our experimental range, as can be seen in Fig. 4.5. We therefore include only the parameters that correspond to the lower-frequency relaxation term in the table presented in Appendix A. For sample T2.0, on the other hand, a single relaxation term was sufficient to fit the data. Results derived from fits such as these are discussed below.

4.3.3 dc conductivity
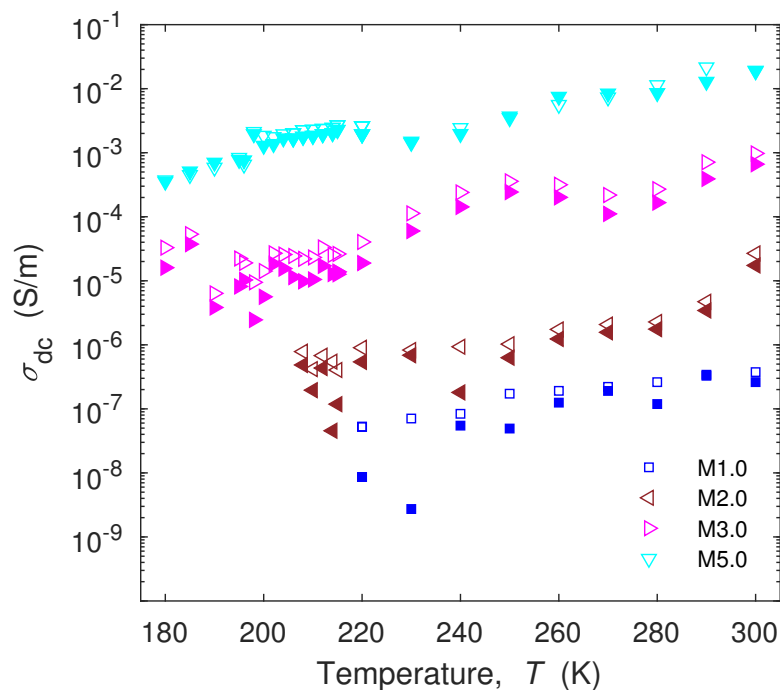
Figure 4.6: DC conductivity obtained from fits to Eq. (4.3) (open symbols) and direct dc measurements (solid symbols) as a function of temperature for melt-mixed nanocomposites. Different symbols represent different MWCNT concentrations. The uncertainty in σ_{dc} is indicated by the scatter in the data. Data for the twin-screw extruded samples are shown in Appendix A.

The last term on the right-hand side of Eq. (4.3) represents the contribution to the permittivity due to the dc conductivity of the material, σ_{dc}. This contribution is responsible for the low-frequency $1/f$ behavior of ϵ'' seen in Figs. 4.2, 4.3, and 4.5. Fig. 4.6 shows σ_{dc} as a function of T for the melt-mixed samples. The open symbols are values obtained from the fits to Eq. (4.3), as described above. The solid symbols are conductivities that were measured directly

in dc experiments.

The results obtained from the two methods agree very well. The conductivity of pure PEO and M0.5 (not shown in Fig. 4.6 as the data are very noisy) was about 10^{-10} S/m at 300 K and decreased slightly with decreasing temperature. σ_{dc} increases by more than three orders of magnitude as p is increased from 0.5 to 1.0 wt%. As the concentration of nanotubes is increased further, the conductivity of the nanocomposites continues to increase, and at $p = 5.0$ wt%, σ_{dc} is eight orders of magnitude larger than for pure PEO. The behavior of the dc conductivity of the twin-screw extruded samples is qualitatively similar, as shown in Appendix A.
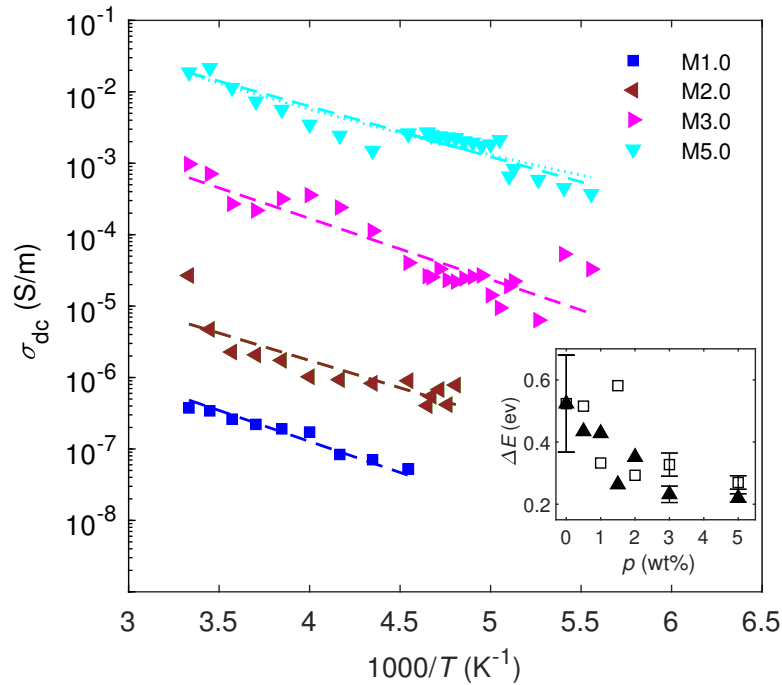
Figure 4.7: σ_{dc} plotted as a function of $1/T$ for different melt-mixed nanocomposites as indicated in the legend. The dashed lines are fits to Eq. (4.5) and the dotted line (shown only for M5.0) is a fit to Eq. (4.6). The uncertainty in σ_{dc} is indicated by the scatter in the data. Corresponding data for twin-screw extruded samples are shown in Appendix A. The inset shows the activation energy ΔE determined from fits to Eq. (4.5) for both M (open symbols) and T (solid symbols) nanocomposites as a function of MWCNT concentration p.

Fig. 4.7 shows the dc conductivity obtained from fits to Eq. (4.3) as a function of the reciprocal of the temperature, $1/T$. Also shown in this figure are fits of the data to the theoretical expressions for two possible models for the temperature dependence of the conductivity. The

dashed lines in Fig. 4.7 correspond to a thermally activated (Arrhenius law) conductivity,

$$\sigma_{dc} = \sigma_0 e^{-\Delta E/2k_B T}, \tag{4.5}$$

where k_B is the Boltzmann constant, σ_0 is the conductivity at infinite temperature, and ΔE is the activation energy [29]. The dotted line (shown only for sample M5.0), is a fit to the theoretical expression for three-dimensional variable-range hopping,

$$\sigma_{dc} = \sigma_0 e^{-(T_0/T)^{1/4}}, \tag{4.6}$$

where T_0 is a characteristic temperature [30, 31]. The two fits are almost indistinguishable over our experimental temperature range; for this reason, the fit to Eq. (4.6) is only shown for one value of p. More sophisticated models of the conductivity are certainly possible, but are not warranted by the precision and limited temperature range of our data.

Both theoretical models describe the conductivity of our nanocomposites within our experimental scatter. The characteristic temperatures extracted from our fits to Eq. (4.6), however, are on the order of 10^8 K, which seem too high to be physical. On the other hand, the thermally-activated conductivity model, Eq. (4.5), yields values of ΔE of a few tenths of an eV, which is physically very reasonable. We thus believe that Eq. (4.5) provides the more meaningful description of our dc conductivity data. The inset in Fig. 4.7 shows the activation energy obtained by fitting the dc conductivity data to this model. ΔE is the same within our experimental scatter for both melt-mixed and extruded nanocomposites. The activation energy was 0.52 ± 0.11 eV for pure PEO and decreases as the MWCNT concentration is increased for both sample types. Therefore we hypothesize that the conducting network consists of highly conductive nanotubes separated by thin polymer domains, with electron transfer between nanotubes being thermally activated.

4.3.4 Percolation transition

The values of σ_{dc} obtained from the fits to Eq. (4.3) are plotted as a function of nanotube concentration p at T = 300 K for both M and T samples in Fig. 4.8. The initial low conductivity of the pure polymer increases dramatically when p is increased above a threshold value p_c; this indicates the formation of a conductive percolation network that spans the polymer matrix at $p = p_c$ [4].
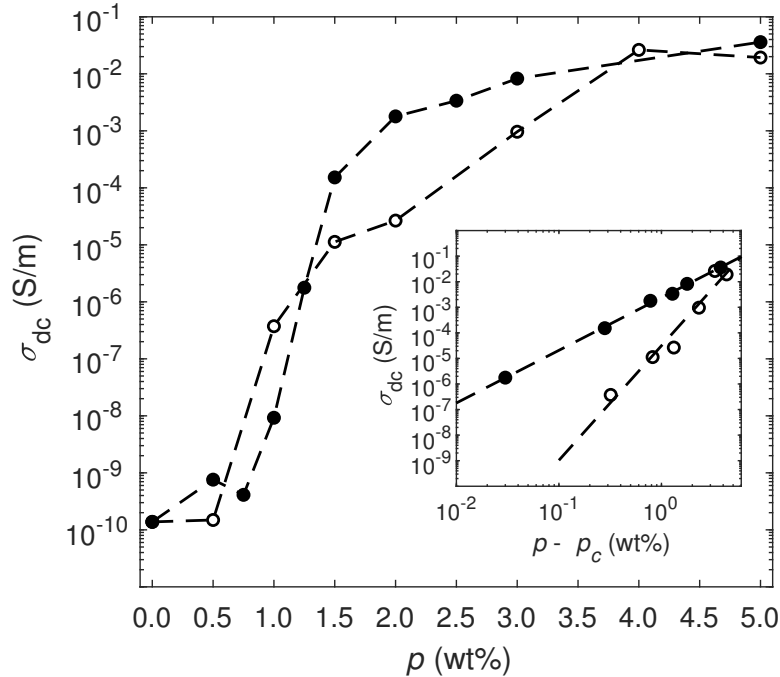
Figure 4.8: DC conductivity of the PEO/MWCNT nanocomposites as a function of MWCNT concentration p at 300 K. Open and solid symbols represent melt-mixed and twin-screw extruded samples, respectively. The dashed lines in the main figure are guides to the eye and the error bars of the individual data points are roughly the size of the symbols, while the scatter of the conductivity curves is more likely due to variations in the internal structure of the samples resulting from their preparation.
  The inset shows σ_{dc} vs $p - p_c$ for $p > p_c$. Here the lines are fits to the power law, Eq. (4.1).

Based on the behavior of σ_{dc} seen in Fig. 4.8, we analysed the data for the twin-screw samples by varying p_c from 0.76 to 1.24 wt% in steps of 0.01 wt% and performing a fit of the logarithm of the data to Eq. (4.1) with A and t being fit parameters. The values of the χ^2 parameter for the fit and the exponent t for each trial value of p_c are plotted in Fig. 4.9(a). It is clear from the figure that the fitted value of t is very strongly correlated with the value used for
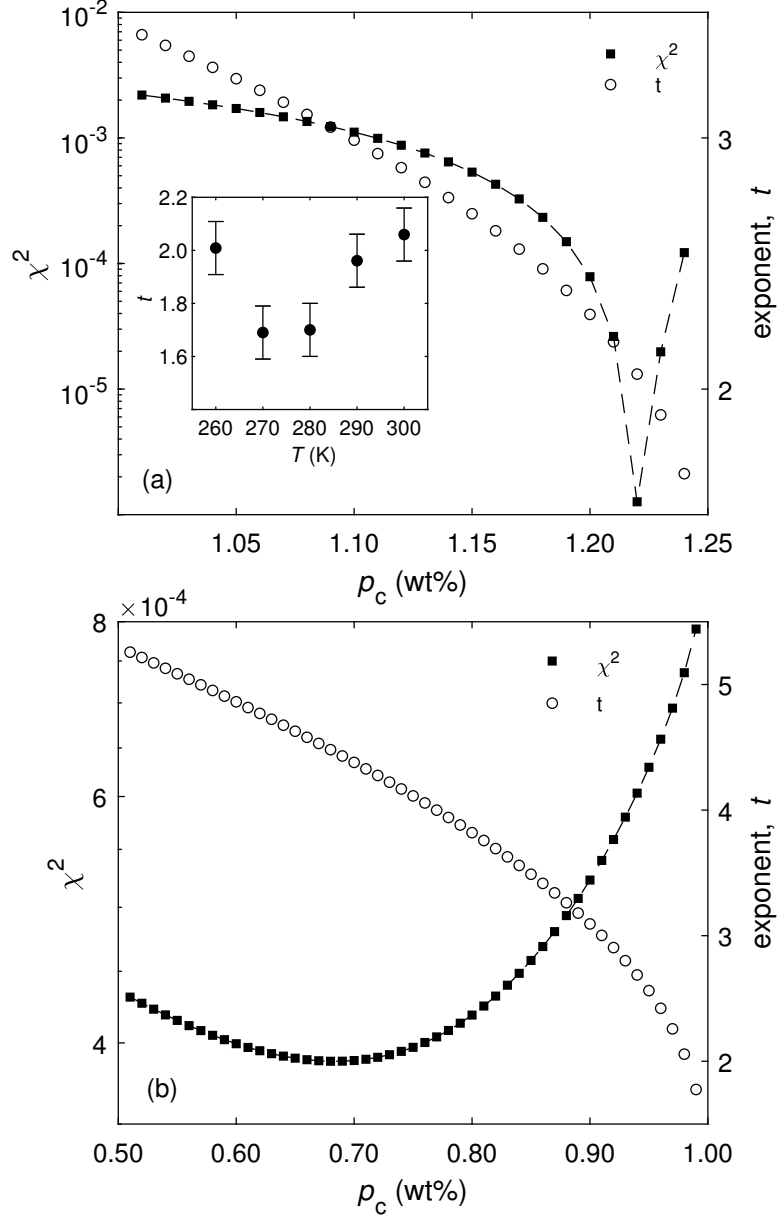
Figure 4.9: χ^2 (left axis) and the percolation exponent t (right axis) determined from fits of Eq. (4.1) to data for σ_{dc} plotted for a range of trial values of the percolation concentration p_c. (a) is for the T samples and (b) for the M samples. The dashed line through the χ^2 data is to guide the eye. The inset in (a) shows the optimum value of t found as a function of temperature T.

p_c, implying that accurate data and measurements at concentrations quite close to (but above) p_c are required to extract accurate values of both the critical concentration and the exponent. In this case, χ^2 has an extremely well-defined minimum at $p_c = 1.22 \pm 0.005$, at which the critical exponent $t = 2.1 \pm 0.1$, in excellent agreement with the predicted value for a simple cubic 3-

dimensional lattice [14]. This power-law fit is shown in the inset of Fig. 4.8 and describes the data very well. Data for all temperatures studied from 260 to 300 K were analyzed in the same way, and the resulting values of t are plotted as a function of temperature in the inset to Fig. 4.9(a). No systematic dependence on temperature is observed, all values of t are reasonably consistent with the theoretical value of 2, and its mean value is $t = 1.9 \pm 0.2$. Similarly, the percolation threshold shows no systematic dependence on T and has a mean of 1.23 ± 0.01 wt% (data not shown).

The same analysis was carried out for the conductivity data obtained with the melt-mixed samples. In this case, p_c was varied from 0.51 to 0.99 wt%. The resulting values of χ^2 and t for $T = 300$ K are plotted in Fig. 4.9(b). In this case, χ^2 is a minimum for $p_c = 0.68$ wt%, corresponding to $t = 4.5$. Here, the minimum in χ^2 is much broader than was the case for the extruded samples, however, and as a consequence both the critical concentration and the power-law exponent are much more uncertain. Since our fit has two parameters, the 68% confidence interval is that over which χ^2 increases by a factor of 2.3 [32]. It is clear from Fig. 4.9(b) that p_c and t are thus very poorly defined; a reasonable estimate for t in this case would be $t = 5 \pm 5$. Once again, the resulting power law fit is plotted in the inset of Fig. 4.8, although the large uncertainties must be kept in mind in this case. The results at other temperatures are similar, and, despite the large uncertainties from the individual fits, the values of the parameters were fairly consistent over the range of temperatures studied: the mean value of p for the melt-mixed samples was 0.65 ± 0.05 wt%, and the mean value of t was 4.7 with a standard deviation of 0.2.

4.3.5 Dielectric relaxation times

The second and third terms in Eq. (4.3) describe contributions to ϵ'' due to dielectric relaxation processes. As noted above, many of our dielectric spectra could be fitted well with a single relaxation term, while others required two. In the latter case, we take $\tau_1 > \tau_2$, i.e., τ_1 is the relaxation time of the slower of the two processes. In some cases, as, for example, the data for M1.5 at 215 K shown in Fig. 4.5, two relaxation peaks are clearly visible in the ϵ'' spectrum. In

other cases, however, although the τ_2 term was required to get a good fit to the data, the actual relaxation peak was well above our experimental frequency range. Occasionally, notwithstanding the fit results, there was no visible feature in ϵ'' corresponding to a relaxation process at τ_2. In these latter two situations, the existence of a well-defined faster relaxation process is questionable, and as a result the corresponding relaxation times are not discussed further.
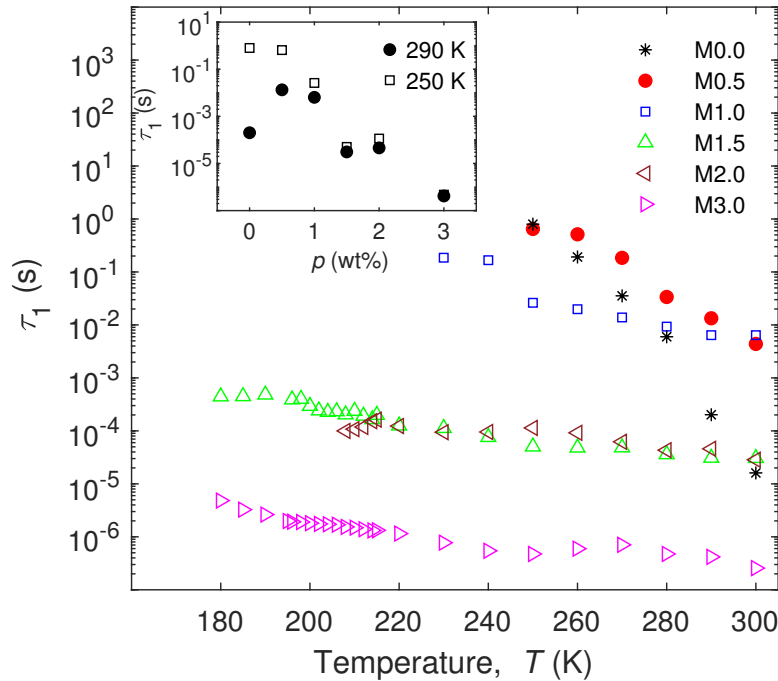
Figure 4.10: The dielectric relaxation time τ_1 of the melt-mixed nanocomposites plotted as a function of temperature. The different symbols represent different MWCNT concentrations, as indicated in the legend. Corresponding data for the twin-screw extruded samples are shown in Appendix A. The inset shows τ_1 at 250 and 290 K as a function of MWCNT concentration p.

The variation of the dielectric relaxation time τ_1 with temperature T and nanotube concentration p is shown for the melt-mixed samples in Fig. 4.10. Similar behavior is seen for the T samples as shown in Appendix A.

The single relaxation time for the pure polymer (M0.0) is on the order of 10^{-5} s at 300 K and increases rapidly to 10^0 s as T is decreased to 260 K. This may be a manifestation of the glass transition of PEO, which has been observed at $T = 205$ K [33]. Addition of nanotubes at concentrations below the percolation threshold increases the relaxation time at $T = 300$ K, but weakens its temperature dependence. For $p \leq 1$ wt%, $\tau_1 \approx 10^{-2}$ s at $T = 300$ K and increases

by roughly two orders of magnitude as T is decreased to 240 K. At lower temperatures, the data become noisy and the relaxation peaks cannot be distinguished.

For nanotube concentrations $p \geq 1.5$ wt%, we observe shorter relaxation times — always less than 10^{-3} s — with a considerably weaker temperature dependence. The inset to Fig. 4.10 shows the dependence of τ_1 on p at two temperatures. At $T = 290$ K, the relaxation time initially increases on addition of nanotubes to the polymer matrix, then decreases as p is further increased. At 250 K, on the other hand, τ_1 decreases monotonically as p is increased.

The width parameter α_1 that appears in Eq. (4.3) is physically constrained to the range $0 \leq \alpha_1 \leq 1$, with $\alpha_1 = 1$ corresponding to a dielectric relaxation process with a single relaxation time and $\alpha_1 < 1$ indicating a distribution of relaxation times. The product $\alpha_1 \beta_1$ is also constrained, with $\alpha_1 \beta_1 \leq 1$ [22]. The behavior of these parameters as determined from our data changes as the nanotube concentration is varied. For melt-mixed nanocomposites with MWCNT concentrations higher than 1 wt%, good fits to Eq. (4.3) were obtained with both α_1 and β_1 fixed at 1. If α_1 and β_1 were treated as unconstrained free parameters, however, the fitting routine gave both α_1 and β_1 higher than 1 at some temperatures, although with no significant improvement in the quality of the fit. For the M1.0 sample, the fits gave $\alpha_1 = 1$ and $\beta_1 \approx 0.4$ for all temperatures between 230 and 300 K.

For lower MWCNT concentrations, fits to Eq. (4.3) with α_1 and β_1 unconstrained free parameters gave $\alpha = 0.3$, $\beta_1 = 7$ and $\alpha_1 = 0.5$, $\beta_1 = 2$ at $T = 300$ K for samples M0.0 and M0.5 respectively. As T was decreased, α_1 increased monotonically to about 2, while β_1 decreased to 0.2. In some cases, these results violate the constraints mentioned above. On the other hand, fixing $\alpha_1 = \beta_1 = 1$ for these data resulted in fits that did not describe the relaxation features in the data very well. This suggests that the empirical HN model may not be the best choice to fully describe the dielectric response of these materials at low nanotube loadings.

4.4 Discussion

Pure PEO is a dielectric with a very low electrical conductivity. Each monomer of the polymer has a dipole moment due to the asymmetry of its -C-C-O- backbone. The dipole moment of the full polymer molecule is the vector sum of all of the monomeric dipoles, and thus depends on the configuration of the polymer molecule [34]. As seen in Figs. 4.2 and 4.3, both the real and imaginary parts of the permittivity of our nanocomposites increase with the addition of MWCNT. The MWCNTs are electrically conductive, leading to a large contribution to ϵ''. Their contribution to ϵ' is due to polarization of the graphene layers that make up the MWCNT [35]. The MWCNTs thus contribute significantly to the dielectric response of the nanocomposites at all concentrations, and indeed dominate it at concentrations higher than about 1 wt%.

Both ϵ' and ϵ'' increase significantly when MWCNT concentration is increased above the percolation threshold p_c. At MWCNT concentrations above p_c, ϵ'' is approximately inversely proportional to frequency over a large range of frequencies, indicating that the low-frequency electrical conductivity $\sigma = \omega\epsilon''\epsilon_0$ is constant. This is due to the electrical conductivity of the sample-spanning percolation network of highly conductive nanotubes.

The temperature dependence of the dc conductivity of the nanocomposites is described equally well within our experimental scatter by both an Arrhenius law and a 3D variable-range hopping model. The variable-range-hopping model has been successfully applied to bulk samples of single-walled carbon nanotubes below 60 K [31] and to composites of poly(3,4-ethylenedioxythiophene) and γ-Fe_2O_3 [36], in both cases giving a characteristic temperature T_0 on the order of 10^3 K. Fits of this model to our data, however, gave $T_0 \approx 10^8$ K, which seems unphysically high. On the other hand, fits of our dc conductivity data to an Arrhenius law gave activation energies ΔE on the order of tenths of an eV, which is consistent with values found in other systems [37, 38]. This leads us to favor the thermally-activated model for our materials, at least over the temperature range covered in our experiments. Even well above the percolation concentration, individual MWCNT will be separated from each other by thin "bridges" of insulating polymer. Our data suggest that transport of electrons across these

68

bridges is thermally activated. The overall conduction process is thus due to a combination of conductive transport along the nanotubes and thermally-activated transport from one nanotube to the next. A similar conduction process has been described in other nanocomposites [39]. It is interesting that the activation energy of these nanocomposites is in the range of common semiconductor materials, suggesting the potential for applications.

We performed a careful analysis of the behavior of the dc conductivity of our nanocomposites near the percolation transition. We observed a surprising difference between the behavior of samples prepared with the two mixing methods described above. Fits of the power-law expression, Eq. (4.1), to the data for the twin-screw extruded samples showed an extremely sharp minimum in χ^2, resulting in a well-defined value of the critical exponent t that was, within our experimental scatter, independent of temperature and in agreement with the theoretical value for a simple cubic 3D lattice [14, 40]. Our result, averaged over T, is $t = 1.9 \pm 0.2$. In contrast, the minimum in χ^2 from fits to the melt-mixed samples was extremely broad and the parameter values correspondingly poorly-defined; in this case we find a mean value of $t = 4.7 \pm 0.2$.

In an attempt to understand this difference, we reanalyzed the twin-screw data with the data point closest to (but above) the percolation threshold eliminated from the analysis. The resulting values of p_c and t were, within our estimated uncertainty, the same as the values obtained using all data points. This suggests that the differing behaviors for the two mixing methods is not simply due to a difference in the number of data points near the percolation threshold, but rather indicates a real difference in the behavior of the two types of samples. It seems likely that this could be due to differences in the distribution and degree of dispersion and isotropy of the nanotubes within the samples. In previous work, large values of t have been attributed to aggregation of the filler particles [16, 17], although we have no direct evidence for this here.

The behaviour of the slowest dielectric relaxation time τ_1 also changes as the concentration of MWCNT is increased, as seen in Fig.4.10. In pure PEO, τ_1 increases steeply as T is decreased. In this case, the relaxation mechanism must involve the relaxation of dipoles on

the polymer backbones due to the dynamics of the polymer chains, which slow dramatically as the system approaches the glass transition at 205 K. At 300 K, adding only 0.5 wt% MWCNT increases the relaxation time by three orders of magnitude. This is likely due to the nanotubes restricting the motion of the polymer chains. The relaxation of space charge distributions — presumably on the nanotubes — might also contribute to the dielectric relaxation on a similar time scale. Nonetheless, the observed temperature dependence, i.e., slowing of the relaxation as the glass transition temperature is approached from above, leads us to favour a process related to the polymer dynamics. For higher p, both the value of the relaxation time and its temperature dependence decrease as the nanotube concentration is increased. The polymer molecules can bind to the nanotubes, reducing the length of the free chains that contribute to the dielectric relaxation and thus reducing their relaxation time. It thus seems reasonable to suggest that the slower, temperature-dependent relaxation seen for $p \leq 1$ wt% is due to the dynamics of essentially the full polymer chains, perhaps constrained by the presence of nanotubes, while the faster relaxation times seen at higher p are due to the relaxation of short segments of polymer chain, with the ends of the segments bound to the surface of the nanotubes.

While a clear change in the behavior of τ_1 seems to take place at a nanotube concentration around the percolation threshold p_c, there does not seem to be an obvious reason why the percolation transition, which indicates the formation of a cluster of nanotubes on the scale of millimeters, should have a dramatic effect on the microscopic polymer dynamics. Rather, we suggest that the change is simply due to the increase in the number of nanotubes, and thus to the degree of polymer-nanotube interactions, and not to the percolation phenomenon specifically.

At concentrations $p \gtrsim 1$ wt%, we found that shape of the relaxation features in the dielectric spectrum was well described when the shape parameters in the HN model, α_1 and β_1, were both equal to 1. This suggests that the relaxation process at higher nanotube concentrations has a reasonably well-defined relaxation time. It is more difficult to interpret our results for these shape parameters at lower p. In some cases they are less than one, suggesting a broad distribu-

tion of relaxation times. In other cases, however, they take unphysical values, suggesting that, at least at low nanotube loadings, it is not appropriate to use the HN model for our system.

Most of our results are qualitatively similar for the melt-mixed samples and the twin-screw extruded samples. In particular, the overall nature of the dielectric response, the dielectric relaxation behavior, and the temperature dependence of the dc conductivity are, at least on a qualitative level, independent of the sample preparation method. The details of the percolation transition, however, are rather different for the two sets of samples, as discussed above. Our SEM images suggest some differences in the distribution of nanotubes in the two types of samples. The image of the M3.5 sample shown in Fig. 4.1(b) appears to show large clusters of nanotubes in the plane of the image, while the image of the T2.0 sample shown in Fig. 4.1(d) shows several smaller, relatively uniformly distributed clusters. There are undoubtedly spatial variations in the orientation and distribution of the nanotubes in these materials due to the way in which they are prepared, and these may well contribute to the observed differences at the percolation transition. Further work involving detailed microstructural measurements in conjunction with conductivity measurements would be required to resolve this question.

4.5   Conclusion

We have used broadband dielectric spectroscopy to study the complex permittivity and electrical conductivity of PEO-MWCNT nanocomposites made by melt mixing and twin-screw extrusion. ϵ', ϵ'' and σ_{dc} increased with increasing MWCNT concentration, and a percolation transition was observed at p_c = 1.23 ± 0.01 wt% for the twin-screw extruded nanocomposites, for which the percolation exponent was found to be 1.9 ± 0.1, and at p_c = 0.65 ± 0.05 wt% for the melt-mixed samples, for which t = 4.7 ± 0.2. The electrical conductivity of the nanocomposites increased by a factor of approximately 10^8 as the nanotube loading was increased from 0 to 5 wt%. The temperature dependence of the conductivity was well-described by a thermally-activated (Arrhenius) model, with a concentration-dependent activation energy

of a few tenths of an eV, comparable to that of common semiconductors. Electron transport in these nanocomposites is due to a combination of conductive transport along the nanotubes and thermally activated transport across thin polymer bridges separating one nanotube from another. The dielectric spectrum of the nanocomposites was dominated at low frequencies by the constant conductivity of the nanotubes. At low MWCNT concentrations, a strongly temperature-dependent relaxation peak is observed in the imaginary part of the spectrum, with the corresponding relaxation time increasing by several orders of magnitude as the glass transition temperature of the pure polymer is approached. At higher MWCNT loadings, the relaxation time was shorter — of order 10^{-6} s at $p = 3$ wt% — and very weakly dependent on T. We attribute the slower relaxation observed at low values of p to the motion of full polymer chains, and the faster relaxation seen at higher p to the motion of shorter chain segments, the ends of which are bound to the nanotubes. While most of the electrical properties we studied were qualitatively the same for both the melt-mixed and extruded samples, our results for the percolation transition are quite different in the two cases. The percolation exponent for the twin-screw extruded nanocomposites was in agreement with the value predicted for a simple cubic lattice, while that for the melt-mixed materials was much larger. In addition, the percolation threshold and critical exponent are much more well-defined for the former materials. These differences may be due to differences in the dispersion and degree of isotropy of the nanotubes in the two cases. In any case these results indicate that the sample preparation method can affect the electrical properties of the material near the percolation transition.

Bibliography

[1] E. Kymakis, I. Alexandou, and G. A. J. Amaratunga. *Synth. Met.*, 127:59, 2002.

[2] R. Haggenmueller, H. H. Gommans, A. G. Rinzler, J. E. Fischer, and K. I. Winey. *Chem. Phys. Lett.*, 330:219, 2000.

[3] G. S. Bocharov and A. V. Eletskii. *Int. J. Molec. Sci.*, 21:7634, 2020.

[4] P. Pötschke, S. M. Dudkin, and I. Alig. *Polymer*, 44:5023, 2003.

[5] J. N. Coleman, U. Khan, and Y K. Gun'ko. *Adv. Mater.*, 18:689, 2006.

[6] M. Moniruzzaman and K.I. Winey. *Macromol.*, 39:5194, 2006.

[7] P. Ma, N. A. Siddiqui, G. Marom, and J. Kim. *Compos. A: Appl. Sci. Manuf.*, 41:1345, 2010.

[8] L. Ma, L. Deng, and J. Chen. *Drug Dev. Indust. Pharm.*, 40:845, 2014.

[9] M. A. Repka, N. Langley, and J. Dinunzio. *Melt Extrusion, Materials, Technology and Drug Product Design*. Springer, 2013.

[10] W. Bauhofer and J. Z. Kovacs. *Compos. Sci. Tech.*, 69:1486, 2009.

[11] D.Stauffer and A. Aharony. *Introduction to Percolation Theory, Revised 2nd Edition*. CRC press, 2018.

[12] F. Du, J. E. Fischer, and K. I. Winey. *Phys. Rev. B*, 72:121404, 2005.

[13] S. Kirkpatrick. *Rev. Mod. Phys.*, 45:574, 1973.

[14] D. B. Gingold and C. J. Lobb. *Phys. Rev. B*, 42:8220, 1990.

[15] S. D. McCullen, D. R. Stevens, W. A. Roberts, S. S. Ojha, L. I. Clarke, and E. R. Gorga. *Macromol.*, 40:997, 2007.

[16] L. Karasek, B. Meissner, S. Asai, and M. Sumita. *Polym. J.*, 28:121, 1996.

[17] A. Abo-Hashem, H. M. Saad, and A. H. Ashor. *Plast. Rubber Composites Process Appl.*, 21:125, 1994.

[18] T. A. Ezquerra, M. Kulescza, C. Santa Cruz, and F. J. Balta-Calleja. *Adv. Mater.*, 2:597, 1990.

[19] N. N. Getangama, J. de Bruyn, and J. L. Hutter. *J. Chem. Phys.*, 153:044901, 2020.

[20] J. Yang, M. Melton, R. Sun, W. Yang, and S. Cheng. *Macromol.*, 53:302, 2020.

[21] M. Eesaee, E. David, and N. R. Demarquette. *Polym. Eng. Sci.*, 60:968, 2020.

[22] J. P. Runt and J. J. Fitzgerald. *Dielectric Spectroscopy of Polymeric Materials*. American Chemical Society, 1997.

[23] P. Debye. *Phys. Z.*, 13:97, 1912.

[24] K.S. Cole and R.H. Cole. *J. Chem. Phys.*, 9:341, 1941.

[25] S. Havriliak and S. Negami. *Polymer*, 8:161, 1967.

[26] T. Blythe and D. Bloor. *Electrical Properties of Polymers*. Cambridge University Press, 2005.

[27] M. Füllbran, P. J. Purv, and A. Schönhal. *Macromol.*, 46:4626, 2020.

[28] B. Carroll, S. Cheng, and A. P. Sokolov. *Macromol.*, 50:6149, 2017.

[29] M. Okutan, H. I. Bakan, K. Korkmaz, and F. Yakuphanoglu. *Phys. B: Condens. Matter.*, 355:176, 2005.

[30] N. F. Mott and E. A. Davis. *Electronic Processes in Non-crystalline Materials*. Oxford University Press, 2012.

[31] Y. Yosida and I. Oguro. *J. Appl. Phys.*, 86:999, 1999.

[32] W. H. Press, S. A. Teukolsky, W. T. Vetterling, and B. P. Flannery. *Numerical Recipes in C: The Art of Scientific Computing, 2nd ed.* Cambridge, 1992.

[33] C. Branca, S. Magazu, G.Maisano, F. Migliardo, P. Migliardo, and G. Romeo. *Phys. Scr.*, 67:551, 2003.

[34] N. Yamaguchi and M. Sato. *Polym. J.*, 41:588, 2009.

[35] B. Kozinski and N. Marzari. *Phys. Rev. Lett.*, 96:166801, 2006.

[36] K. Singh, A. Ohlan, P. Saini, and S. K. Dhawan. *Polym. Adv. Tech.*, 19:229, 2008.

[37] B. Kim, J. Lee, and I. Yu. *J. Appl. Phys.*, 94:6724, 2003.

[38] G. Chakraborty, K. Gupta, D. Rana, and A. K. Meikap. *Adv. Nat. Sci.: Nanosci. Nanotec.*, 4:025005, 2013.

[39] B. Wen, M. Cao, Z. Hou, W. Song, L. Zhang, M. Lu, H. Jin, X. Fang, W. Wang, and J. Yuan. *Carbon*, 65:124, 2013.

[40] J. Adler. *J. Phys. A: Mathematical and General*, 18:307, 1985.

Chapter 5

Rheological relaxation times of poly(ethylene oxide)-carbon nanotube nanocomposites

5.1 Introduction

Polymer nanocomposites are lightweight materials that are made by adding nanometer-sized filler particles to a polymer matrix. The properties of the nanocomposite can be enhanced over those of the pure polymer by choosing the right filler. For an example, the electrical and mechanical properties of a polymer can be improved by using carbon nanotubes (CNT) as fillers. Multi-walled CNT (MWCNT) can have Young's moduli as large as 0.9 TPa and tensile strength as high as 0.15 TPa [1]. The combination of these mechanical properties with their large length-to-diameter aspect ratio makes CNT an ideal candidate for an advanced filler material in polymer nanocomposites [2, 3, 4, 5]. The mechanical properties of polymer nanocomposites with fillers such as CNT, graphene oxide, and silica have been studied extensively [5, 6, 7, 8, 9, 10, 11]. In general, adding nanoscale fillers to polymers results in substantial increases in elastic and loss moduli, especially at low frequencies [11, 12]. Such nanocompos-

ites have potential applications in many areas, including conducting plastics, energy storage, conductive adhesives, and air and water filtration [9].

Despite previous work on polymer nanocomposites, there have been few studies of the shear rheology of nanocomposites, and the details of the polymer-filler interactions remain poorly understood. In this work, we use shear rheometry to perform frequency sweep, creep, and creep recovery experiments and study the mechanical properties of poly(ethylene oxide) (PEO)-multiwalled carbon nanotube nanocomposites. Our results provide information about the interactions between the MWCNT and the PEO molecules and the effect of the nanotubes on the viscoelastic properties of the nanocomposites. Abraham et al. [12] studied rheological properties of poly(ethylene oxide) (PEO)-MWCNT nanocomposite and observed an increase in shear viscosity and storage modulus with increasing MWCNT concentration.

Polymer nanocomposites are viscoelastic materials, and their viscous and elastic characteristics are important considerations for use in potential applications. We measure the elastic and viscous moduli (G' and G'', respectively) of our nanocomposites as a function of frequency by applying a small-amplitude sinusoidal strain to the material. The crossover frequency ω_f of G' and G'' corresponds to a mechanical relaxation process with a characteristic relaxation time τ_f given by [13]

$$\tau_f = \frac{1}{\omega_f}. \tag{5.1}$$

Creep due to, and recovery from, mechanical stress depend on time and temperature and determine a material's durability and reliability in applications. One of the main reasons for structural failure of a polymer-based material in an application is creep-induced deformation. Previous work has shown that adding a small amount of nanoparticles plays an important role in restricting the mobility of polymer chains, resulting in an improvement in structural stability [14, 15]. Furthermore, it has been reported that adding nanofillers can increase creep resistance under different stress levels [10, 16]. In a creep test, the stress on a sample is increased from zero to a constant value σ_0 at time zero. The resulting strain is then measured as a function of time. We fit the creep strain as a function of time using the well-known Burgers model [10, 17].

In this model, the creep strain is given as a function of time t by

$$\gamma(t) = \frac{\sigma_0}{E_M} + \sum_{i=1}^{2} \frac{\sigma_0}{E_{ki}} \left[1 - \exp\left(\frac{-t}{\tau_i}\right) \right] + \frac{\sigma_0 t}{\eta_M} + at, \qquad (5.2)$$

where σ_0 is the applied constant stress. In this expression, the first term of the equation represents the elastic (instantaneous) deformation corresponding to the Maxwell model with elastic moduli E_M, the second term indicates two delayed viscoelastic deformations corresponding to the Kelvin-Voigt model with relaxation times τ_i and elastic modulus E_{ki}, the third term represents Newtonian flow behavior with viscosity η_M, and the fourth term, which is not in the original Burgers model, is intended to model a slowly varying strain resulting from residual stresses in the sample due to the sample preparation process (see below).

At time t_0, the applied stress is removed. The component of the accumulated strain due to elastic deformation will then recover over time. We use a modified Weibull distribution [10, 17] to describe the creep recovery data obtained in our experiments. In this distribution, the recovering strain is given by

$$\gamma_r(t) = \sum_{i=1}^{2} \gamma_{vi} \left[\exp\left(-\left(\frac{t - t_0}{\tau_{ri}} \right) \right) \right] + at + \gamma_\infty, \qquad (5.3)$$

where γ_{vi} and τ_{ri} are strain recovery amplitudes and characteristic relaxation times. Eq. 5.3 has two relaxation processes. The second term on the right represents the same sample-preparation-dependent creep as in Eq. 5.2, and γ_∞ is the irreversible strain remaining as $t \to \infty$ due to viscous flow of the sample.

The nanocomposite samples are subject to significant unknown and uncontrollable internal stresses resulting from the sample fabrication process. These stresses relax very slowly, over a time scale that depends on temperature and is much longer than the duration of our experiments. We represent the contribution to the strain resulting from these internal stresses by a linear term at in Eqs. 5.2 and 5.3. We determined a for a given sample and temperature by fitting the creep recovery data to Eq. 5.3. We then used the same value of a when fitting the creep data to

78

Burger's model.

In what follows, our experimental data are discussed in terms of the microstructure of the nanocomposites and the microscopic interactions between carbon nanotubes and the polymer molecules.

5.2   Experiment

We prepared nanocomposites of PEO and multi-walled carbon nanotubes using melt mixing compounding and compression molding. PEO powder with a molar mass of 100,000 g/mol was purchased from Sigma-Aldrich and used as received. MWCNT with diameter 8–15 nm and length 30–50 μm were purchased from TimeNano Chengdu Organic Chemicals and used as received.

50 g of PEO powder and the required amount of MWCNT were added to a Brabender three-piece mixer equipped with two counter-rotating blades and preheated to 75 °C. The PEO powder and the MWCNT were mixed for 10 minutes, then removed from the mixer and cooled to room temperature. The resulting material was then pelletized to obtain particles of a suitable size for the compression molding. Disks of the nanocomposites 50 mm in diameter and 1 mm thick were made by transferring the small pellets of PEO/MWCNT to a room temperature mold made from 3.2 mm thick aluminum plates separated by a 1 mm thick aluminum gasket with three 50 mm diameter holes in it. The filled mold was heated to 75 °C for 5 min, then compressed under 13.3 kN of force for 5 min. Finally, the mold was cooled to room temperature and the disks were removed.

We followed this procedure to make nanocomposites with MWCNT concentrations ranging from 0 to 5% by weight. In this work, we label our samples by the letter M to indicate melt-mixing followed by the amount of MWCNT added, given as a percentage of the total sample weight. For example, a 1.0% PEO-MWCNT nanocomposite is referred to as M1.0.

Scanning electron microscope (SEM) images of the nanocomposite samples were obtained

using a Zeiss 1540XB SEM with an acceleration voltage of 1.0 keV. Surfaces suitable for imaging were prepared by quenching the samples in liquid nitrogen and fracturing. The newly-exposed cross-sections were then coated with a conducting layer of osmium before imaging with the SEM.

The viscoelastic properties of the nanocomposites were measured using an Anton-Paar MCR-302 rotational shear rheometer with a 50 mm diameter parallel-plate tool. The bottom plate had a roughness of 25 μm, while a 50 mm diameter disk of 280 grit sandpaper was attached to the top plate to avoid slip between the sample and the tool. The temperature range of our experiments includes the melting temperature of the nanocomposite samples, and the volumes of the samples change as they melt. To accommodate this, we set the rheometer to apply a constant normal force to the sample to maintain proper contact between the sample and the parallel plate. Because of this, the gap between the rheometer plates varied slightly with sample temperature over the course of a run. This was taken into account in our data analysis. The rheometer was set to the desired temperature and held at that temperature for 15 minutes to ensure equilibrium before performing experiments. We raised the sample temperature from 60 to 85 °C in 5 °C increments, then lowered it back to 60 °C, again in 5 °C steps, waiting 15 minutes at each step for the sample temperature to equilibrate. The temperature was cycled in this way several times for a given experiment, with viscoelastic data collected at each temperature step.

In the frequency sweep experiments, the 50 mm diameter PEO nanocomposite disks were placed coaxially between the plates of the rheometer. The upper plate was lowered until the normal force on the sample was 2 N. The temperature was set as described above, then frequency sweeps carried out using a strain amplitude of 0.5%, which we confirmed is well within the linear regime. The measurements were taken over the angular frequency range 0.1 rad/s $\leq \omega \leq$ 100 rad/s and, for these experiments, the temperature was cycled twice.

In creep experiments, it is important to keep the materials in the linear regime to avoid significant structural changes. Therefore, we first performed amplitude sweeps at 10 rad/s to

Table 5.1: The stress σ_0 used for each sample in the creep experiments.

Sample	σ_0 (Pa·s)
M0.0	0.08
M1.0	0.3
M2.0	4.0
M3.0	2.0
M5.0	55

determine the linear regime of our samples. All the nanocomposites were kept in the linear regime while performing the creep test. A new nanocomposite sample was used for the creep and recovery tests. The same parallel-plate configuration of the rheometer was used, but with the normal force set to 0.5 N. We wished to keep the deformation of the samples within the linear viscoelastic regime throughout these experiments. To achieve this, each sample was first heated to 70 °C, a set of stresses was applied, and the resulting strain was measured. Based on these results, the stress σ_0 to be used in the creep experiments was chosen so that the maximum strain was a few percent and was well within the linear regime. The values of σ_0 used for each sample are shown in Table 5.1. After σ_0 had been determined, the sample was cooled down back to 60 °C to start the first cycle of the creep experiment. When the desired temperature was reached as explained above, the stress σ_0 was applied to the sample for 15 minutes and the corresponding strain γ was measured as a function of time. After 15 minutes of creep, the stress was set to zero to start the recovery portion of the experiment, and the strain was measured for another 15 minutes as the sample relaxed. Both the creep and recovery measurements were taken over up to 4 heating-cooling cycles.

5.3   Results

Fig. 5.1 shows SEM images of PEO-MWCNT nanocomposites prepared with relatively low (0.5 wt%) and relatively high (3.5 wt%) MWCNT concentrations. These images show a portion of a cross-sectional surface of the nanocomposites obtained by freeze-fracture, as described above.

In the image of the M0.5 sample shown in Fig. 5.1(a), a small cluster of nanotubes can be seen at the center of the image. On the scale of this image, the distribution of nanotubes is far from uniform. However, it appears more homogeneous on millimeter scales. The image of the M3.5 sample shown in Fig. 5.1(b) shows more clusters distributed over most of the image area and the distribution is homogeneous on the sample scale. Upon solidification of the melt during sample preparation, PEO polymer chains fold together and form ordered regions known as lamellae, which can be seen as groups of parallel lines in the SEM images. The PEO chains are oriented perpendicular to the lamellae. Both the SEM images show polymer lamellae throughout the sample. One region of lamellae is indicated in Fig.5.1 (b). The overall appearance of both samples is similar to that of the PEO-MWCNT samples used by us in previous work in Chapter 4.
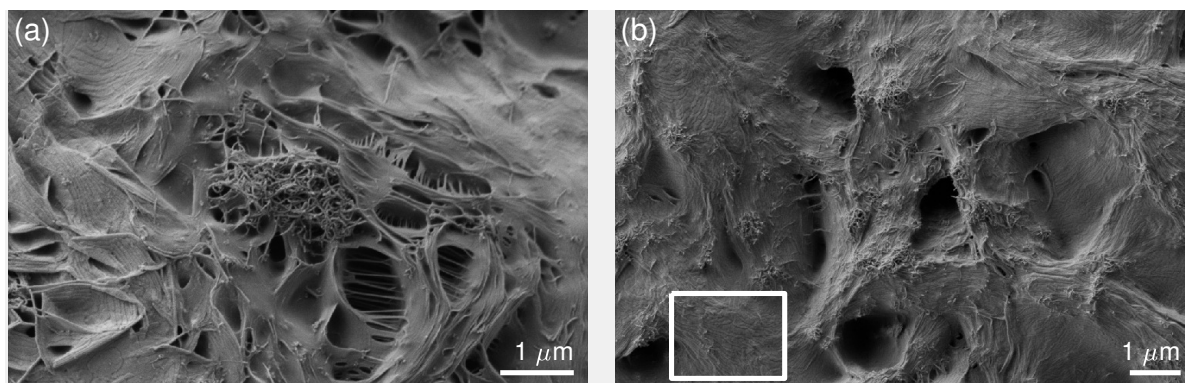
Figure 5.1: SEM images of PEO-MWCNT nanocomposites (a) M0.5 and (b) M3.5, respectively. The white square in (b) shows a region with polymer lamellae. These images are discussed in detail in the text.

The viscoelastic behavior of the nanocomposites is exemplified by the frequency sweep data shown in Fig. 5.2 for sample M1.0. This figure shows the elastic and viscous moduli at temperatures ranging from 60 to 80 °C during the heating phase of the second thermal cycle. At 60 °C, which is below the melting temperature of pure PEO (around 65 °C), G' and G'' are about 10^5 and few times 10^4 Pa respectively, indicating that the behavior of the material is primarily elastic. When the temperature is increased through the melting point to 70 °C, both G' and G'' decrease. G' drops more than one order of magnitude below 1 rad/s and the drop in

G' is always larger than that of G'' at any frequency.

At temperatures of 70 °C and above, G' and G'' cross over within the frequency range studied for this concentration. G'' is larger than G' below the crossover frequency, implying primarily viscous behavior at low frequencies. This is typical of entangled polymer melts, with τ_f, the reciprocal of the crossover frequency, typically being taken as a measure of the reptation time of the polymer molecules. The inset in Fig. 5.2 shows the variation of the relaxation time τ_f with temperature. At temperatures below 70 °C, the crossover frequency was lower than the lower limit of our experimental frequency range so τ_f could not be measured. τ_f decreases with increasing temperature.
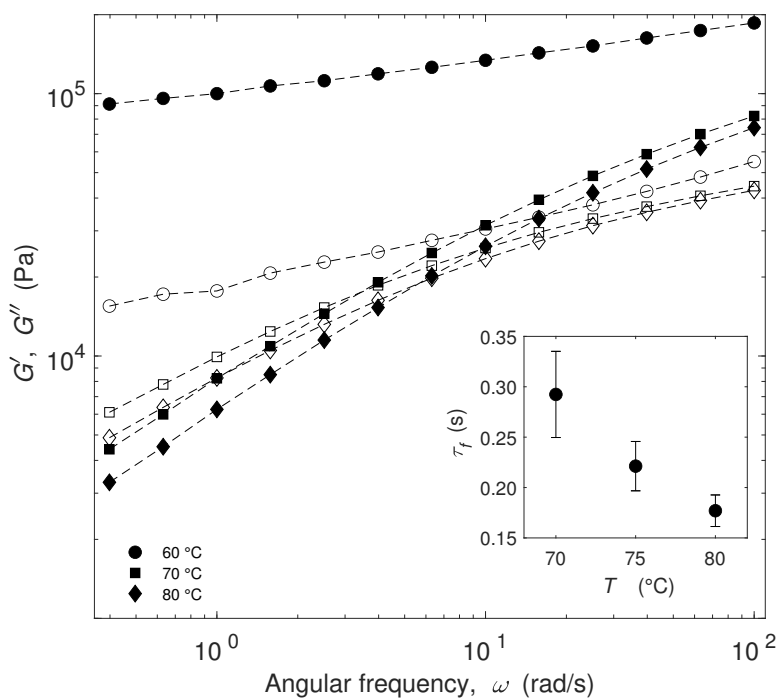
Figure 5.2: Storage modulus G' (solid symbols) and viscous modulus G'' (open symbols) of M1.0 versus angular frequency ω at different temperatures during the heating phase of cycle 2. The lines are guides to the eye. The inset shows the variation of relaxation time τ_f measured as the inverse of crossover frequency of G' and G'' as a function of temperature. The crossover frequency was out of our experimental frequency range for temperatures below 70 °C.

The elastic and viscous moduli of our nanocomposites at 75 °C are shown as a function of MWCNT concentration during the heating phase of thermal cycle 2 in Fig. 5.3. Both G' and G'' increase with MWCNT loading, especially at low frequencies. At low frequencies where

the time scales are long enough to show the unraveling of entanglements, the Maxwell model predicts $G' \propto \omega^2$ and $G'' \propto \omega$ [18]. This low frequency regime is called the terminal regime. The power law dependence we observe is not as strong in either case, however, indicating that our experimental frequencies are not low enough to be in the material's terminal regime. Nanocomposites with MWCNT concentrations up to 2.0 wt% show a crossover frequency within our experimental frequency range, below which the material's behavior is primarily viscous, and above which it is primarily elastic. Above 2 wt%, the crossover frequency was below the lower limit of our experimental frequency range and the materials are therefore solid-like (i.e., predominantly elastic) over the full frequency range studied. The mechanical relaxation time τ_f is shown as a function of MWCNT concentration p in the inset of Fig. 5.3. τ_f increases with increasing p from 0.14 ± 0.01 s for pure PEO to 2.4 ± 0.3 s for M2.0. The increase in τ_f between 1.5 and 2 wt% is dramatically larger than at lower concentrations.
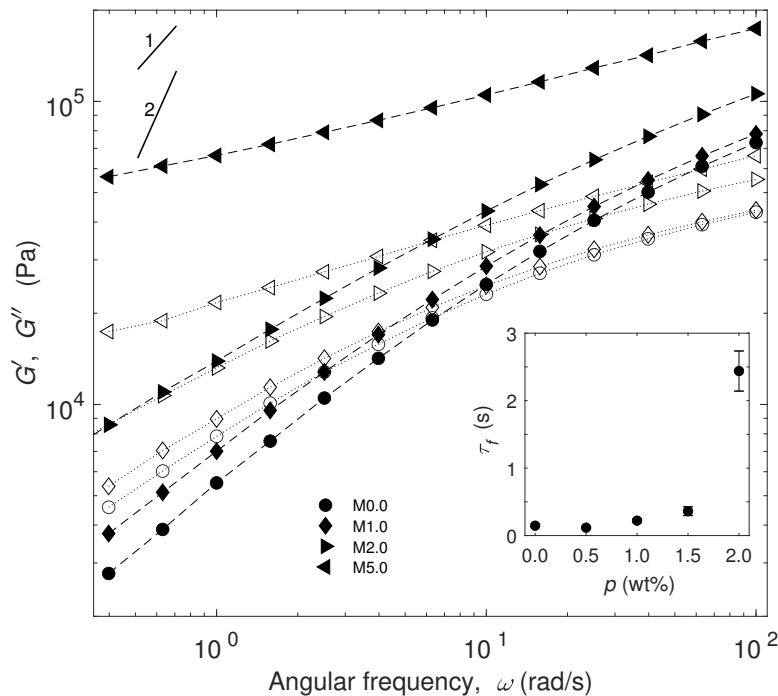
Figure 5.3: Storage modulus G' (solid symbols) and viscous modulus G'' (open symbols) versus angular frequency ω at 75 °C measured during the heating phase of cycle 2. The different symbols represent different MWCNT concentrations from 0 to 5 wt%. The lines are guides to the eye. The inset shows the relaxation time as a function of MWCNT concentration p. The lines with slope 1 and 2 are shown to compare the low frequency behaviour of G'' and G', respectively.
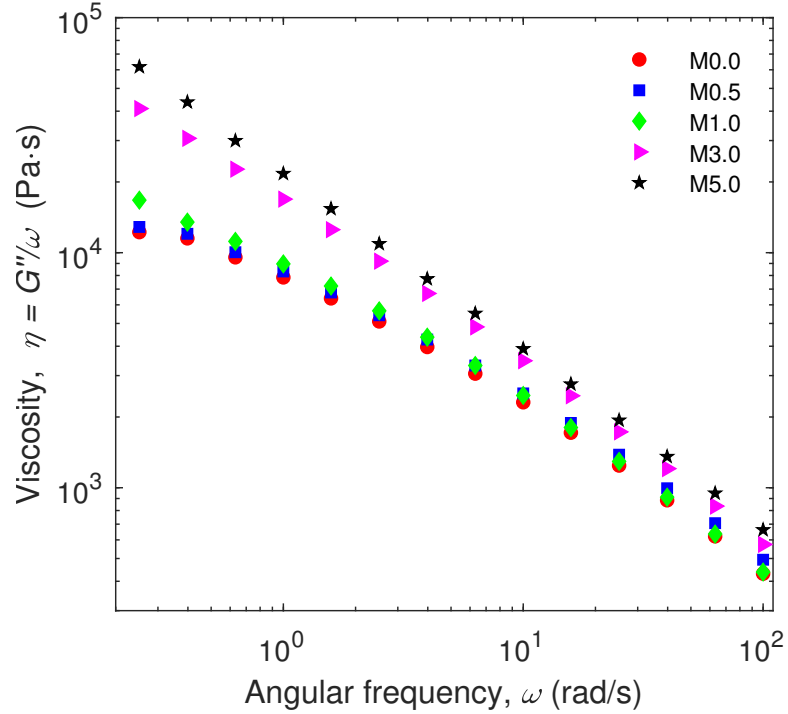
Figure 5.4: Frequency dependence of viscosity η at 75 °C during the heating phase of cycle 2. The different symbols represent different MWCNT concentrations from 0 to 5 wt% as indicated in the legend.

The viscosity $\eta = G''/\omega$ is plotted as a function of angular frequency in Fig. 5.4 for measurements obtained at 75 °C during the heating phase of thermal cycle 2. η increases with p at any given frequency, and decreases with frequency following a power law with exponent between −0.7 and −0.8 for all the nanocomposites for $\omega > 3$ rad/s. One expects η to approach a constant at low frequencies for an entangled polymer melt [18]. We see the start of this behavior at low MWCNT concentrations, but at higher concentrations, our experimental frequency range does not extend low enough for us to observe this plateau in η. These results suggest that there are some very slow dynamics in these systems on longer time scales, i.e., at lower frequencies, than studied here.

G' and η at an angular frequency of 1 rad/s are plotted as a function of MWCNT concentration at 80 °C during the heating phase of cycle 2 in Fig. 5.5. Both G' and η slowly increases with p for $p \leq 1$ wt%, then increase at a slightly higher rate for higher MWCNT loadings. The overall change in both G' and η as p increases from 0 to 5 wt% is only about a factor of three,
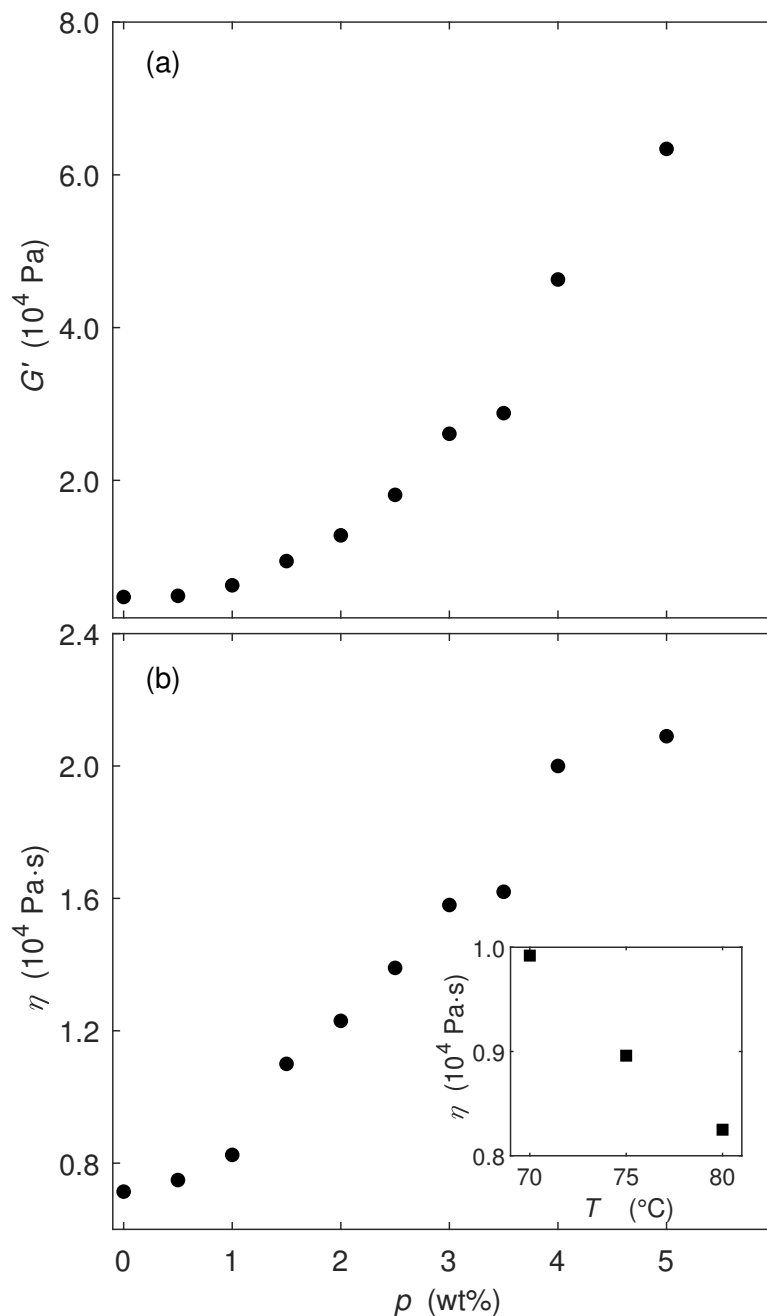
Figure 5.5: (a) Elastic modulus G' and (b) viscosity η at 1 rad/s versus MWNCT weight concentration p at 80 °C. The inset in (b) shows the viscosity at 1 rad/s of M1.0 at different temperatures.

however. The inset in Fig. 5.5 (b) shows the variation of η at an angular frequency 1 rad/s for sample M1.0 as a function of temperature during the heating phase of cycle 2. η decreases by about 20% as the temperature increases from 70 to 80 °C.

The long-time behavior of the nanocomposites was studied by measuring the elastic and
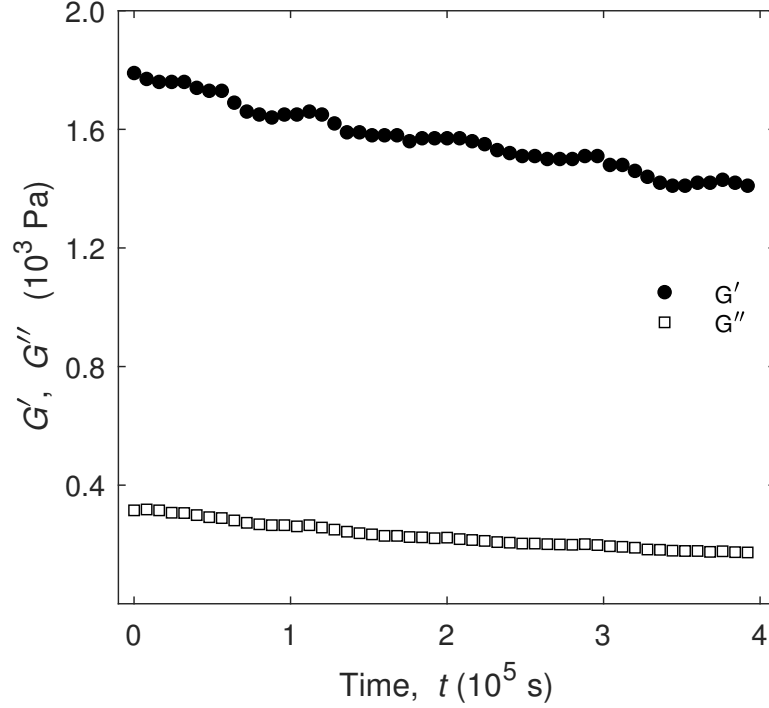
Figure 5.6: Storage modulus G' and viscous modulus G'' of M5.0 versus time at 75 °C. The measurements were taken at f = 1 Hz and a strain amplitude of 0.5%.

viscous moduli over several days at a constant frequency of 1 Hz with a strain amplitude of 0.5%. Fig. 5.6 shows the results for M5.0 at 75 °C. Both G' and G'' decrease steadily with time even after several days, indicating a very slow evolution of the sample's properties.

In the creep and recovery experiments, strain $\gamma(t)$ is measured as a function of time. In our measurements, the applied stress is different for each sample, as shown in Table 5.1. Therefore, we present the creep data in the form of the creep compliance

$$J(t) = \gamma(t)/\sigma_0 \tag{5.4}$$

and the recovery data as the recoverable compliance

$$J_r(t) = \frac{\gamma_{\max} - \gamma_{r(t)}}{\sigma_0}, \tag{5.5}$$

where $\gamma_{\max}$ is the maximum strain attained during the creep stage of the experiment, $\gamma_r(t)$

87

is the strain during the creep recovery stage and σ_0 is the constant stress applied during the creep measurement. This allows an unbiased comparison of the data for different samples. For clarity, we plot only every tenth data point in graphs of the creep and recovery data.

We observed changes in the mechanical properties as the materials were cycled thermally. In other words, our samples do not reach a steady state, even after several days (Fig. 5.6) or after four thermal cycles. Possible reasons for this are discussed below.
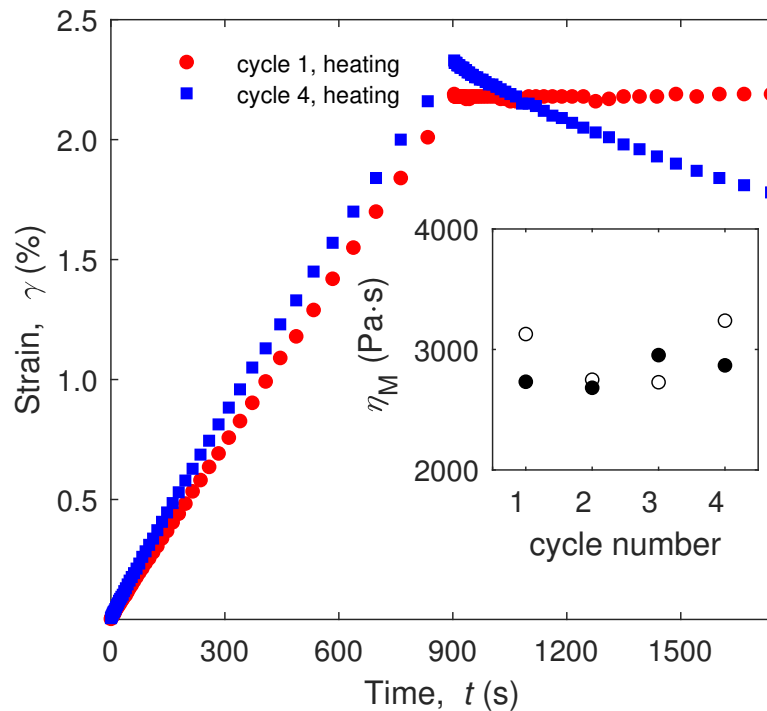
Figure 5.7: Creep and recovery strain versus time for M0.0 at 75 °C during the heating phase of cycle 1 and 4. The inset shows the viscosity η_M of M0.0 at 75 °C during the heating phase as a function of thermal cycle number. The open and solid symbols represent heating and cooling data respectively. The uncertainty in η_M is indicated by the scatter in the data.

Figure 5.7 shows both creep and recovery strain data for M0.0, at 75 °C during the heating phases of cycles 1 and 4. In both cycles, γ increases almost linearly during creep, but is slightly higher in cycle 4 than in cycle 1. Interestingly, however, there are significant changes in the strain during the recovery phase of the experiment, with a much faster recovery in cycle 4 compared to cycle 1. This suggests sample M0.0 becomes much more elastic as it goes through the thermal cycles. However, in all the nanocomposites, both the creep strain and recovery

strain decrease with increasing thermal cycles. The inset of Fig. 5.7 shows the viscosity η_M determined from fits of Eq. 5.2 to the data of M0.0 at 75 °C as a function of thermal cycle, with open and solid symbols representing heating and cooling respectively. η_M is about 3100 Pa·s
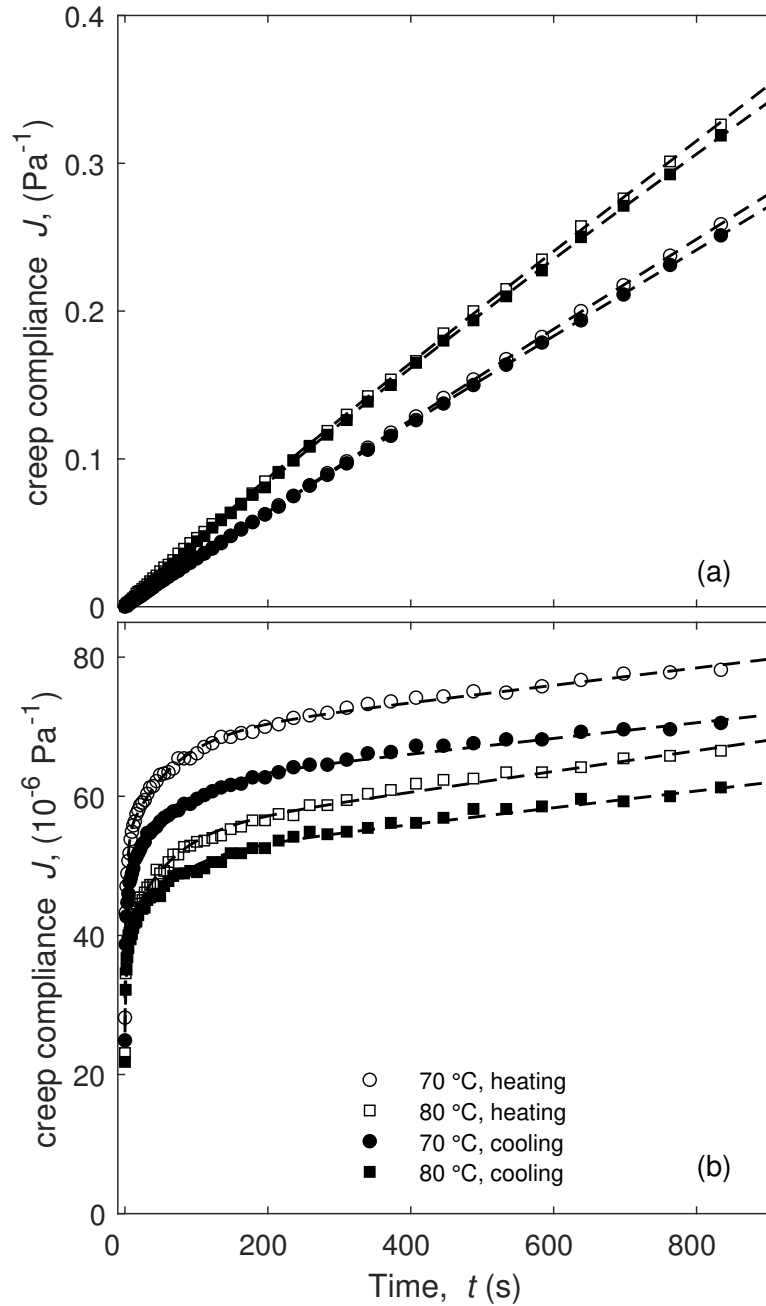
Figure 5.8: The creep compliance versus time at different temperatures in thermal cycle 3 for (a) M0.0 and (b) M5.0, respectively. Open and solid symbols indicate data at 70 and 80 °C in the heating and cooling phase, respectively. The different symbols represent different temperatures. The dashed lines are fits to Eq. 5.2 divided by σ_0.

in the heating phase of the first cycle, and it does not change significantly with thermal cycles in both heating and cooling phases. In what follows we mainly show data for cycle 3.

Fig. 5.8 shows results from a series of creep measurements on samples M0.0 and M5.0 at two different temperatures during both the heating and cooling phases of cycle 3. The change in compliance with t is substantially larger for M0.0 than M5.0. The compliance of M0.0 (Fig. 5.8 (a)) increases nearly linearly with time, indicating that the behaviour of pure PEO under a constant stress of $\sigma_0 = 0.08$ Pa is almost purely viscous. When the temperature increases from 70 to 80 °C in cycle 3, the creep compliance and its slope, which is related to the sample's viscosity, increases. We observe no significant hysteresis in J for M0.0. Creep compliance data for M5.0 are shown in Fig. 5.8(b). At this nanotube loading, the compliance first increases rapidly with time, then approaches a constant slope at later times. Surprisingly, J for M5.0 decreases when T is increased from 70 to 80 °C and then increases when the sample is cooled. In contrast to what was observed for M0.0, there is a clear hysteresis in J at the higher nanotube loading, since the compliance values obtained during the heating phase of the cycle are higher than those measured on cooling. The dashed lines in the figure are the creep compliance calculated by dividing fits of $\gamma(t)$ to Eq. 5.2 by σ_0. For M0.0, we need only one relaxation term and the linear terms of Eq. 5.2 to adequately fit the experimental data. The linear appearance of $J(t)$ data shown in Fig. 5.8(a) indicates that the relaxation term is small. For all other nanotube concentrations, fits to the model required the linear terms and two relaxation terms.

The relaxation times τ_1 and τ_2 obtained from the fits to Eq. 5.2 are plotted in Fig. 5.9 as a function of nanotube concentration p at $T = 75$ °C in the heating phase of cycle 3. τ_f from the frequency sweep data in the heating phase of cycle 2 is also shown in the figure. τ_1 has a value of several seconds and τ_2 is on the order of 100 s. There is no τ_1 for M0.0, as discussed above. The large separation between τ_1 and τ_2 indicates that these time constants characterize two very different relaxation processes. τ_f is less than τ_1 for low concentrations, but increases to become roughly equal to τ_1 at $p = 2$ wt%. This indicates the presence of a third, faster relaxation process at low nanotube loading. τ_1 is similar for all thermal cycles, while τ_2 shows
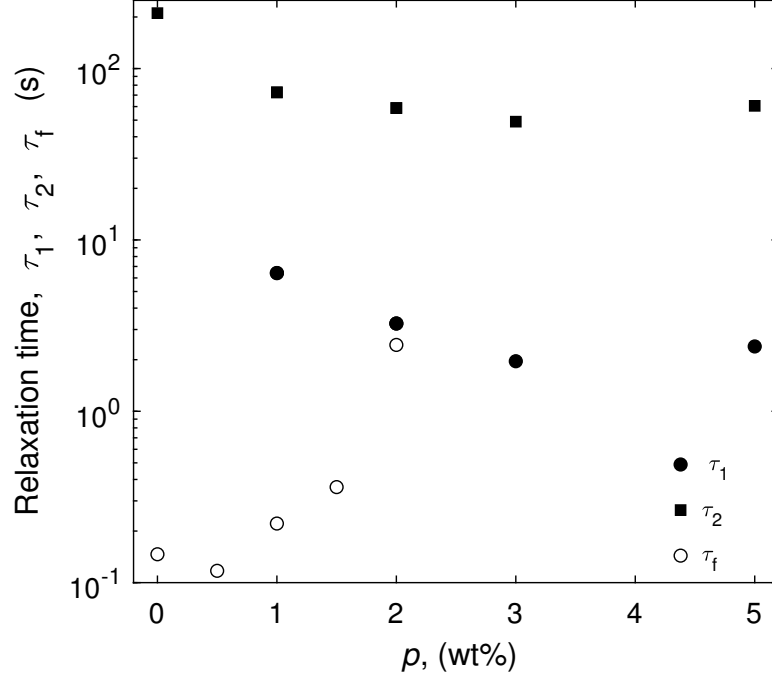
Figure 5.9: Relaxation times τ_1 and τ_2 as a function of MWCNT concentration p obtained from fits of creep data to Eq. 5.2 at 75 °C during the heating phase of thermal cycle 3. τ_f is the relaxation time shown in Fig. 5.3 from the frequency sweep measurement for comparison.

variability, particularly for early thermal cycles.

The third term in Eq. 5.2 describes the contribution to the creep strain due to the material's viscosity. We have added an additional linear term to this equation, *at*, to account for the slow evolution of sample properties discussed above, which is observed in both creep and recovery. The contribution due to viscosity was separated from the *at* term by using the value of *a* determined from fits of Eq. 5.3 to the recovery curves, for which there is no other linear contribution. The variation of η_M at 75 °C in the heating phase of cycle 3 with MWCNT concentration p is shown in Fig. 5.10. The viscosity is on the order of 10^3 Pa·s for the pure polymer, and increases to above 10^5 Pa·s for $p = 1.0$ wt%. As the concentration of MWCNT is increased further, η_M continues to increase rapidly, and is nearly 10^8 Pa·s for $p = 5.0$ wt%, about five orders of magnitude higher than for pure PEO.

The effect of CNT loading on the fractional recoverable compliance, $J_r/J_{\max}$, of M0.0 and M5.0 is illustrated in Fig. 5.11(a) and (b) respectively, at 70 and 80 °C during the heating
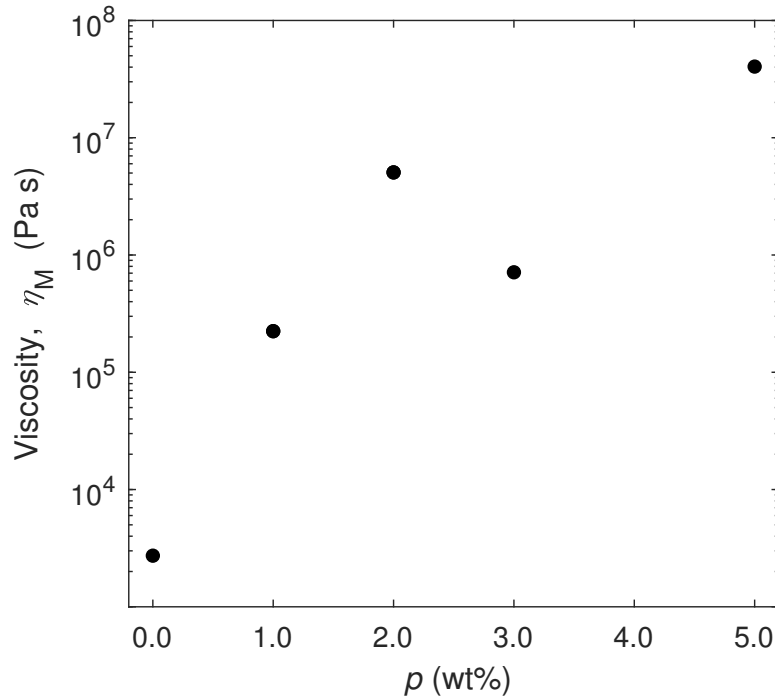
Figure 5.10: Viscosity η_M of the nanocomposites obtained from fits of creep data to Eq. 5.2 plotted as a function of MWCNT concentration p at 75 °C during the heating phase of cycle 3. The uncertainties of η_M given by the fits are within the symbols, while the non-monotonic behavior is more likely due to variations in the internal structure of the samples resulting from their preparation.

and cooling phases of thermal cycle 3. The dashed lines in the figure are from fits to Eq. 5.3. For M0.0, one exponential term in Eq. 5.3 was sufficient to describe the data, while two relaxation terms were used for all other fits, as in the creep fits. The pure polymer shows very slow recovery, faster at 80 °C than at 70 °C. The recoverable compliance for M0.0 did not approach close to 100% within our experimental time due to the substantial non-recoverable viscous strain. The maximum recovery for this sample over the 900 s of our measurement was about 20% at 80 °C. The percent recoverable compliance of sample M5.0 is large compared to M0.0 and increases rapidly with t over the first 50 s of the recovery experiment, after which it increases more slowly with a longer relaxation time. The trend in recoverable compliance with temperature is almost the same for the two temperatures in both the heating and cooling phases of the experiment, with roughly 95% of the compliance recovered over 900 s at both temperatures.
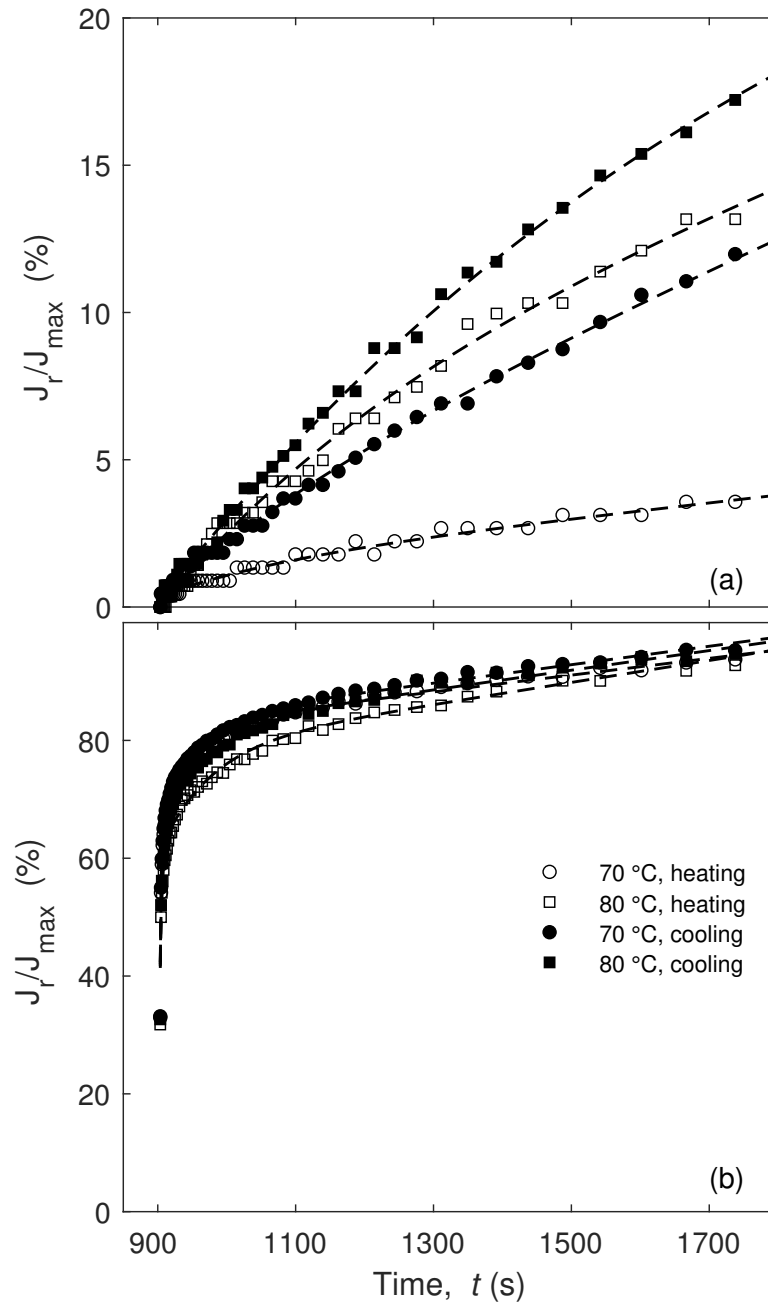
Figure 5.11: The percent recoverable compliance as a function of time for (a) M0.0 and (b) M5.0 samples measured during creep recovery experiments at 70 and 80 °C in the heating and cooling phase of cycle 3, respectively. The lines are from fits to Eq. 5.3 as explained above.

The creep and recoverable compliance data for nanocomposites with different MWCNT loadings are compared in Fig. 5.12 for measurements obtained at 80 °C during the heating phase of thermal cycle 3. The data for J_r have been shifted in time to overlap with the creep compliance data for easy comparison. Both J and J_r decrease rapidly with increasing MWCNT
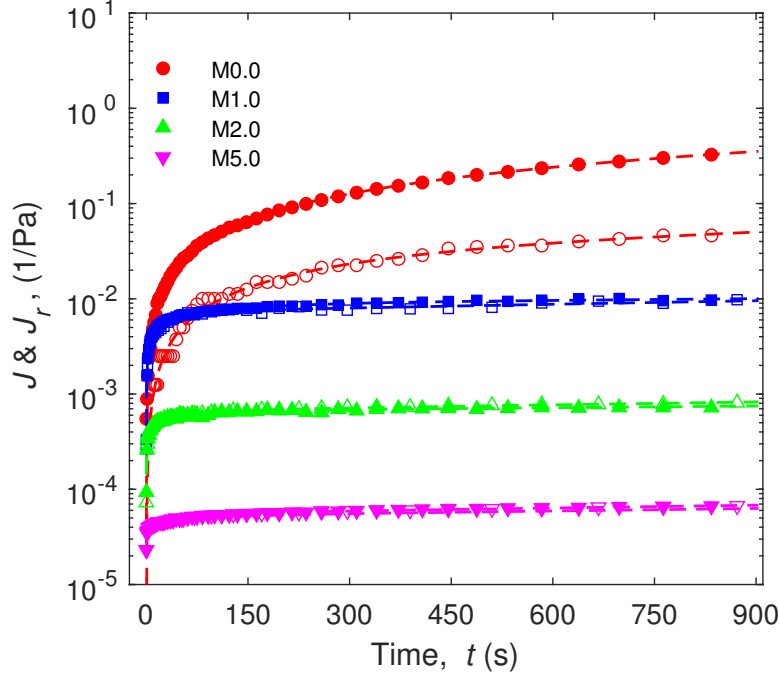
Figure 5.12: Creep J (solid symbols) and recoverable compliance J_r (open symbols) as a function of time for different MWCNT concentrations measured at 80 °C during the heating phase of cycle 3. The lines are from fits to Eq. 5.2 and 5.3 as explained above.

concentration. The gap between J and J_r indicates only a fraction of compliance was recovered for M0.0, as seen in Fig. 5.11. For nonzero nanotube loadings, in contrast, the creep and recoverable compliance graphs overlap almost perfectly. This means that, in nanocomposites containing MWCNT, almost all of the strain is recovered after the stress is removed. Figure 5.12 also confirms the increase in elastic modulus with p as the size of the instantaneous response in creep compliance drops dramatically with MWCNT concentration.

The characteristic relaxation times τ_{r1} and τ_{r2} obtained from fits of Eq. 5.3 to the creep recovery data are plotted in Fig. 5.13 as a function of MWCNT concentration at 75 °C in the heating phase of cycle 3. For M0.0 (pure PEO), Eq. 5.3 with one exponential term fits the data well, giving a relaxation time of around 10^2 s. The creep recovery data for all the other nanocomposite samples required two relaxation terms in Eq. 5.3 to fit the experimental data well. As in the case of the creep data discussed above, the two relaxation times τ_{r1} and τ_{r2} differ by about an order of magnitude, and they are equal within our experimental uncertainties
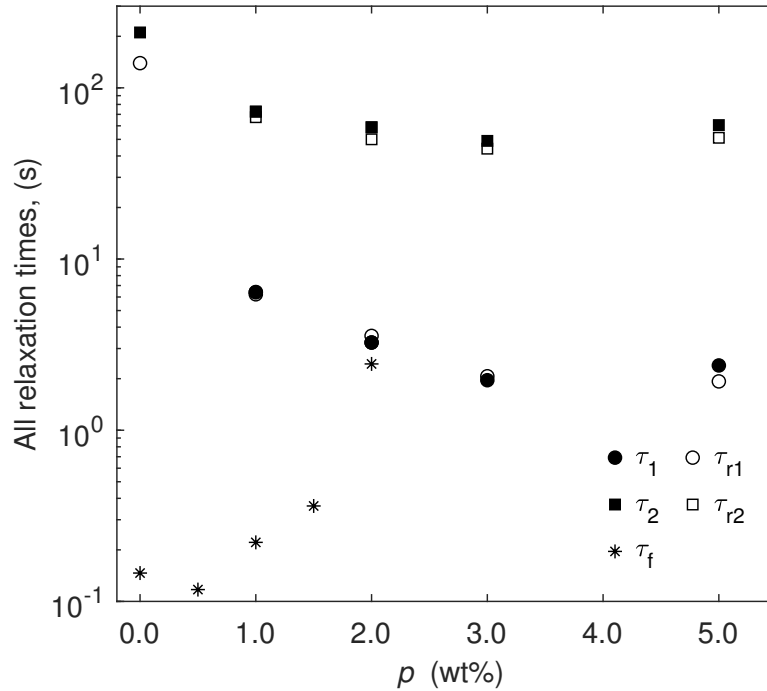
Figure 5.13: Characteristic relaxation times (τ_{r1} and τ_{r2}) of creep recovery at 75 °C in the heating phase of cycle 3 plotted as a function of MWCNT concentration p. M0.0, or pure PEO, only required one relaxation term of Eq. 5.3 to fit the data, while other concentrations required two relaxation terms. The uncertainties given by the fits are within the symbols. τ_f, the relaxation times from the frequency sweep measurements (Fig. 5.3) and τ_1 and τ_2, the relaxation time from the creep measurements (Fig. 5.9), are shown for comparison.

to the time constants τ_1 and τ_2 obtained from the creep data.

The relative contribution of the two exponential terms to the creep recovery was determined by calculating the ratio γ_{v1}/γ_{v2}. The result is shown in Fig. 5.14. All the weighted amplitudes are order of 1, indicating that both relaxation terms contribute approximately equally to the relaxation of the material.

The fractional recoverable compliance, $J_r/J_{\max}$, for M0.0, M1.0 and M5.0 is shown in Fig. 5.15 as a function of time for measurements obtained at 75 °C during the heating phase of each cycle. For M0.0, the percent recoverable compliance is very small in the first two thermal cycles and increases with further thermal cycling, as seen in Fig. 5.7. In contrast, a significant portion of the compliance is recovered in the first thermal cycle of M1.0 with more recovered in further cycles. The nanocomposite with the highest MWCNT concentration (M5.0) recovers more than 80% of the compliance, with little increase after the second thermal cycle.
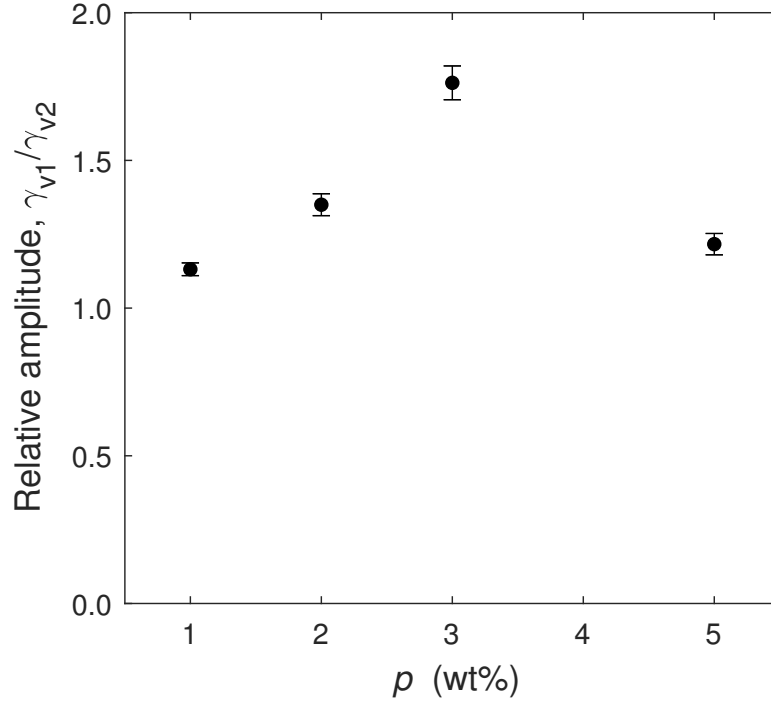
Figure 5.14: The ratio of the amplitudes (γ_{v1}/γ_{v2}) of the relaxation terms in Eq. 5.3 obtained during the heating phase of cycle 3 plotted as a function of MWCNT concentration at 75 °C.
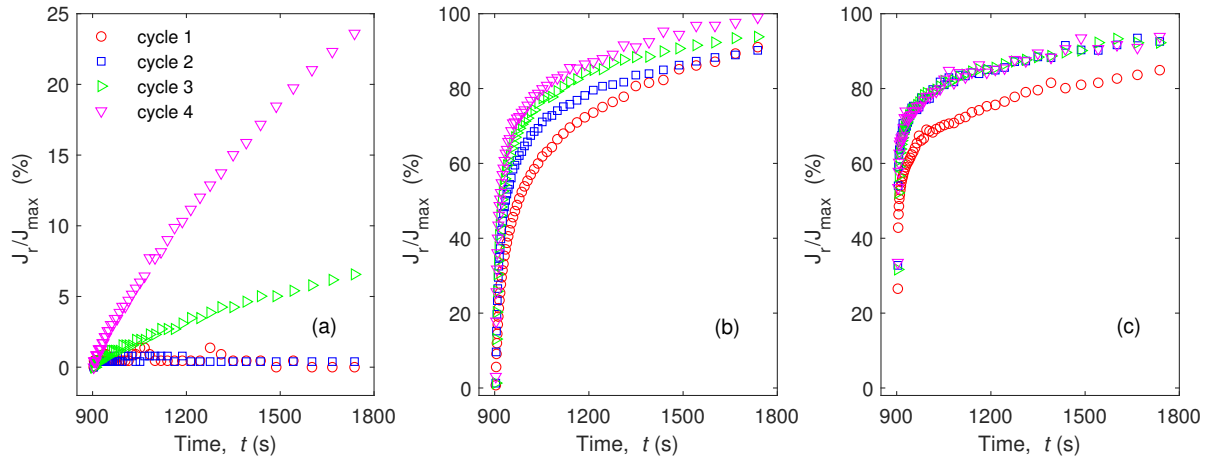
Figure 5.15: The percent recoverable compliance vs time for (a) M0.0, (b) M1.0, and (c) M5.0 at 75 °C during the heating phase of different thermal cycles.

5.4 Discussion

We studied the mechanical properties of PEO/MWCNT nanocomposites by performing frequency sweep, creep, and creep recovery measurements. These experimental data demonstrate the existence of several different relaxation times in the nanocomposites. The relaxation time

τ_f from the frequency sweep experiments gives information about relatively short time-scale processes. The creep and recovery measurements probe longer time scales, corresponding to slower processes that involve longer length scales.

Let us first examine the behaviour of M0.0, the pure polymer. The PEO used in our experiments has a molar mass of 100,000 g/mol and is an entangled polymer in the melt [19]. The crossover of G' and G'' observed in the frequency sweep experiments is usually identified with the reptation time of an entangled polymer molecule, i.e., the time it takes for a molecule to wiggle its way out of its entanglements and take on a completely independent conformation [20]. The value of the reptation time τ_f for pure PEO shown in the inset of Fig. 5.3 is on the order of fraction of a second. This is a reasonable value for the reptation time of an entangled polymer melt and as such is expected to be the slowest relaxation time in the system. We observed much slower processes in our creep and recovery experiments, however. The time τ_1 is not observed in the pure polymer and will be discussed below. The relaxation time τ_2 is observed in both creep and recovery and is a few orders of magnitude higher than τ_f. We believe this timescale is related to the sample preparation method. In the sample preparation, melt-mixed PEO pellets were randomly distributed in the mold before compressing, as explained above. The polymers in these pellets may have a preferential alignment in some direction. This alignment in the pellets leads to the presence of domains with different mean polymer orientation in our nanocomposites, and this orientation persists in the melt. As a result of this, our samples have something like grain boundaries separating regions of different mean orientation. We suggest that τ_2 is a time scale for this grain boundary to relax due to diffusion of molecules across the boundary.

Both creep and recovery data of PEO showed a very slow evolution of the mechanical response which we represented by the linear *at* term in both Eq. 5.2 and 5.3. Figure 5.6 also shows a very slow evolution of the mechanical properties. We think this is also related to sample preparation. During compression molding, a large force is applied to the materials leading to large internal stress within the material. As a result of this and the flow that takes

place during molding, the polymer molecules are strongly aligned in configurations that are very far from their equilibrium configurations, and they do not have time to fully relax before the sample is cooled and solidified. The stresses are thus frozen into the sample. Complete relaxation of these stresses involves polymer motions over an entire domain, which is on the order of 1 mm in size. This gives a relaxation time many orders of magnitude longer than the single-molecule reptation time. This slow process indicates that our results are strongly affected by the sample preparation technique.

When MWCNT were added to the PEO, the crossover frequency from the frequency sweep experiments decreased and τ_f increased as the MWCNT inhibit the ability of the molecules to diffuse through the melt, increasing the time required to escape their entanglements. Also, the process characterized by τ_1 appeared in both creep and recovery data. τ_1 represents the relaxation of polymer chains whose motions are restricted by the presence of nanotubes. Interestingly, at p = 2 wt%, the crossover time τ_f and τ_1 become the same. In pure PEO and low MWCNT concentrated nanocomposites, τ_f is due to reptation in regions of the composites that consist of pure polymer, with no nanotubes nearby to affect the dynamics. When the concentration is high enough, all polymer molecules are close to, and affected by the MWCNT, resulting in τ_f and τ_1 becoming the same. The τ_2 process and the process explained by *at* term were also seen in the nanocomposites. The relaxation mechanisms described for both these processes involve polymer dynamics and are not strongly affected by the presence of MWCNT.

The addition of MWCNT to the polymer also affects the viscous and elastic moduli of the materials. MWCNT are comprised of rolled-up graphene sheets and have an elastic modulus in the TPa range [1], approaching that of graphene. Adding MWCNT to PEO leads to an increase in the elastic modulus of the resulting composites, as shown in Fig. 5.3.

G', G'', and η increase with concentration p, especially at low frequencies as shown in Fig. 5.5. Pötschke et al. [8] studied polycarbonate/MWCNT nanocomposites and reported the existence of a mechanical percolation threshold around 2 wt% at which the viscosity increases significantly. Our previous work in Chapter 4 showed that there is an electrical percolation

transition around 2 wt% in these PEO/MWCNT nanocomposites. Our data do not show any dramatic changes in mechanical properties in this concentration range, however.

The effect of MWCNT loading on creep is illustrated in Fig. 5.8. The experimental data were described well by the Burgers model. For pure PEO, M0.0, the creep compliance increases almost linearly with time, indicating predominantly viscous behavior with elastic effects being very small. For the PEO/MWCNT composites, we observed an initial rapid elastic response followed by slower viscous creep and a much smaller overall compliance. This also indicates that the MWCNT contribute strongly to the elastic behavior of the composite. Increasing MWCNT concentration increases the elastic modulus due to the presence of rigid MWCNT.

When MWCNT are added to PEO, the viscosity of the resulting nanocomposites increases, as shown in Fig. 5.5. This could be due to a decrease in free volume available to the polymer chains as a result of interactions between the polymer chains and the nanotubes, and the effect of CNT clusters restricting polymer flow [10]. The long-time viscosities obtained from fits of the creep data to Eq. 5.2 shown in Fig. 5.10 are much larger than those obtained from the frequency sweep experiments, which are shown in Fig. 5.5 at 1 rad/s. This is because the viscosity is strongly dependent on frequency, as shown in Fig. 5.4. This frequency dependence suggests that the frequency sweep experiment has not reached the terminal zone even for frequencies as low as 1 rad/s, indicating that there are very slow dynamics in these systems. This is confirmed by our creep and recovery data which show the very slow relaxations discussed above.

The effect of MWCNT on creep recovery is shown in Fig. 5.11. In this case, the experimental data were described well by the Weibull distribution, Eq. 5.3 with an added linear term. The nanocomposite samples exhibited much more strain recovery than the pure PEO, again because of the contributions of the MWCNT to the elasticity of the nanocomposites. In M5.0, strain recovered by approximately 90% in 900 s after removal of an applied stress of 55 Pa. Our results indicate that not only do the composites resist to higher stress, but recovery is also higher for higher concentrations of MWCNT because the elasticity is higher.

The frequency sweep experiment was able to determine the reptation time of entangled PEO molecules. The reptation time increases with increasing MWCNT concentration indicating that the nanotubes slow down the polymer dynamics. Creep and recovery identified very slow relaxation processes which are directly related to the sample preparation technique. Our results also suggested that these materials evolve over a long time as a consequence of the sample preparation technique. If one wants a material with stable mechanical properties, then they should allow these materials to release the internal stress resulting from in the sample preparation before using for an application.

5.5 Conclusion

We studied the mechanical properties of PEO-MWCNT nanocomposites made by melt mixing. The reptation time τ_f extracted from our frequency sweep data was a fraction of a second for pure PEO and increased with MWCNT loading. Creep and recovery experiments were able to detect slow mechanical relaxation processes that were not visible in the frequency sweep. Creep and recovery data were fitted to the Burgers model and the Weibull distribution, respectively, with an additional linear term to account for the very slow relaxation of stresses built into the samples by the sample preparation method. The two relaxation times found from the creep data were the same within experimental error as the relaxation times determined from the reovery data. $\tau_1 \approx \tau_{r1}$ was attributed to the relaxation time of PEO chains whose motion are restricted by MWCNT and $\tau_2 \approx \tau_{r2}$ was due to the diffusion of PEO polymer chains across the interfaces between pellets. A very slow sample evolution was also evident from creep and recovery. Both $\tau_2 \approx \tau_{r2}$ and the slow sample evolution were associated with the sample preparation technique.

Bibliography

[1] B.G. Demczyk, Y.M. Wang, J. Cumings, M. Hetman, W. Han, A. Zettl, and R. O. Ritchie. *Mater. Sci. Eng., A*, 334:173, 2002.

[2] E. Kymakis, I. Alexandou, and G. A. J. Amaratunga. *Synth. Met.*, 127:59, 2002.

[3] R. Haggenmueller, H. H. Gommans, A. G. Rinzler, J. E. Fischer, and K. I. Winey. *Chem. Phys. Lett.*, 330:219, 2000.

[4] G. S. Bocharov and A. V. Eletskii. *Int. J. Molec. Sci.*, 21:7634, 2020.

[5] J. N. Coleman, U. Khan, W. J. Blau, and Y. K. Gun'ko. *Carbon*, 44:1624, 2006.

[6] R. Krishnamoorti, I. Banik, and L. Xu. *Rev. Chem. Eng.*, 26:3, 2010.

[7] Y. Song and Q. Zheng. *J. Rheol.*, 59:155, 2015.

[8] P. Pötschke, T. D. Fornes, and D. R. Paul. *Polymer*, 43:3247, 2002.

[9] P. Ma, N. A. Siddiqui, G. Marom, and J. Kim. *Compos. A: Appl. Sci. Manuf.*, 41:1345, 2010.

[10] X. Wang, L. Gong, L. Tang, K. Peng, Y. Pei, L. Zhao, L. Wu, and J. Jiang. *Compos. - A: Appl. Sci. Manuf.*, 69:288, 2015.

[11] Q. Zhang and L. A. Archer. *Langmuir*, 18:10435, 2002.

[12] T. N. Abraham, D. Ratna, S. Siengchin, and J. Karger-Kocsis. *J. Appl. Polym. Sci.*, 110:2094, 2008.

[13] C. W. Macosko. *Rheology Principles, Measurements, and Applications*. Wiley-VCH, Inc., 1994.

[14] A.D. Drozdov, A.-L. Høg Lejre, and J. de C. Christiansen. *Compos. Sci. Technol.*, 69:2596, 2009.

[15] Z. Dai, Y. Gao, L. Liu, P. Pötschke, J. Yang, and Z. Zhang. *Polymer*, 54:3726, 2013.

[16] Y. Jia, K. Peng, X. Gong, and Z. Zhang. *Int. J. Plast.*, 27:1239, 2011.

[17] K. S. Fancey. *J. Mater. Sci.*, 40:4827, 2005.

[18] F. A. Morrison. *Understanding Rheology*. Oxford university press New York, 2001.

[19] J. D. Ferry. *Viscoelastic Properties of Polymers*. John Wiley & Sons, 1980.

[20] M. Rubinstein and R. H. Colby. *Polymer Physics*. Oxford University Press, 2003.

Chapter 6

Dielectric spectroscopy of polystyrene-carbon nanotube nanocomposites

6.1 Introduction

Polymer nanocomposites with carbon nanotube (CNT) fillers are novel materials. They are of great interest among researchers due to the ability to tune both electrical and mechanical properties of a polymer by adding a small amount of nanotubes [1, 2, 3, 4, 5]. High electrical conductivity [6], high length to diameter ratio (aspect ratio), Young's moduli as large as 0.9 TPa, and tensile strength as high as 0.15 TPa in multi-walled CNT (MWCNT) [7] are some of extraordinary properties carbon nanotubes possess.

Polystyrene (PS) is a widely available thermoplastic polymer with many applications related to daily life, such disposable cutlery and housing insulation [8]. In the present work, we study the dielectric properties of PS-MWCNT nanocomposites using a dielectric spectrometer. In previous work, PS/CNT nanocomposites were synthesized to use as electromagnetic interference (EMI) shielding [9, 10]. Several other potential applications of PS/CNT have been re-

ported in fields such as light weight energy storage, transducers and sensors, and high-strength, low-density corrosion-resistant components [11].

Electrical properties such as electrical conductivity and the percolation transition of polymer nanocomposites have been studied widely [12, 13, 14]. The electrical conductivity of an insulating polymer can be increased by several orders of magnitude by adding conductive fillers such as CNT, and the minimum filler concentration needed to achieve this dramatic change is known as the percolation threshold p_c [2]. The percolation threshold depends on several parameters such as the electrical conductivity of the filler, its aspect ratio, and the sample preparation technique, resulting in the wide range of p_c values that have been reported for PS/CNT nanocomposites [11].

In dielectric spectroscopy, the complex permittivity $\epsilon^* = \epsilon' - i\epsilon''$ is measured over a broad range of frequencies. Here ϵ' is the dielectric constant and $\epsilon'' = \sigma/\epsilon_0\omega$, where σ is the frequency-dependent electrical conductivity and ω is the angular frequency. The dielectric spectra of polymeric materials display very broad relaxation features. A variety of dielectric relaxation models have been used in their interpretation [15, 16, 17, 18]. In this work, we interpret the dielectric properties of PS-MWCNT nanocomposites by fitting the empirical Havriliak-Negami (HN) model [19] to the imaginary part of our experimental data. This model, which has been applied to polymeric materials by several groups [19, 20, 21, 22], models the complex permittivity ϵ^* as

$$\epsilon^* = \epsilon_\infty + \frac{\Delta\epsilon}{(1 + (i\omega\tau)^\alpha)^\beta} - i(\frac{\sigma_{dc}}{\epsilon_0\omega})^\gamma, \tag{6.1}$$

where ϵ_∞ and $\Delta\epsilon$ are the infinite-frequency dielectric constant and the dielectric strength, respectively. The second term on the right-hand side of Eq. (6.1) represents the contribution to ϵ^* due to a dielectric relaxation process. When the exponents α and β in Eq. (6.1) are all equal to 1, the relaxation term describes an exponential relaxation process with relaxation time τ. For non-exponential relaxation processes, α and β are different from 1, and τ can be regarded as a

characteristic relaxation time. The relaxation process is manifested as a peak in ϵ''. The last term of the equation represents the contribution of the conductivity σ_{dc} and the exponent γ is generally between 0 and 1. γ is equal to 1 if the low-frequency conductivity is constant, i.e., for the usual Ohmic conduction. $\gamma < 1$ indicates non-Ohmic behavior which could, for example, involve charge transport by hopping.

In this work, we report measurements of the real and imaginary parts of the permittivity of PS-MWCNT nanocomposites prepared by twin-screw extrusion. The experimental data were collected as functions of MWCNT concentration, temperature and thermal cycles. The measured imaginary part of the permittivity was interpreted using the HN model (Eq. 6.1) and parameters such as the relaxation time and electrical conductivity were extracted. Our results are discussed in terms of the microstructure of the nanocomposites and the microscopic interactions between the nanotubes and the polymer molecules.

6.2   Experiment

We dispersed multiwalled carbon nanotubes (MWCNT) in polystyrene (PS) using twin-screw compounding. PS pellets with molar mass of 35,000 g/mol were purchased from Sigma-Aldrich and used as received. MWCNT with diameter 8–15 nm and length 30–50 μm was purchased from TimeNano Chengdu Organic Chemicals and used without further purification. In the sample preparation, 4.5 g of PS and the required amount of MWCNT were mixed in a Thermo Scientific HAAKE MiniLab II twin-screw micro-compounder preheated to 125 °C. The components were mixed for 10 minutes with a screw speed of 50 rpm before extracting the compound from the mixer and cooling to room temperature. The extracted material was in the form of a long sheet, about 1 mm thick and 5 mm in width, which was pulverized by hand before compression molding.

Disks of the nanocomposites 25 mm in diameter and 1 mm thick were made by transferring the small pieces of PS/MWCNT prepared as above to a room temperature mold made from 3.2

mm thick aluminum plates, separated by a 1 mm thick aluminum gasket with three 25 mm diameter holes in it. The filled mold was heated to 125 °C for 5 min, then compressed under 13.3 kN of force for 5 min. Finally, the mold was cooled to room temperature and the disks were removed. We follow this recipe to make nanocomposites with MWCNT concentration ranging from 0 to 5% by weight. We labeled our samples as PS, representing polystyrene, followed by the amount of MWCNT added, given as a percentage of the total sample weight. For example, PS1.0 represents PS/MWCNT nanocomposites with 1.0 wt% MWCNT.

Scanning electron microscope (SEM) images of our nanocomposites were obtained using a high-resolution Zeiss 1540XB SEM with an acceleration voltage of 1.0 keV. The composites were quenched in liquid nitrogen and fractured. The newly-exposed cross-section was then coated with a conducting layer of osmium for imaging with the SEM.

The complex permittivity $\epsilon^* = \epsilon' - i\epsilon''$ of each nanocomposite was measured as a function of frequency and temperature T using a Solartron ModuLab Material Test System (MTS) dielectric spectrometer with a Janis Research STVP-200-XG cryostat for temperature variation. The 25 mm diameter PEO nanocomposite disks were placed between the 25 mm diameter electrodes of the dielectric spectrometer's solid-sample holder. A sinusoidal voltage of frequency $f = \omega/2\pi$ was applied across the sample holder, and the amplitude and phase of the resulting current were measured. Our measurements were conducted using a 2-wire measurement technique over the frequency range 0.1 Hz $\leq f \leq$ 0.1 MHz, using a sinusoidal excitation voltage of 4 V rms. A Lake Shore Model 335 Cryogenic Temperature Controller was used to control the temperature T of the sample with an accuracy of 0.01 K. Measurements were taken as a function of temperature in 10 K increments while heating from 300 K to 360 K, and then while cooling back to 300 K, again in 10 K steps. The temperature was cycled in this way four times for each sample. The samples were allowed to equilibrate at each temperature step for 20 minutes before the dielectric spectrum was measured.

6.3 Results

Figure 6.1 shows SEM images of PS0.5 and PS5.0 nanocomposites. Fig. 6.1(a) and (b) are SEM images of PS0.5 at two different magnifications. The distribution of the nanotubes in PS0.5 is not very uniform and several disconnected clusters of MWCNT can be seen in Fig.6.1(a). However the clusters themselves are reasonably evenly distributed throughout the sample, and they are approximately the same size. Fig. 6.1(b) shows an area of the same sample at higher magnification. Fig. 6.1(c) and (d) are the SEM images of PS5.0. There are clearly more nanotubes than in PS0.5. Fig. 6.1(c) shows a large range of cluster sizes distributed throughout the image. Fig. 6.1(d) shows an area of the same sample at higher magnification in which individual nanotubes and small clusters are visible.
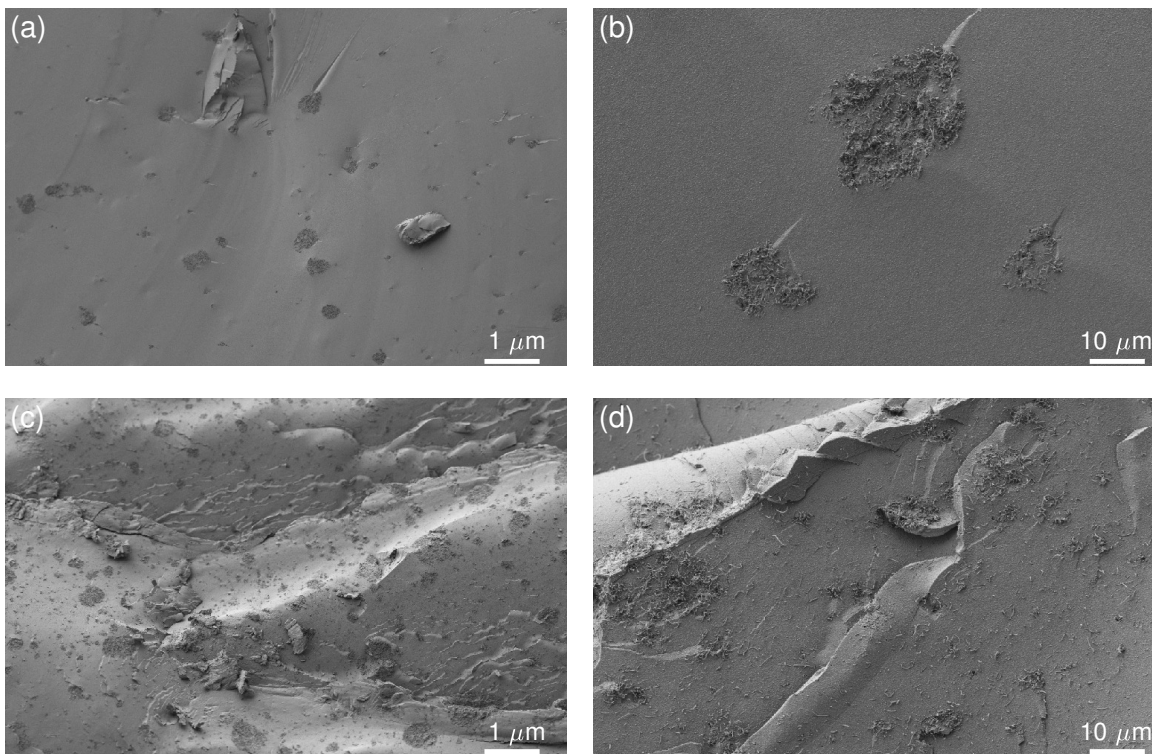
Figure 6.1: SEM images of PS-MWCNT nanocomposites (a) and (b) PS0.5 and (c) and (d) PS5.0. These images are discussed in more detail in the text.

The real and imaginary parts of the permittivity of the nanocomposites with MWCNT concentrations ranging from 0 to 5 wt% at 300 K in the heating phase of cycle 1 are illustrated
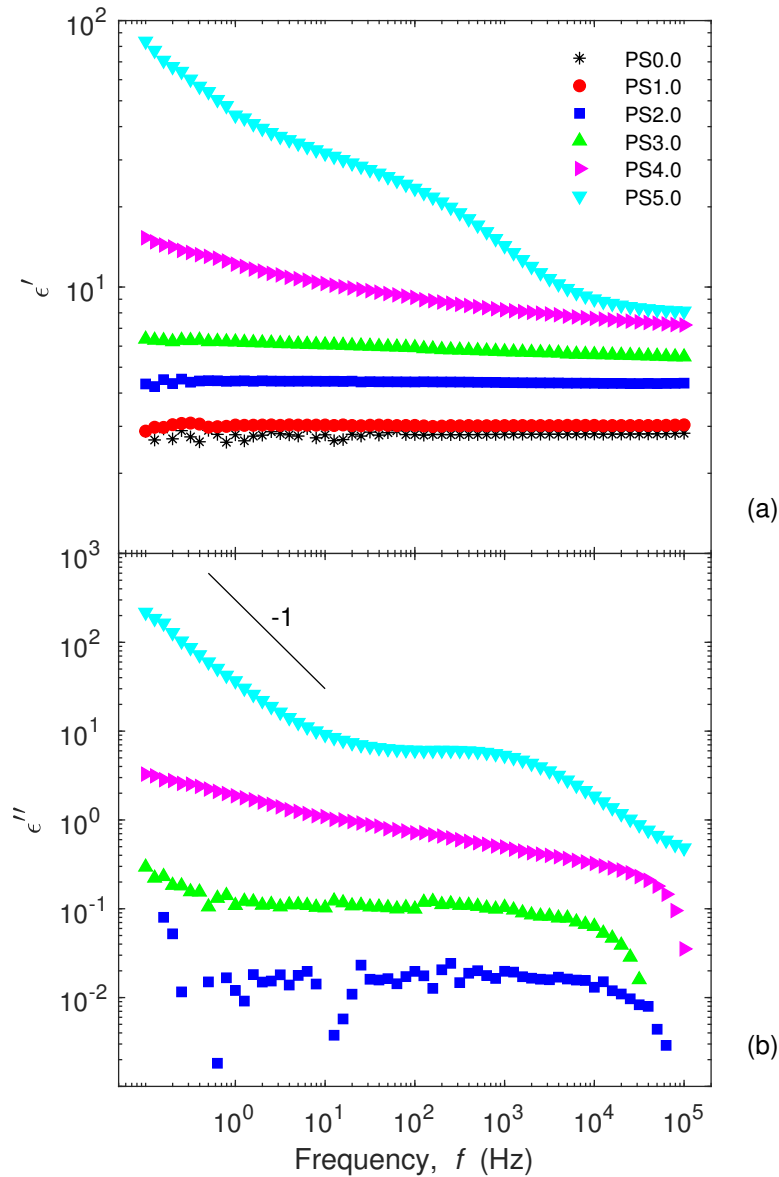
Figure 6.2: (a) Real (ϵ') and (b) imaginary (ϵ'') parts of the permittivity of PS/MWCNT nanocomposites at a temperature of 300 K during the heating phase of cycle 1. The different symbols indicate different MWCNT concentrations, as shown in the legend. The solid line in (b) has a logarithmic slope of -1 and is shown for comparison.

in Fig. 6.2. The dielectric constant of pure polystyrene (i.e., PS0.0) is about 3 due to its small dipole moment, and is independent of frequency. Adding 1.0 wt% of MWCNT results in little change in ϵ', but a strong effect is seen for higher MWCNT concentrations. A significant frequency dependence of the real part is observed at $p = 5$ wt% when ϵ' begins to change both qualitatively and quantitatively. At the highest MWCNT concentration measured at $p = 5$

wt%, ϵ' shows a weak step-like structure between 10^4 and 10^2 Hz and a continuous increase with decreasing frequency below 10^2 Hz.

The imaginary part of the permittivity is shown in Fig. 6.2 (b). ϵ'' of pure PS (not shown) was very small and could not be accurately measured due to the limited sensitivity of the dielectric spectrometer. ϵ'' was measurable for $p \geq 2.0$ wt% and was about 10^{-2} at $p = 2$ wt%. The imaginary part of the permittivity increases continuously with increasing p. At $p = 5.0$ wt% (sample PS5.0), ϵ'' shows more interesting features than the other nanocomposites. Similarly to the real part, the characteristics of ϵ'' also change significantly at $p = 5$ wt%. The broad peak in ϵ'' centered around 1 kHz in the data for PS5.0 indicates a dielectric relaxation process with a characteristic relaxation time on the order of 1 ms. The imaginary part of PS5.0 at $f < 10$ Hz follows a $1/f^\gamma$ behavior, implying that the electrical conductivity $\sigma(\omega) = \epsilon'' \epsilon_0 \omega$ is frequency-dependent at low frequencies. Overall, the dielectric constant at 1 Hz changes from around 3 to 40 and the imaginary part increases by about four orders of magnitude as p is increased from 0.0 to 5.0 wt%.

The real and imaginary parts of the permittivity at 1 kHz are plotted as a function of temperature during the heating phase of cycle 1 at different MWCNT concentrations in Fig. 6.3. Both ϵ' and ϵ'' show negligible dependence on temperature for $p \leq 4$. At $p = 5.0$ wt%, both the real and imaginary parts increase dramatically when T increases from 330 and 340 K. Consistent with what was seen in Fig. 6.2, both ϵ' and ϵ'' increase with p.

None of the data for $p \leq 4$ wt% showed a significant change with temperature, nor at a given temperature as a function of thermal cycling. However, both the real and imaginary parts of PS5.0 show significant changes as a function of temperate and thermal cycles. We will discuss the behaviour of ϵ'' in detail below.

To illustrate the change in permittivity of PS5.0 due to thermal cycling, ϵ' at 10 kHz is shown as a function of temperature over three thermal cycles in Fig. 6.4. In the heating phase of cycle 1, ϵ' stays around 10 as the temperature increases from 300 to 330 K and then increases abruptly by an order of magnitude between 330 and 340 K. On cooling, ϵ' increases from
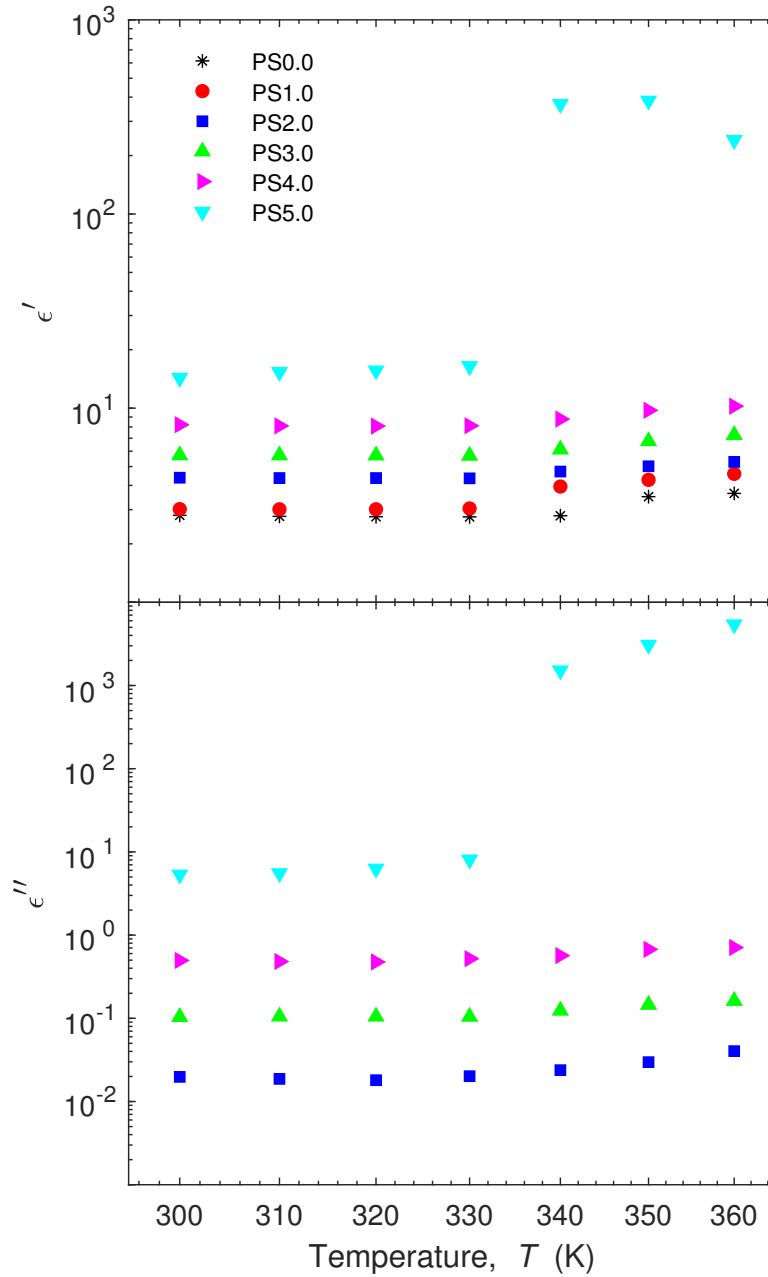
Figure 6.3: (a) Real (ϵ') and (b) imaginary (ϵ'') parts of the permittivity of PS/MWCNT nanocomposites at $f = 1$ kHz as a function of T during the heating phase of cycle 1. The different symbols represent different MWCNT concentrations.

about 150 at 360 K to 350 at 300 K. The jump between 330 and 340 K in the heating phase is weakened in the later cycles. At 300 K, the real part of the permittivity is always higher in the cooling phase at the end of the thermal cycle than in the immediately preceding heating phase.

The dielectric spectra of the nanocomposites were analyzed in detail by fitting the imagi-
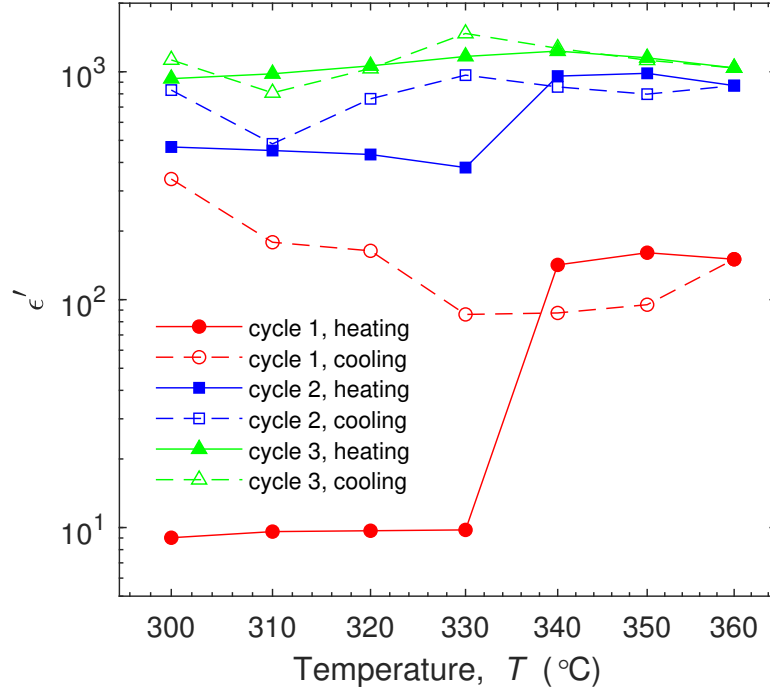
Figure 6.4: ϵ', the real part of the permittivity of PS5.0, at $f = 10$ kHz as a function of T over three themal cycles. Solid and open symbols show data recorded during heating and cooling, respectively. The solid and dashed lines are guides to the eye.

nary part of the permittivity to the HN model, Eq. 6.1. Samples with MWCNT $p < 5$ wt% did not show either a peak in ϵ'' nor follow $1/f^\gamma$ behavior for the entire frequency range studied. However, we were able to fit the data for $f < 100$ Hz for the $p = 3$ and 4 wt% samples to the last term of the HN model. The other samples ($p < 3$ wt%) did not show this power law behavior even below 100 Hz. Therefore, those data were not further analyzed. The PS5.0 data show a peak in ϵ'' at some temperatures and follow a power law with f at low frequencies. Therefore, their data were analyzed in detail as follows. Since the shape of $\epsilon''(f)$ depends strongly on temperature, we used the full HN model for any PS5.0 data displaying a peak in ϵ'', but only the last term of Eq. 6.1 for data that show only a power low dependence on frequency over the entire experimental frequency range. The parameters obtained from fits to the data for PS5.0 at different temperatures during the heating phase of cycle 1 are presented in Table. 6.1.

The effect of temperature on ϵ'' for PS5.0 in the heating phase of cycle 1 is shown in Fig. 6.5. The dashed lines in this figure are the fits to the model as explained above. Up to 330

111

Table 6.1: Optimum fit parameters from fits of the HN model (Eq. 6.1) to the ϵ'' data for sample PS5.0 during the heating phase of cycle 1. Uncertainties in the parameters are given in parentheses.

T (K)	$\Delta\epsilon$	$\tau(10^{-4}$ s)	α	β	$\sigma_{dc}(10^{-5}$ S/m)	γ
300	24.9 (0.7)	2.5 (0.4)	0.46 (0.02)	1.5 (0.1)	1.32 (0.02)×10⁻⁴	0.77 (0.01)
310	38 (1)	0.9 (0.3)	0.36 (0.01)	2.3 (0.2)	7.19 (0.08)×10⁻⁵	0.80 (0.01)
320	36.5 (0.7)	2.8 (0.3)	0.44 (0.01)	1.76 (0.08)	1.67 (0.01)×10⁻⁴	0.775 (0.005)
330	38 (1)	3.0 (0.2)	0.53 (0.02)	1.58 (0.08)	9.82 (0.07)×10⁻⁴	0.820 (0.003)
340					3.7 (0.1)	0.895 (0.004)
350					12.4 (0.3)	0.949 (0.003)
360					23.9 (0.3)	0.968 (0.002)

K, ϵ'' does not change much with increasing temperature and shows a broad peak at around 1 kHz, as seen in Fig 6.2. The position of the peak is almost independent of temperature. When temperature increases from 330 to 340 K, ϵ'' shows an increase of two orders of magnitude at high frequency and four orders of magnitude at low frequencies.

Furthermore, ϵ'' closely follows a $1/f$ dependence, indicating that the electrical conductivity $\sigma = \omega\epsilon_o\epsilon''$ is constant over the experimental frequency range for $T > 330$ K. We see a peak in ϵ'' for $T < 340$ K. This peak is no longer visible at higher temperatures, however, presumably because it is masked by the high conductivity of the PS5.0 nanocomposite. Upon cooling (data not shown), ϵ'' follows a $1/f$ dependence, even below 330 K.

The variation of the dielectric relaxation time τ with temperature T during the heating phase of cycle 1 for PS5.0 is shown in the inset of Fig. 6.5. τ is on the order of 10^{-4} s and is almost independent of temperature.

The variation of ϵ'' for PS5.0 with frequency and number of thermal cycles at 300 (solid symbols) and 360 K (open symbols) during the heating phase of the first three thermal cycles is shown in Fig. 6.6. The imaginary part of the permittivity shows a peak at 300 K in cycle 1 that is masked by the high dc conductivity of PS5.0 for subsequent cycles, as also seen in Fig. 6.5. This peak was observed at low temperatures in the heating phase of cycle 1 but did not reappear in any further thermal cycles, even in the cooling phase of cycle 1 (not shown here). ϵ'' continuously increases with the number of thermal cycles at both temperatures, with the
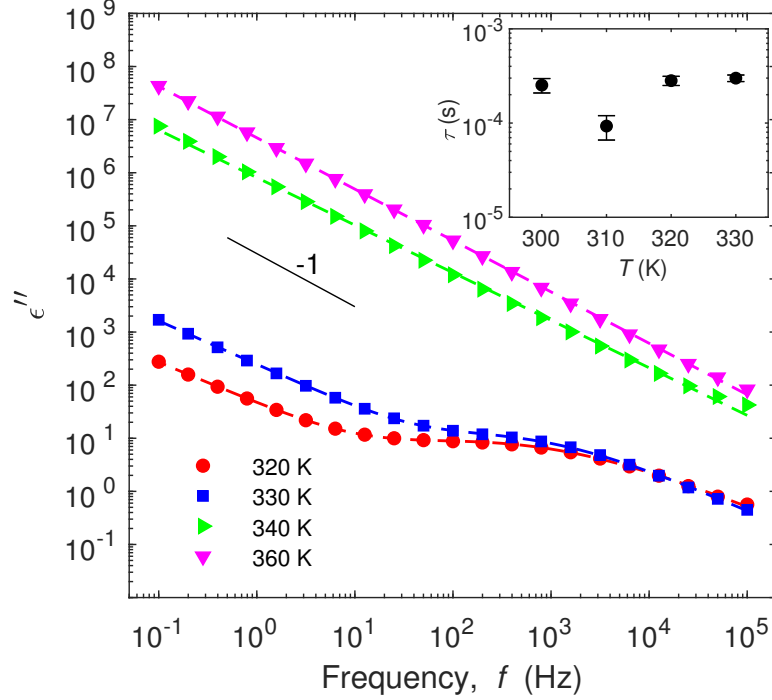
Figure 6.5: Fits of the HN model, Eq. (6.1), to ϵ'' for PS5.0 nanocomposites at different temperatures during the heating phase of thermal cycle 1. The symbols represent the experimental data and the dashed lines are the fits to Eq. 6.1.

most significant increase in the first cycle.

The last term on the right-hand side of Eq. (6.1) represents the contribution to the permittivity due to the conductivity of the material. This contribution is responsible for the low-frequency $\approx 1/f$ behavior of ϵ'' for PS5.0 seen in Figs. 6.5 and 6.6. Figure 6.7 (a) shows σ_{dc} for PS5.0 obtained from fits to Eq. 6.1 as a function of temperature and thermal cycles. σ_{dc} was around 10^{-8} S/m at temperatures below 330 K in the first thermal cycle and then increases more than four orders of magnitude when heating from 330 to 340 K, indicating an electrical percolation transition. σ_{dc} increases with further heating, reaching 10^{-4} S/m at 360 K. In the cooling phase of cycle 1, σ_{dc} (not shown) stays between 10^{-4} and 10^{-3} S/m. The dc conductivity of PS5.0 did not increase as dramatically in later cycles.

The exponent γ of Eq. 6.1 is plotted as a function of temperature and thermal cycles in Fig. 6.7(b). The exponent is around 0.8 at 300 K and increases with temperature in the heating phase of the first thermal cycle, reaching 1 at 360 K. γ stays approximately 1 in the cooling
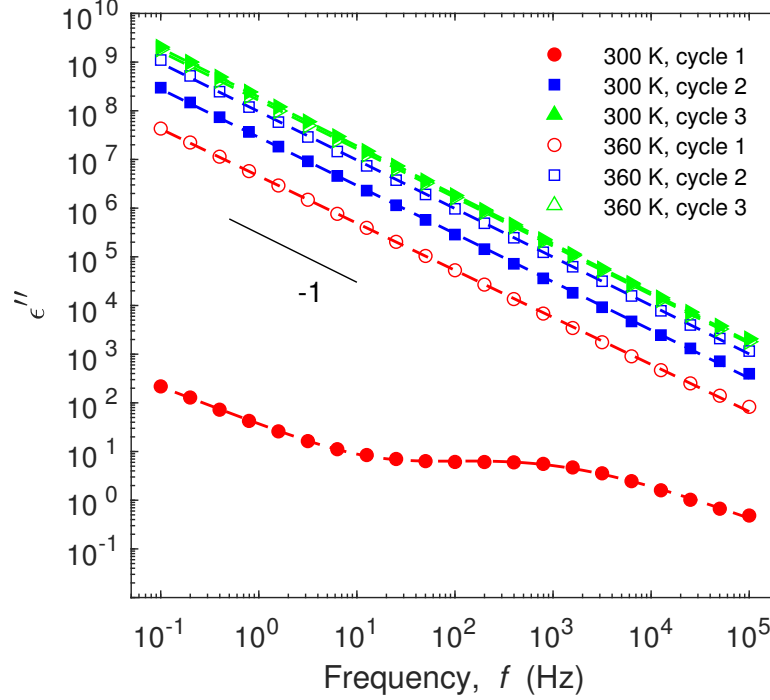
Figure 6.6: The imaginary part of permittivity versus frequency for PS5.0 at 300 (solid symbols) and 360 K (open symbols) in the heating phase of different thermal cycles. The symbols represent the experimental data and the dashed lines are the fits to Eq. (6.1) as described above.

phase of cycle 1 (not shown) and at all temperatures in the further heating or cooling phases. γ was less than 0.1 and 0.2 for $p = 3$ and $p = 4$ wt%, respectively, and did not change much with either temperature or thermal cycling.

6.4 Discussion

We studied the dielectric behavior of PS/MWCNT nanocomposites using a dielectric spectrometer. As seen in Fig. 6.2, both the real and imaginary parts of the permittivity of the nanocomposites increase with MWCNT concentration p. The MWCNT contribute to ϵ' due to the polarization of the graphene layers that make up the nanotubes [23]. In addition, MWCNT can form nanocapacitor structures consisting of thin polymer layers between nanotubes [12], which would also increase the real part of the permittivity. Both of these effects will become stronger with increasing MWCNT concentration, leading to an increase in ϵ' with p. The high
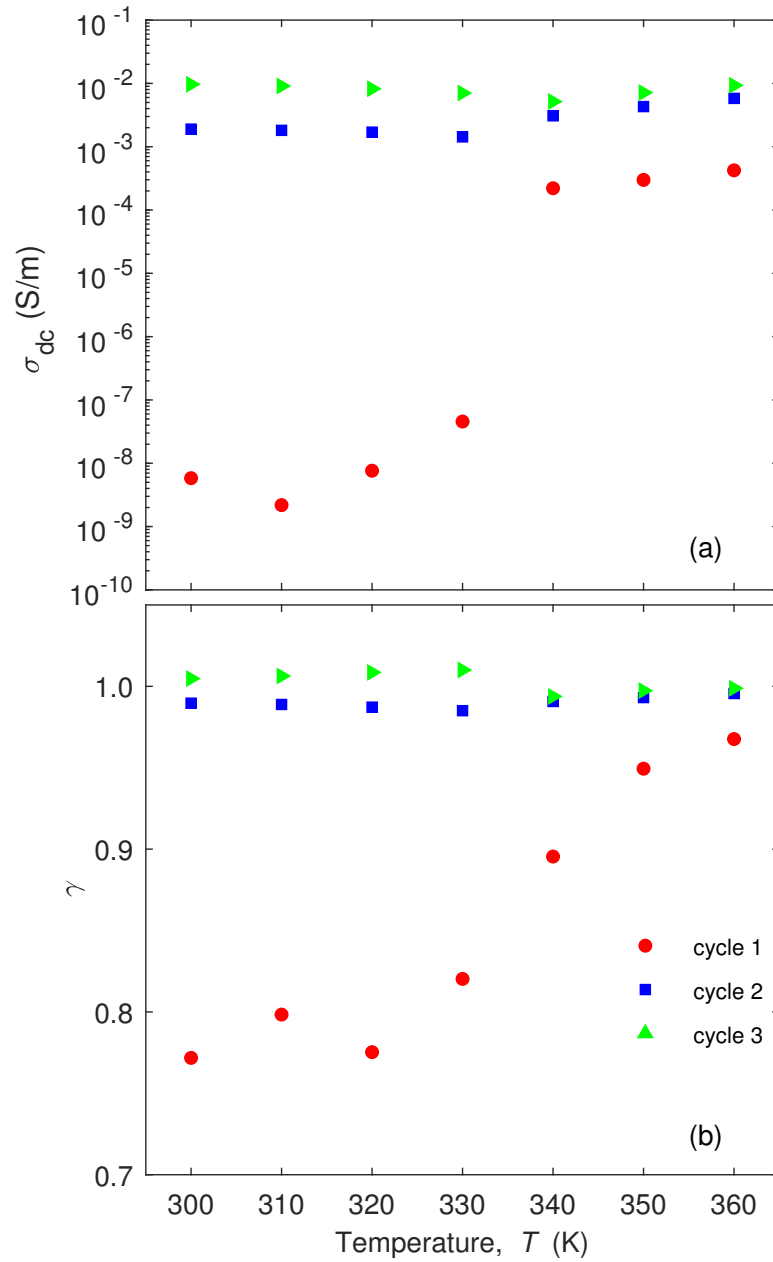
Figure 6.7: (a) The electrical conductivity and (b) the exponent of the last term of Eq. 6.1 for PS5.0 as a function of temperature in the heating phase of different thermal cycles shown in the legend. The uncertainties given by the fits are within the symbols.

electrical conductivity of MWCNT leads to an increase in ϵ'' with increasing p.
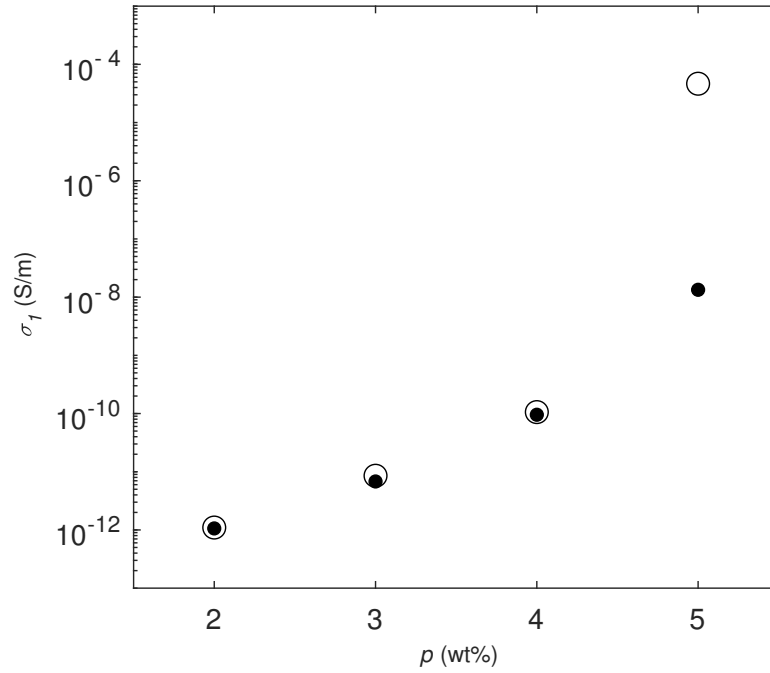
Figure 6.8: The frequency-dependent electrical conductivity $\sigma_1 = \omega\epsilon''\epsilon_0$ at 1 Hz as a function of MWCNT concentration. Solid symbols and the open symbol show σ_1 at 330 and 340 K, respectively, in the heating phase of the first thermal cycle.

If low-frequency electrical conductivity $\sigma_\omega = \omega\epsilon''\epsilon_0$ is a constant σ_{dc} then we would expect ϵ'' to behave as $1/f$ (i.e., $\gamma = 1$). γ was well below 1 for nanocomposites with $p = 3$ and 4 wt%. Also, the HN model was unable to successfully fit the dielectric data for $p < 3$ wt%. Therefore, there was no way to estimate σ_{dc} by fits to HN model for the nanocomposites with MWCNT concentration below 4 wt%. Therefore, we use the frequency-dependent conductivity $\sigma_1 = \omega\epsilon''\epsilon_0$ at 1 Hz shown in Fig. 6.8 to describe their electrical conductivity. Our data in Fig. 6.8 show that the electrical conductivity increases from 10^{-12} to 10^{-10} S/m as p increases from 2 to 4 wt%. For comparison, Arjmand et al. [12] reported the conductivity of pure PS is to be around 10^{-13} S/m. The electrical conductivity of PS5.0 is around 10^{-8} S/m at 330 K in the heating phase of the first cycle and increases by three orders of magnitude when heating from 330 to 340 K. This jump is also visible in σ_{dc} in Fig. 6.7. This increase in σ_1 implies the formation of a sample-spanning percolation network of highly conductive nanotubes at a percolation transition somewhere between 4 and 5 wt% of MWCNT. For comparison, the

conductivity is on the order of 10^{-10} S/m for PS4.0 at 340 K and is on the order of 10^{-5} S/m for PS5.0 at 340 K.

The percolation concentration p_c of PS/MWCNT nanocomposites made by twin-screw extrusion depends on the screw speed and mixing time. The effect of the screw speed on p_c was reported in the work of McClory et al. [24], who found that p_c was between 1 and 3 wt% at 20, 70, and 100 rpm. We used a screw speed of 50 rpm and 10 min mixing time in the sample preparation and found p_c to be between 4 and 5 wt%. The difference in p_c could be due to using different mixing times but, unfortunately, their mixing time wasn't reported. p_c can be different in the same nanocomposites made by using different sample preparation methods. It was reported that p_c was as little as 0.06 wt% for solution-mixed PS/MWCNT nanocomposites. This low threshold was attributed to good dispersion and distribution of the MWCNT in the polystyrene [12]. In our previous work presented in Chapter 4, we prepared poly(ethylene oxide)/MWCNT by melt-mixing and twin-screw extrusion with the same rpm and mixing time and found that p_c = 0.68 and 1.22 wt%, respectively. This suggests that the nanotubes are not as well dispersed in PS materials as in the PEO. This is consistent with the appearance of the SEM images shown in Fig. 6.1.

The last term of Eq. 6.1 represents a contribution to ϵ'' that is proportional to $f^{-\gamma}$. γ is typically between 0 and 1 and depends on the charge transport mechanism within the material. $\gamma = 1$ results from an Ohmic contribution to the conductivity, while $\gamma < 1$ indicates a non-Ohmic conduction mechanism [20, 22]. For all samples with $p < 5$ wt%, γ was much less than 1. For $p = 5$ wt%, γ was 0.77 at 300 K, reached approximately 1 at 360 K during the heating phase of the first thermal cycle, and stayed at close to 1 through all subsequent thermal cycles. This suggests that the electrical conduction process in PS5.0 changes from non-Ohmic to Ohmic during the initial heating, then remains Ohmic through subsequent cycles. In the non-Ohmic state, both conduction along carbon nanotubes and hopping across a thin layer of polymer between adjacent nanotubes contribute to charge transport. In the Ohmic state, conduction along the nanotubes is the main charge transport mechanism.

The change in the charge transport mechanism of PS5.0 can be understood as follows. There are many clusters of nanotubes in the polymer matrix as shown in Fig. 6.1(c). We suggest that, when the nanocomposites are initially prepared, the clusters are separated by thin layers of insulating polymer. These layers prevent electrical conduction between the clusters. Charge transport across these thin layers occurs by a hopping mechanism, resulting in a non-Ohmic material and low electrical conductivity. As the material is heated towards its glass transition, which is approximately 400 K [25], the PS in these thin insulating layers softens enough that the attractive van der Waals interaction between the carbon nanotubes can pull the nanotube clusters into contact. This creates a percolating conductive network, allowing Ohmic conduction across the sample. σ_{dc} increased with further thermal cycles as the network gets stronger. We did not observe this behaviour in our PS nanocomposites with lower p as their MWCNT concentrations were lower than the percolation concentration.

A peak in ϵ'' indicates a dielectric relaxation process. We did not observe any peaks for nanocomposites with $p \leq 4$ wt%. A clear peak was only observed for PS5.0 at temperatures below 340 K, and only in the heating phase of the first thermal cycle. The corresponding relaxation time τ, shown in the inset of Fig. 6.5 is on the order of 10^{-4} s. In all our experiments, the nanocomposites were below the glass transition temperature of PS, which is approximately 400 K [25]. Because of this, the observed relaxation cannot be due to the motion of full PS chains, as they are immobile at these temperatures. This relaxation cannot be due to a process involving charges on the nanotubes either, as no other nanocomposites showed this relaxation peak. We suggest that this relaxation is due to the motion of small, mobile segments of PS chains resulting from interactions with the nanotubes. The polymer chains can bind to the carbon nanotubes, leaving small segments of polymer between the bonds. We suppose that the average length of these chain segments decreases with increasing MWCNT concentration and that the chain segments below a certain length and close to the nanotubes are mobile even below the bulk glass transition. Our data suggest that in PS5.0 these chain segments are small enough and mobile enough to respond to the applied electric field in the frequency range we studied,

even at temperatures below the glass transition. Our previous work on PEO nanocomposites, presented in Chapter 4, showed a similar relaxation process at temperatures below the glass transition temperature of the polymer. The relaxation process we observe in PS 5.0 becomes hidden by the high electrical conductivity of the nanocomposite above 330 K in the heating phase of the first thermal cycle and at any temperature in further thermal cycles. We only observed this dielectric relaxation process in PS5.0 and further work involving nanocomposites with higher MWCNT concentration is required to allow a more complete understanding of the dielectric response of these nanocomposites.

6.5   Conclusion

We studied the complex permittivity of PS/MWCNT nanocomposites made by twin-screw extrusion. Both the real and imaginary parts of the permittivity increased with increasing nanotube concentration. The dielectric spectrum of PS5.0 showed more features in ϵ'' than seen in pure PS and nanocomposites with lower nanotube concentration. The dramatic change in conductivity of PS5.0 indicates the existence of a percolation transition at MWCNT concentration between 4 and 5 wt%. Conduction in PS5.0 was non-Ohmic initially, but became Ohmic after the material was heated above 330 K. In the non-Ohmic state, both conduction and hopping across a thin layer of polymer between two nanotubes or clusters contribute the electric current. Conduction along the nanotubes is the main charge transport mechanism in the Ohmic region. The dielectric relaxation process observed in PS5.0 is due to the relaxation of small segments of polymer chains, the ends of which are bound to the nanotubes. The dielectric peak observed in PS5.0 was hidden due to the high electrical conductivity of the nanocomposite after the material was heated above 330K and it did not reappear even after cooling back to 300 K again.

Bibliography

[1] J. P. Runt and J. J. Fitzgerald. *Dielectric Spectroscopy of Polymeric Materials*. American Chemical Society, 1997.

[2] P. Pötschke, S. M. Dudkin, and I. Alig. *Polymer*, 44:5023, 2003.

[3] R. Haggenmueller, H. H. Gommans, A. G. Rinzler, J. E. Fischer, and K. I. Winey. *Chem. Phys. Lett.*, 330:219, 2000.

[4] P. Ma, N. A. Siddiqui, G. Marom, and J. Kim. *Compos. A: Appl. Sci. Manuf.*, 41:1345, 2010.

[5] E. Kymakis, I. Alexandou, and G. A. J. Amaratunga. *Synth. Met.*, 127:59, 2002.

[6] A. B. Kaiser, G. Düsberg, and S. Roth. *Phys. Rev. B*, 3:1418, 1998.

[7] B.G. Demczyk, Y.M. Wang, J. Cumings, M. Hetman, W. Han, A. Zettl, and R. O. Ritchie. *Mater. Sci. Eng., A*, 334:173, 2002.

[8] J. Scheirs and D. Priddy. *Modern Styrenic Polymers: polystyrenes and Styrenic Copolymers*. John Wiley & Sons, 2003.

[9] V. K. Sachdev, S. Bhattacharya, K. Patel, S. K. Sharma, N. C. Mehra, and R. P. Tandon. *J. Appl. Polym. Sci.*, 131:24, 2014.

[10] Y. Yang, M. Gupta, K. L. Dudley, and R. W. Lawrence. *Nano Lett.*, 5:2131, 2005.

[11] M. Kaseem, K. Hamad, and Y. G. Ko. *Eur. Polym. J.*, 79:36, 2016.

[12] M. Arjmand and U. Sundararaj. *Polym. Eng. Sci.*, 55:173, 2015.

[13] G. S. Bocharov and A. V. Eletskii. *Int. J. Molec. Sci.*, 21:7634, 2020.

[14] W. Bauhofer and J. Z. Kovacs. *Compos. Sci. Tech.*, 69:1486, 2009.

[15] P. Debye. *Phys. Z.*, 13:97, 1912.

[16] K.S. Cole and R.H. Cole. *J. Chem. Phys.*, 9:341, 1941.

[17] S. Havriliak and S. Negami. *Polymer*, 8:161, 1967.

[18] T. Blythe and D. Bloor. *Electrical Properties of Polymers*. Cambridge University Press, 2005.

[19] M. Eesaee, E. David, and N. R. Demarquette. *Polym. Eng. Sci.*, 60:968, 2020.

[20] M. Füllbran, P. J. Purv, and A. Schönhal. *Macromol.*, 46:4626, 2020.

[21] B. Carroll, S. Cheng, and A. P. Sokolov. *Macromol.*, 50:6149, 2017.

[22] F. Kremer and A. Schönhals. *Broadband Dielectric Spectroscop*. Springer, 2003.

[23] B. Kozinski and N. Marzari. *Phys. Rev. Lett.*, 96:166801, 2006.

[24] C. McClory, P. Pötschke, and T. McNally. *Macromol. Mater. Eng.*, 296:59, 2011.

[25] https://www.sigmaaldrich.com/CA/en/product/aldrich/331651. last accessed on April 15, 2022.

Chapter 7

Conclusions and Future Work

The goals of this study were to explore the electrical and mechanical properties of polymer nanocomposites, and in particular, the effects of carbon nanotubes on those properties. One of our main interests was to understand polymer dynamics at various length scales in the presence of carbon nanotubes.

In this thesis, we have presented measurements of the electrical and mechanical properties of polymer nanocomposites produced by adding multiwalled carbon nanotubes (MWCNT) into poly(ethylene oxide) (PEO) and polystyrene (PS). We used a dielectric spectrometer to study the permittivity and electrical conductivity of these nanocomposites and studied their mechanical properties by collecting data with a rotational shear rheometer. We presented the electrical properties of PEO/MWCNT and PS/MWCNT nanocomposites in Chapters 4 and 6, respectively. Chapter 5 examined the mechanical properties of PEO/MWCNT nanocomposites.

Our dielectric data for PEO/MWCNT showed that both the real, ϵ', and imaginary, ϵ'', parts of the permittivity increased with increasing MWCNT concentration. In Chap. 4, we prepared PEO/MWCNT nanocomposites using two different techniques: melt mixing and twin-screw extrusion. The DC conductivities σ_{dc} of the resulting materials were directly measured using the dielectric spectrometer and were also obtained by fitting the imaginary part of the permittivity to the empirical Havriliak-Negami model. The DC conductivities obtained from the

two methods agree very well. The DC conductivity data shows a percolation transition for the PEO/MWCNT composites at $p_c = 1.23 \pm 0.01$ wt% and $p_c = 0.65 \pm 0.05$ wt% for the twin-screw extruded and the melt-mixed nanocomposites, respectively. For both mixing methods, the electrical conductivity of these nanocomposites increased by a factor of approximately 10^8 as the nanotube loading was increased from 0 to 5 wt%, with $\sigma_{dc} \approx 10^{-2}$ S/m at 300 K for 5 wt% NWCNT. The temperature dependence of the dc conductivity of PEO/MWCNT was studied in the temperature range from 180 to 300 K and was found to be well-described by a thermally-activated (Arrhenius) model, with a concentration-dependent activation energy of a few tenths of an eV, comparable to that of common semiconductors.

Our results for PS/MWCNT in Chapter 6 also showed that both ϵ' and ϵ'' increased with increasing MWCNT concentration. However, the electrical conductivity of PS/MWCNT pre-pared using twin-screw extrusion did not change significantly up to 4 wt% MWCNT. We were unable to determine a well-defined p_c for this material, but estimate it to be between 4 and 5 wt% MWCNT. The electrical conductivity for 5 wt% carbon nanotubes in PS/MWCNT was about 10^{-2} S/m at 300 K, which is the same as in the PEO/MWCNT nanocomposites at $p = 5$ wt%.

We used the frequency dependence of our dielectric data to identify relaxation processes in the nanocomposites. In Chap. 4, we presented evidence for the existence of two relaxation processes in PEO/MWCNT nanocomposites made by both mixing methods, corresponding to different peaks in ε''. One relaxation peak was observed at low MWCNT concentrations (below 1.5 wt%) and had a relaxation time that depended strongly on temperature. We attribute this relaxation to the motion of full polymer chains. Another, higher-frequency relaxation process was observed at higher MWCNT concentration and was very weakly dependent on temperature. We hypothesize that this fast relaxation is due to the motion of shorter chain segments, the ends of which are bound to the nanotubes. Interestingly, we did not observe a dielectric relaxation in PS/MWCNT composites for $p \leq 4$ wt%. A relaxation peak for $p = 5$ wt% was visible only while heating the sample from 300 to 330 K during the first thermal

cycle, and was hidden thereafter due to the high conductivity of the composite. This relaxation process is similar to the relaxation process observed at high frequencies in PEO/MWCNT and is attributed to the motion of shorter PS polymer chain segments bound to carbon nanotubes.

In Chap. 5, we presented the mechanical properties of PEO/MWCNT nanocomposites prepared by melt mixing. The reptation time τ_f extracted from our frequency sweep data using a rotational shear rheometer was 0.15 ± 0.01 s for pure PEO and increased with MWCNT loading. Creep and recovery experiments using a constant stress revealed the existence of two relaxation times τ_1 and τ_2. τ_1 did not exist in pure PEO and was several seconds for $p = 1$ wt%. τ_1 and τ_f were the same at $p = 2$ wt%. τ_1 was attributed to the relaxation time of PEO chains whose motion is restricted by the MWCNT. At nanotube concentrations above 2 wt%, the motion of nearly all chains was restricted. τ_2 is a few orders of magnitude higher than τ_f. We attribute τ_2 to the diffusion of PEO polymer chains across the interfaces between pellets that were compressed and melted to form the sample.

The relaxation processes observed in the dielectric data were fast compared to those in the mechanical data. Altogether, we observed relaxation mechanisms spanning a range from microseconds to hundreds of seconds covering very fast and very slow dynamics. The repation time τ_f involves the dynamics of full polymer molecules and did not change much at low MWCNT concentration as full chain dynamics are unaffected by the nanotubes. As MWCNT concentration is increased, the polymer dynamics become restricted, resulting in an increase in repation time. Similar to this, the dielectric relaxation of full polymer chains did not change significantly at low nanotube concentrations. A fast relaxation process appeared at high MWCNT concentration as a result of the relaxation of short segments of polymer chain, with the ends of the segments bound to the surface of the nanotubes. These results helped us to understand polymer dynamics at different length scales.

Future work in this area could focus on exploring these polymer nanocomposites with different parameters. We prepared all the nanocomposites with a mixing speed of 50 rpm and a fixed mixing time as explained Chap. 3. One could study how the mixing speed and mixing

time affect both the electrical and mechanical properties of these nanocomposites. This could indicate whether the dispersion of MWCNT in PEO and PS can be improved by changing these two parameters, thereby changing the percolation threshold p_c discussed in Chap. 4. More conductivity data are needed with MWCNT concentrations between 4 and 5 wt% and higher than 5 wt% to accurately determine the percolation threshold in PS/MWCNT nanocomposites. One could explore other sample preparation methods to find a way to better disperse the CNT in the PS.

In Chap. 5, we observed a slowly varying strain in both creep and creep recovery experiments and suggested that this was the result of residual stresses in the sample due to the sample preparation process. It would be interesting to further study the effect of the residual stress on the creep and creep recovery by changing the compression force, time, and temperature. It would be also interesting to study the polymer dynamics using different types of filler particles such as spherical conducting particles like metal nanospheres. Some of our dielectric data imply the existence of a relaxation peak at frequencies higher than 1 MHz. Therefore, higher frequency dielectric measurements would be interesting to probe the dynamics that lead to this relaxation peak.

Appendix A

Additional measurements and Analysis of PEO/MWCNT nanocomposites

In this Appendix we present additional data not presented in Chapter 4.
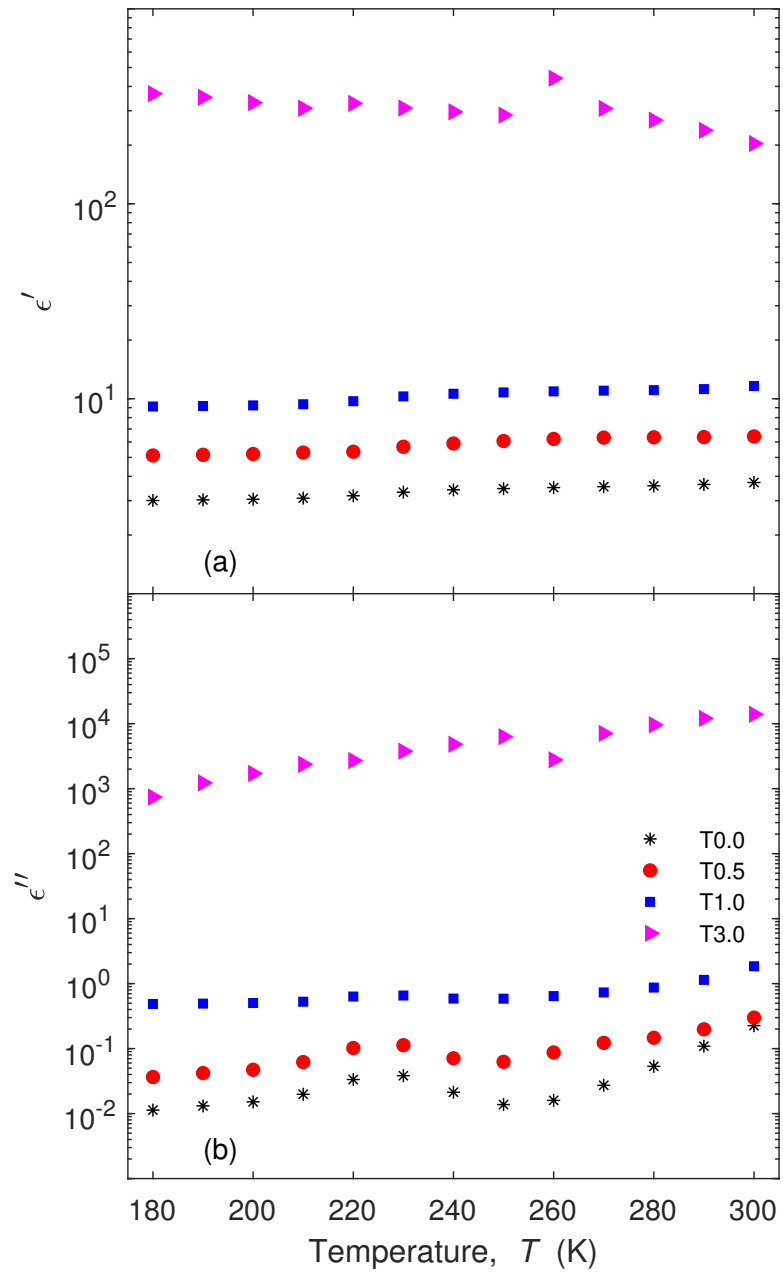
Figure A.1: (a) Real (ϵ') and (b) imaginary (ϵ'') parts of the permittivity of twin–screw extruded PEO nanocomposites at $f = 1$ kHz as a function of T. The different symbols represent different MWCNT concentrations.
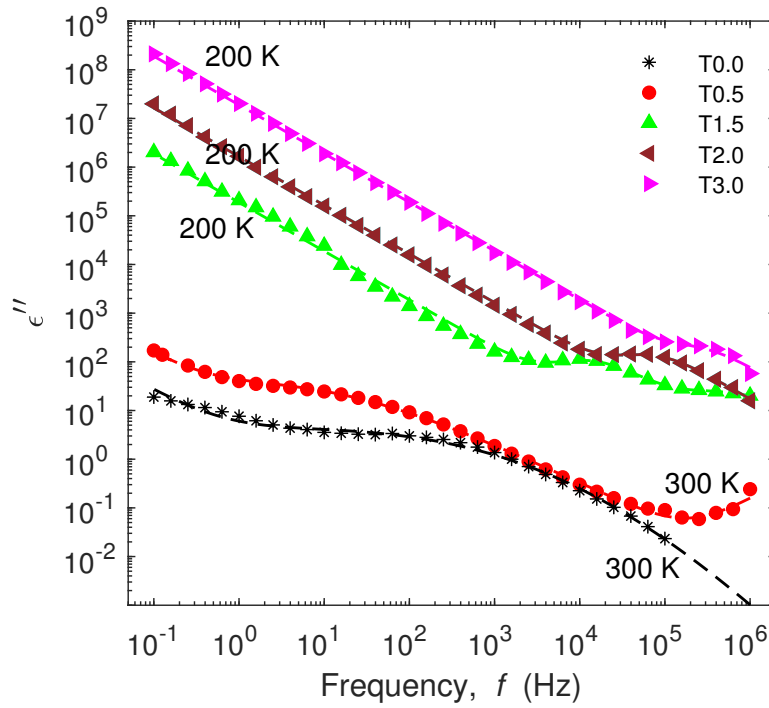
Figure A.2: Fits of the HN model, Eq. (3), to ϵ'' for twin–screw extruded PEO nanocomposites at a few different temperatures and MWCNT concentrations, illustrating the range of behavior observed. b symbols represent the experimental data and the dashed lines are the fits. One relaxation term was used for samples T0.0, T2.0 and T3.0, and two were used for T0.5 and T1.5.
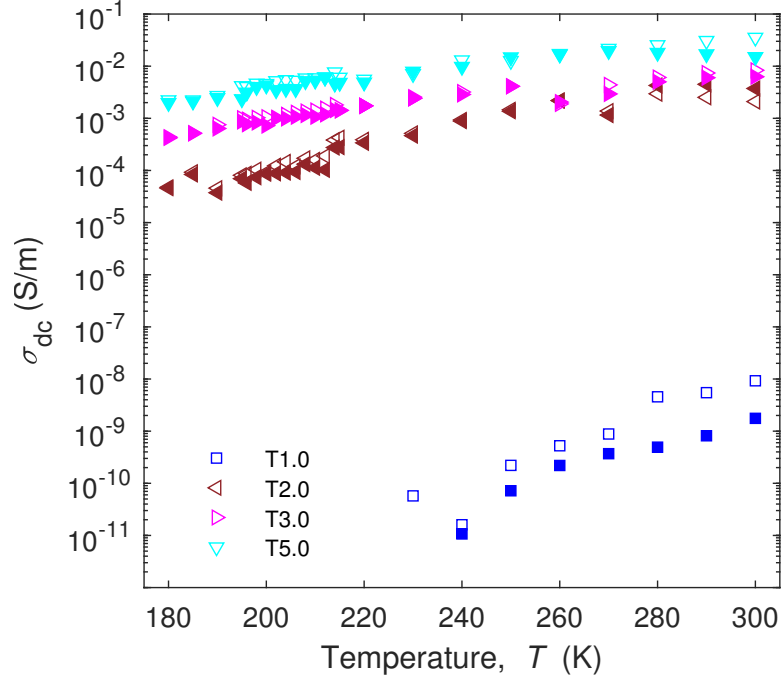
Figure A.3: DC conductivity obtained from fits to Eq. (3) (open symbols) and direct dc measurements (solid symbols) as a function of temperature for twin–screw extruded nanocomposites. Different symbols represent different MWCNT concentrations. The uncertainty in σ_{dc} is indicated by the scatter in the data.

Table A.1: Optimum fit parameters from fits of the HN model with two relaxation terms (Eq. (3)) to the ϵ'' data for sample M2.0. Parameters corresponding to the higher-frequency relaxation peak fit are not shown as that peak was outside of our experimental frequency range. Uncertainties in the parameters are given in parentheses.

T (K)	$\Delta\epsilon_1$	$\tau_1(10^{-5}\text{s})$	$\sigma_{dc}(10^{-7}\text{S/m})$
208	100 (4)	10 (1)	7.8 (0.1)
210	102 (10)	11 (5)	4.1 (0.2)
212	103 (8)	12 (3)	6.8 (0.2)
214	110 (6)	15 (3)	5.5 (0.1)
215	108 (4)	16 (2)	4.05 (0.07)
220	95 (3)	12 (1)	9.01 (0.08)
230	104 (4)	9 (1)	8.3 (0.2)
240	116 (3)	9.5 (0.9)	9.3 (0.1)
250	122 (9)	11 (3)	10.2 (0.3)
260	119 (10)	9 (2)	17.4 (0.5)
270	152 (3)	6.2 (0.5)	20.7 (0.2)
280	188 (3)	4.3 (0.4)	22.8 (0.2)
290	206 (5)	4.6 (0.4)	47.2 (0.3)
300	130 (20)	3 (1)	268 (3)

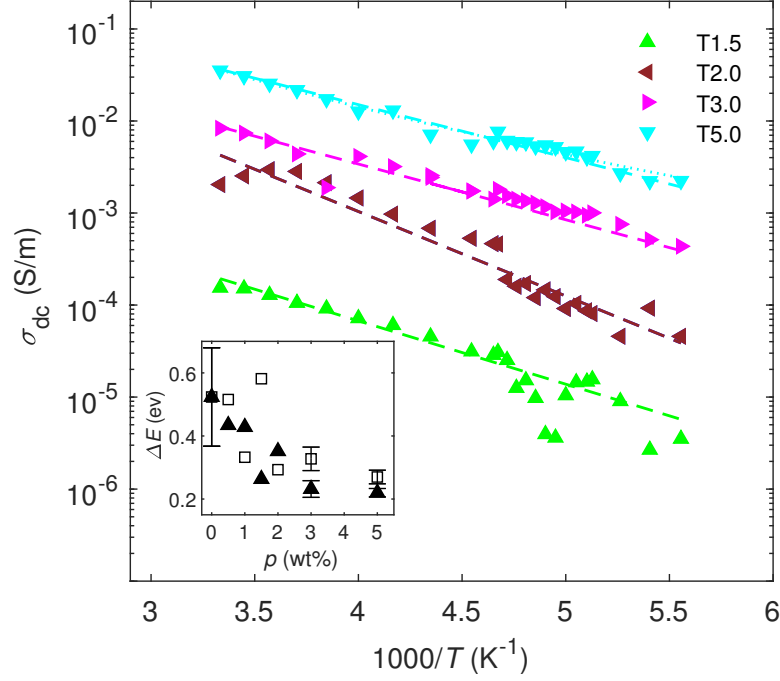Figure A.4: σ_{dc} plotted as a function of $1/T$ for different twin-screw extruded nanocomposites as indicated in the legend. The dashed lines are fits to Eq. (5) and the dotted line (shown only for T5.0) is a fit to Eq. (6). The uncertainty in σ_{dc} is indicated by the scatter in the data. The inset shows the activation energy ΔE determined from the fits to Eq. (5) for both M (open symbols) and T (solid symbols) nanocomposites as a function of MWCNT concentration p.

Table A.2: Optimum fit parameters from fits of the HN model with one relaxation terms (Eq. (3)) to the ϵ'' data for sample T2.0. Uncertainties in the parameters are given in parentheses.

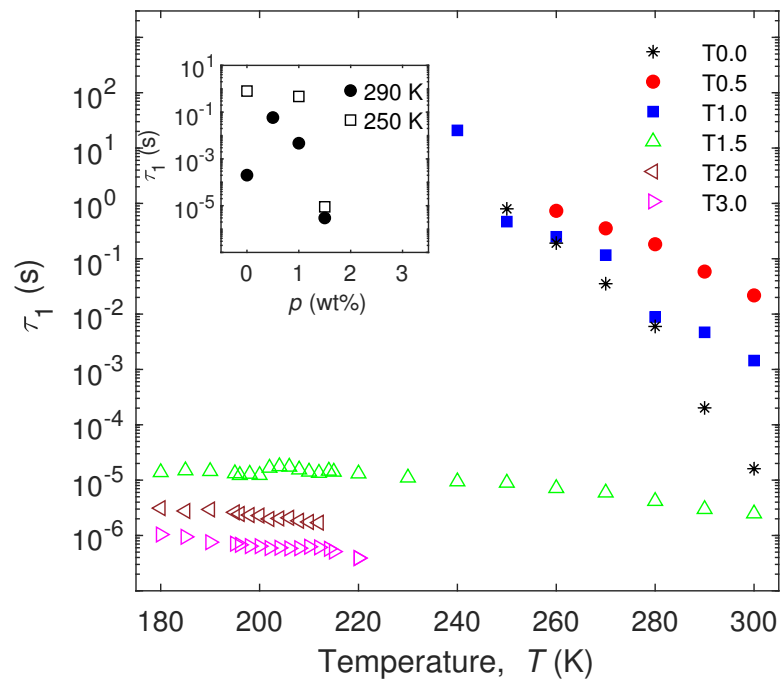| T (K)	$\Delta\epsilon_1$	$\tau_1(10^{-6}\text{s})$	$\sigma_{dc}(10^{-5}\text{S/m})$
180	244 (27)	3 (1)	4.6 (0.2)
185	225 (20)	2.8 (0.9)	9.2 (0.2)
190	269 (20)	3.0 (0.9)	4.6 (0.1)
195	245 (10)	2.6 (0.5)	8.1 (0.1)
196	237 (10)	2.4 (0.6)	8.7 (0.2)
198	240 (10)	2.3 (0.5)	10.4 (0.2)
200	227 (30)	2 (1)	9.2 (0.3)
202	207 (20)	2.0 (0.9)	12.4 (0.4)
204	204 (20)	2.0 (0.8)	14.6 (0.4)
206	228 (20)	2.1 (0.8)	12.0 (0.3)
208	203 (30)	1.8 (0.9)	17.1 (0.5)
210	199 (30)	2 (1)	16.0 (0.6)
212	194 (30)	2 (1)	19.0 (0.6)

Figure A.5: The dielectric relaxation time τ_1 of the twin-screw extruded nanocomposites plotted as a function of temperature. The different symbols represent different MWCNT concentrations, as indicated in the legend. The inset shows τ_1 at 290 and 250 K as a function of MWCNT concentration p.

Curriculum Vitae

Name: Nuwansiri Nirosh Getangama

Post-Secondary   University of Western Ontario
Education and   London, ON, Canada
Degrees: 2015 – to date Ph.D.

University of Western Ontario
London, ON
2013 – 2015 M.Sc.

University of Sri Jayewardenepura
Nugegoda, Sri Lanka
2006 – 2010 B.Sc.

Honours and   Robert and Ruth Lumsden Graduate Award, 2018-2019
Awards: Lillian Margaret & Walter David Jackson Scholarship in Physics, 2019

Related Work   Technical/Research Support 1
Experience: University of Western Ontario
2020 – to date

Teaching Assistant
University of Western Ontario
2013 – 2019

Teaching Assistant
Department of Physics
University of Sri Jayewardenepura
2010 – 2012

Conference Presentations : N. N. Getangama, J. R. de Bruyn and J. L. Hutter
Electrical and mechanical properties of polymer nanocomposites
CAMBR Distinguished Lecturer and Research Day
University of Western Ontario, London, ON, Canada, April 17, 2019

N. N. Getangama, J. R. de Bruyn and J. L. Hutter
Electrical and mechanical properties of polymer nanocomposites
The Society of Rheology 90th Annual Meeting
Houston, Texas, USA, October 14 – 18, 2018

N. N. Getangama, J. R. de Bruyn and J. L. Hutter
Electrical and mechanical properties of polymer nanocomposites
CAP Congress
Queen's University, Kingston, ON, Canada, May 29 - June 02, 2017

N. N. Getangama, J. R. de Bruyn and J. L. Hutter
Electrical and mechanical properties of polymer nanocomposites
Soft Matter Canada 2017
Queen's University, Kingston, ON, Canada, May 28, 2017

N. N. Getangama, J. R. de Bruyn and J. L. Hutter
Dielectric Spectroscopy of Polyvinyl Alcohol Hydrogels and Nanocomposites
CAP Congress
University of Alberta, Edmonton, AB, June 15 - June 19, 2015

N. N. Getangama, J. R. de Bruyn and J. L. Hutter
Dielectric Spectroscopy of Polyvinyl Alcohol Hydrogels and Nanocomposites
Fallona Family Interdisciplinary Showcase 2015
University of Western Ontario, London, ON, December 08, 2015

Publications:

1. N. N. Getangama, J. R. de Bruyn, J. L. Hutter, Dielectric Spectroscopy of Poly(ethylene oxide)-Carbon Nanotube Nanocomposites. Accepted for publication in *AIP Advances.*

2. M. Zheng, Q. Guo, X. Yin, N. N. Getangama, J. R. de Bruyn, J. Xiao, Y. Bai, M.Liu, J. Yang, Recyclable and In-situ Repairable 3D Printing via Direct Ink Writing of Photothermal Disulfide-based Polyurethane. *J. Mater. Chem. A:, 9:6981, 2021.*

3. N. N. Getangama, J. R. de Bruyn, J. L. Hutter, Electrical and Mechanical properties of PVA Cryogel prepared by freeze-thaw cycles, *J. Chem. Phys. 153:044901, 2020.*

4. M. Coady, N. N. Getangama, A. Khalili, M. Wood, K. Nielsen, J. de Bruyn, J. Hutter,

R. Klassen, A. Kietzig, P. Ragogna, Highly cross-linked UV-cured siloxane copolymer networks as icephobic coating, *J. Polym. Sci. 58:1022, 2020.*

5. J. A. Noel, N. N. Getangama, J. R. de Bruyn, M. A. White, Supercooling and Nucleation of Fatty Acids: Influence of Thermal History on the Behavior of the Liquid Phase, *J. Phys. Chem. B: 122:12386, 2018.*